Dissertation

Dispersion Control and Application of Cationic Polymer Particles by Surface Modification

（カチオン性ポリマー粒子表面の改質による分散性制御と応用）

Takashi Yamazaki

Contents

Chapter 1 General Introduction 6

1.1 Definition and Properties of Polymer Particles 6

1.2 Colloidal Stability 7

1.2.1 Dispersion Stability 7

1.2.2 Aggregation Kinetics of Colloidal Particles 7

1.2.3 Inter-Particle Interaction 8

1.3 Heterophase Polymerization Techniques 10

1.3.1 Emulsion Polymerization 10

1.3.2 Surfactant-Free Emulsion Polymerization 12

1.3.3 Miniemulsion Polymerization 13

1.3.4 Water-Soluble Azo Radical Initiators 15

1.3.5 Azo Radical Initiators with Quaternary Ammonium Structure 16

1.3.6 Polymeric Surfactants 17

1.4 Applications of Polymer Particles 17

1.4.1 Polystyrene Particles 17

1.4.2 Poly(methyl methacrylate) Particles 18

1.4.3 Particle-Stabilized Emulsions *via* Interfacial Assembly of Polymer Particles 18

1.5 Overview of the Dissertation 19

1.6 References 22

Chapter 2 Stability Control of Cationic PMMA Particles Using Cationic Azo Radical Initiators with Either Chloride or Triflate as Counter Anion 29

2.1 Introduction 29

2.2 Materials & Methods 29

2.2.1 Reagents 29
2.2.2 Particle Synthesis and Evaluation 30
2.2.3 Relationship between Diameter and Dispersion or Sedimentation 31
2.2.4 Aggregation of Cationic PMMA Latex Particles in the Presence of Electrolytes..... 32
2.2.5 Counterion Exchange of ADIP 32
Thermal decomposition and Arrhenius parameters 33
2.3 Results 34
2.3.1 Synthesis of PMMA Particles 34
2.3.2 Dispersion Stability of PMMA Latex Particles 36
2.3.3 Effect of Anion on the Aggregation of Cationic PMMA Latex Particles 39
2.3.4 Synthesis of ADIP-Cl 40
2.3.5 Synthesis of PMMA Latex Particles using ADIP-Cl..... 45
2.4 Discussion 46
2.4.1 Aggregation Mechanism in the Presence of Triflate 46
2.4.2 Synthesis of ADIP-Cl 46
2.5 Summary..... 46
2.6 References..... 47
Chapter 3 Dispersion Behavior of Cationic PMMA Particles in the Presence of Triflate Anion 48
3.1 Introduction..... 48
3.2 Materials & Methods..... 48
3.2.1 Reagents 48
3.2.2 Particle Synthesis and Evaluation 48
3.2.3 Surface Tension of Electrolytes 52
3.3 Results 53

3.3.1 Synthesis of PMMA Latex Particles 53
3.3.2 Zeta Potentials of PMMA Latex Particles Dispersed in Electrolyte Solutions 56
3.3.3 Time Courses of Dynamic Light Scattering 58
3.3.4 Stability Ratio of Cationic PMMA Latex Particles 68
3.3.5 Determination of CCC 70
3.3.6 Electrolyte Adsorption onto the Hydrophobic Interface 70
3.4 Discussion 72
3.5 Summary 72
3.6 References 73
Chapter 4 Functionalization of Cationic PMMA Particles 75
4.1 Introduction 75
4.2 Materials & Methods 75
4.2.1 Reagents 75
4.2.2 Particle Synthesis and Evaluation 76
4.2.3 Emulsion Preparation 77
4.2.4 Observation of Emulsions 78
4.2.5 Extraction of Insoluble Fraction 78
4.2.6 Fourier-Transform Infrared Spectroscopy 79
4.2.7 Gel Permeation Chromatography 79
4.2.8 Interfacial Tension 79
4.2.9 Simulation Methods 80
4.3 Results 84
4.3.1 Emulsion Observations 84
4.3.2 Evaluation of Synthetic Samples 89

4.4 Discussion 100
4.4.1 Characteristics of Pickering Emulsions Stabilized by PMMA-PVA 100
4.4.2 High Internal Oil Phase Pickering Emulsion 100
4.4.3 Properties of PMMA-PVA 101
4.4.4 Interfacial Adsorption Behavior of PMMA-PVA 102
4.5 Summary 103
4.6 References 104
Chapter 5 Encapsulation of Ultraviolet Absorber into Cationic Polystyrene Particles by Miniemulsion Polymerization using Poly(vinyl alcohol) 107
5.1 Introduction 107
5.2 Materials & Methods 109
5.2.1 Reagents 109
5.2.2 Emulsification 111
5.2.3 Synthesis of DHHB-Encapsulated Polystyrene Particles (PS-DHHB) 112
5.2.4 Characterization of PS-DHHB 113
5.2.5 Evaluation of DHHB Leaching from Particles into Aqueous Alcohol Solution 115
5.2.6 Evaluation of PS-DHHB Adsorption on Hair 116
5.2.7 Evaluation of Hair Protein Loss by UVA Irradiation 116
5.3 Results 118
5.3.1 Optimal Type of PVA for Miniemulsion Polymerization of Styrene 118
5.3.2 Polymerization Conditions for forming Stable and DHHB-rich PS-DHHB 121
5.3.3 UV Absorption of PS-DHHB 124
5.3.4 DHHB Leaching from PS-DHHB in Aqueous Alcohol 125
5.3.5 Hair Adsorption Properties of PS-DHHB 126
5.3.6 Inhibition of Protein Loss from Hair Due to UVA Irradiation 127

5.4 Discussion 128
5.4.1 Difference in Emulsification due to the Molecular Weight of PVA 128
5.4.2 Efficient Preparation of PS-DHHB *via* Miniemulsion Polymerization 128
5.4.3 UV Absorption and Hair Adsorption of PS-DHHB 129
5.4.4 Applications of PS-DHHB 130
5.5 Summary 131
5.6 References 132
Chapter 6 Conclusion 136
6.1 Summary 136
6.2 Future Prospects 137
6.3 References 138
List of Publications 139
Acknowledgments 140

Chapter 1 General Introduction

1.1 Definition and Properties of Polymer Particles

Polymer particles are spheres either made of natural polymers or produced by polymerization. They are characterized by size, size distribution, shape, as well as internal and external structures. For example, their optical properties depend on the particle size. Those larger than microns exhibit diffuse reflective properties and are used as a whitening agent. On the other hand, when the particles are uniform in size and in the range of visible light wavelength, they exhibit coloration due to light interference (structural color).

Polymer particles are often dispersed as a colloid in a continuous (*e.g.*, aqueous) phase and available commercially as ready-to-use products. Such dispersions, known as "latex", are used in the paper, paint, coating, additive, textile, and leather industries. In recent years, latex also found applications in medicine and biotechnology, such as *in vitro* diagnostics.

The nomenclature of polymer particles depends on their size. According to Japanese Industrial Standards (JIS) Z 8122:2000, those larger than 10 μm are called "coarse particles", those smaller than *ca*. 1 μm are "fine particles", and those between 0.1 and 1 μm are "submicron particles". Polymer particles used as aqueous dispersions are often smaller than 1 μm.

1.2 Colloidal Stability

1.2.1 Dispersion Stability

Fine or submicron particles cannot disperse in a liquid and will agglomerate unless there is sufficient inter-particle repulsive force. The reason is that as the particle size decreases, the ratio of the particle surface area to the total volume of particles increases, which raises the free energy of dispersion. Therefore, dispersions have a tendency for aggregation to reduce the surface area [1]. When this occurs for some reason, the resultant large coagulates easily settle out, and such sedimentation caused by aggregation causes reduced functionality of the final product [2]. Therefore, it is very important to control the dispersion/aggregation state of polymer particles by enhancing the repulsive inter-particle forces.

1.2.2 Aggregation Kinetics of Colloidal Particles

In 1917, Smoluchowski modeled the kinetics of irreversible aggregate formation due to collisions between colloidal particles [3]. However, there are known cases in which Smolukowski's model does not agree with the experimental results, and differences have also arisen between numerous experimental results and theoretical predictions [4]. To adequately describe the aggregation process, it is necessary to supplement Smolukowski's equation with equations corresponding to specific conditions.

Holthoff *et al*. suggested the kinetics of monodisperse colloids dispersed in water at the early stage of aggregation. The particle concentration of singlets and doublets as a function of time can be obtained by solving Eqs. (1.1) and (1.2), based on data measured using the light scattering method [5].

$$\frac{dn_1}{dt} = -k_{11}n_0^2 \tag{1.1}$$

$$\frac{dn_2}{dt} = \frac{1}{2}k_{11}n_0^2 \tag{1.2}$$

where n_0 is the initial particle concentration, and k_{11} is the coagulation rate constant for doublet formation in an initially monodisperse dispersion. The coagulation rate constant can then be expressed by an integral [6].

$$k_{11} = \left\{2a\int_0^\infty \frac{B(h)}{(2a+h)^2}\exp\left[\frac{V(h)}{k_BT}\right]dh\right\}^{-1}\frac{8k_BT}{3\mu} \tag{1.3}$$

where a is the particle radius, k_B is the Boltzmann constant, T is the temperature, μ is the viscosity of the fluid, $B(h)$ is a correcting factor for the diffusion coefficient, $V(h)$ is the attractive potential due to van der Waals (vdW) forces, and h is the inter-particle distance.

1.2.3 Inter-Particle Interaction

The colloidal particle surface is often charged due to protonation or deprotonation of ionizable groups. Counterions of opposite charge also collect around the particle, forming a diffused electric double layer. When two particles with the same type of charge approach each other and their diffused electric double layers overlap, the electrostatic repulsive force becomes dominant, and the particles repel each other. Meanwhile, the vdW force, which is universally generated between materials but depends on the distance, acts as an attractive force. These repulsive and attractive forces form the basis of the Derjaguin-Landau-Verwey-Overbeek (DLVO) theory [7]. Figure 1-1 depicts the free energy, which is the sum of the electrostatic repulsive force (V_{EDL}, Eq. 1.4) and vdW attractive force (V_{vdW}, Eq. 1.5), as a function of inter-particle distance according to the DLVO theory.

$$V_{EDL} = 2\pi a \Psi_0^2 \exp(-\kappa h) \tag{1.4}$$

$$V_{vdW} = -\frac{aA}{12h} \tag{1.5}$$

where Ψ_0 is the surface potential, κ is the Debye length, and A is the Hamaker constant. The Debye length at 25 ℃ is expressed by Eq. (1.6)

$$\kappa = 3.3 \times 10^9 z\sqrt{C} \tag{1.6}$$

where z is the electrolyte valance and C is the electrolyte concentration.

Colloidal particles aggregate when the attractive force is dominant and disperse when the repulsive force is dominant. The particles will aggregate easily if a large amount of electrolyte creates electrostatic shielding or if the particles carry a weak charge. Conversely, the particles tend to disperse under the opposite conditions. The DLVO theory states that the stability of latex is inversely proportional to the counterion valence raised to the 2nd–6th power. It is also in line with the experimental results of Schultze and Hardy [8]. However, even at the same counterion valance, the surface charge density of particles has been found to vary systematically with the type of counterions, just as expected for a hydrophobic surface within the Hofmeister series (Fig. 1-2) [9]. A hydrophobic ion tends to adsorb on the hydrophobic colloidal surface and drastically

decreases the surface charge density, resulting in aggregation at a lower electrolyte concentration. This situation can be categorized as a non-DLVO force [9-13].

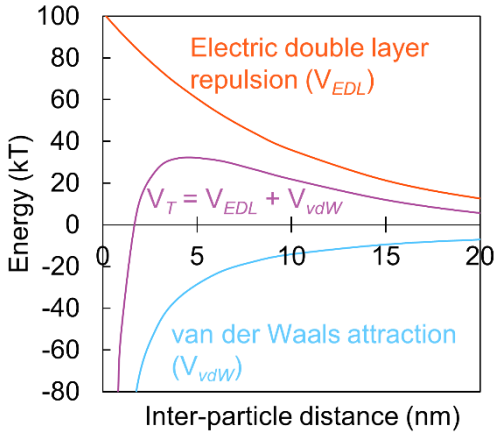

Fig. 1-1. Schematic diagram of the free energy as a function of inter-particle distance according to the DLVO theory. Electrolyte concentration: 10 mmol/L, electrolyte valance: 1, surface potential: +40 mV, particle radius: 100 nm, Hamaker constant: 3.9×10^{-20} J at 298 K.

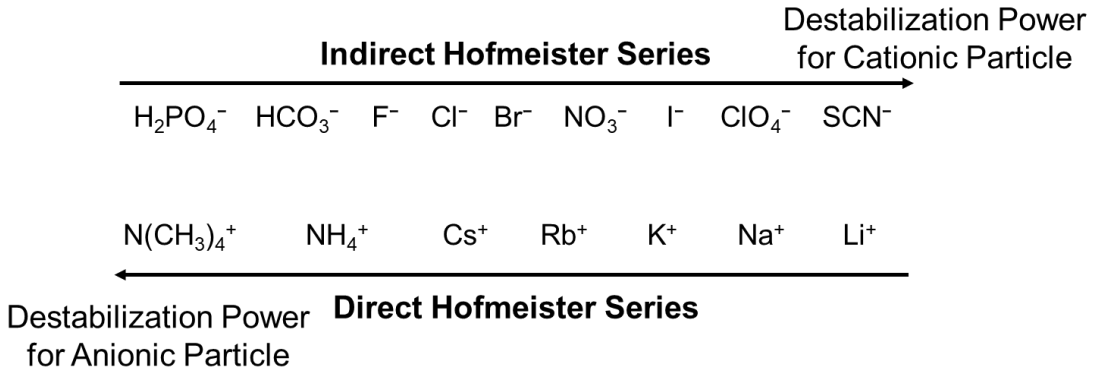

Fig. 1-2. Hofmeister series of monovalent anions and cations.

1.3 Heterophase Polymerization Techniques

1.3.1 Emulsion Polymerization

Polymer particles of spherical shape and uniform submicron size are synthesized under heterophase conditions. The reaction conditions should be chosen to avoid aggregation with consideration to the kinetics of polymerization and DLVO theory. If the polymer particle dispersion has poor stability, aggregation may occur during synthesis, resulting in undesired outcomes. Emulsion polymerization, one of the most popular heterophase polymerization techniques for preparing submicron particles, has its origin in the industrial production of synthetic rubber [14]. Harkins proposed a general mechanism of emulsion polymerization [15, 16], which assumes that particle formation occurs in swollen monomer micelles that are stabilized by surfactants. Based on his theory, Smith and Ewart developed a kinetic model of emulsion polymerization [17].

Emulsion polymerization requires a surfactant, a water-soluble radical initiator, and a vinyl monomer. The amount of surfactant should be at or above the critical micelle concentration to form micelles. Electrical charge of the surfactant will affect the electrostatic interactions and therefore the polymer particles' aggregation behavior. The vinyl monomer is dissolved inside the micelles, and the size of the swollen micelles is about 10 nm [18]. The vinyl monomer is slightly dissolved in the aqueous phase or dispersed as oil droplets.

Emulsion polymerization is initiated by free radicals generated when the water-soluble initiator decomposes under the action of heat or ultraviolet light. When the free radicals encounter slightly dissolved vinyl monomers in water, a chain propagation reaction proceeds to produce oligomeric radicals. When the oligomeric radicals reach a chain length that makes them insoluble in water, they are trapped in micelles swollen with the monomer, behaving like a surfactant. In the micelles, the oligomeric radicals repeatedly react with vinyl monomers to form a nucleus of fine particles. The nucleus is continuously supplied with vinyl monomer from the aqueous phase by diffusion, resulting in particle growth. When monomer in the micelles and monomer oil droplets are both depleted, polymerization is terminated, and polymer particles are obtained (Fig. 1-3).

The surface of particles synthesized by emulsion polymerization is covered with surfactant and molecular moieties of the initiator. These particles disperse well in aqueous medium because of the protonation or deprotonation of ionizable groups on their surface. However, repeated adsorption and desorption of surfactants from the particle surface have a negative impact for paint applications. Specifically, surfactant desorption lowers the homogeneity and functionality of painted surfaces. The toxicity of surfactants is also a concern for biological applications [19]. To

overcome these limitations, researchers have developed surfactants with the vinyl group (surfmer) [20]. These surfactants act as not only a surface-active material but also a monomer, and they are incorporated into the chain during polymerization to suppress desorption from the particle surface.

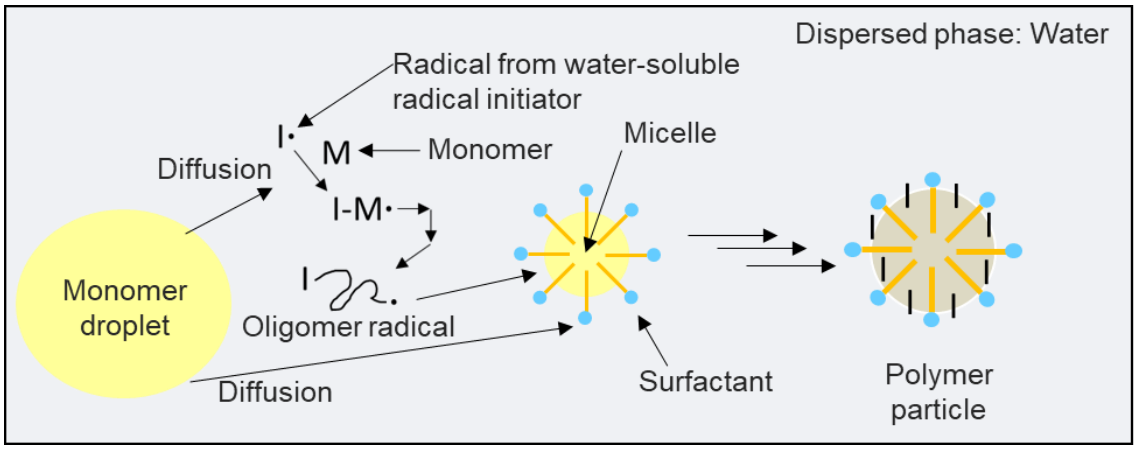

Fig. 1-3. Schematic diagram of the emulsion polymerization process. Objects here are not drawn to scale.

1.3.2 Surfactant-Free Emulsion Polymerization

The surfactant-free emulsion polymerization (SFEP) technique does not involve micelles created by surfactants. Rather, particle nucleation occurs at sites created by oligomeric radicals [19, 21, 22]. Latex synthesized by SFEP is stabilized either sterically or by electrostatic repulsive force from moieties of the radical initiator (Fig. 1-4).

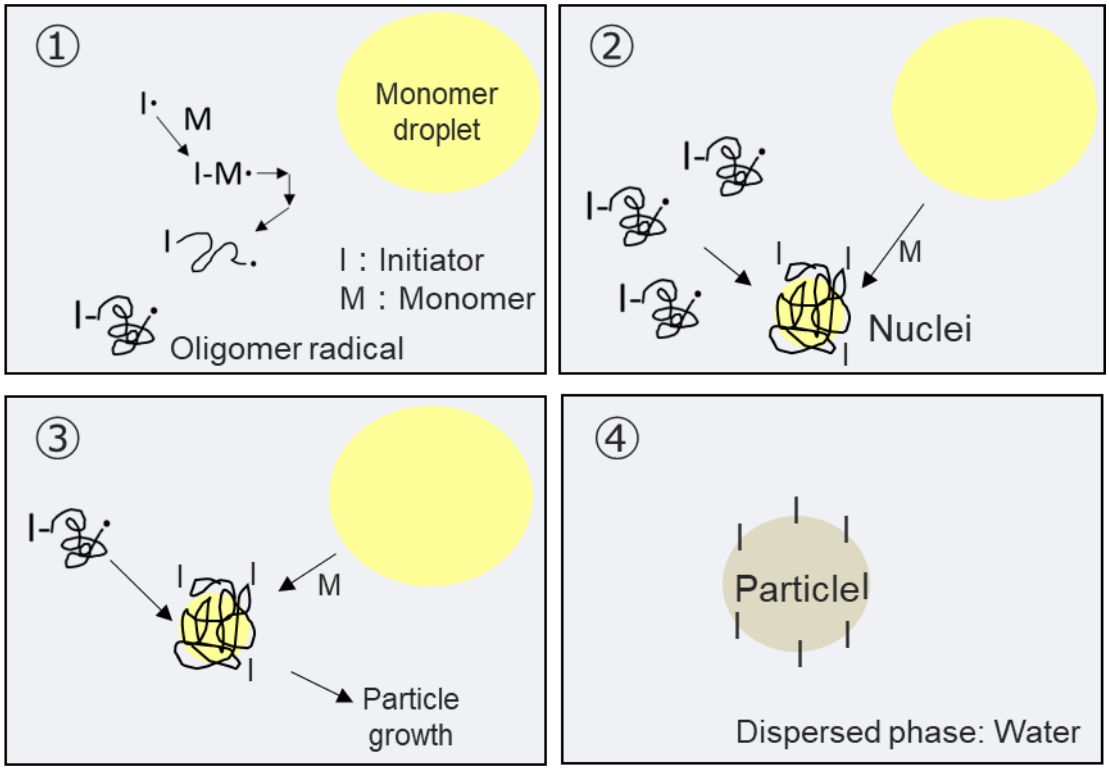

Fig. 1-4. Schematic diagram of particle growth steps in SFEP.

1.3.3 Miniemulsion Polymerization

Miniemulsion polymerization was developed by Ugelstad *et al.* in 1973 [23]. First, miniemulsion droplets (50–500 nm) are prepared in the presence of both a surfactant and a costabilizer by breaking an emulsion into submicron size using high-speed shearing, mechanical homogenization, or sonication. The prepared miniemulsion oil droplets have a much larger total surface area, with most of the surfactants adsorbed on the oil droplets and few micelles. Then, polymerization is initiated. Miniemulsion polymerization is very similar to emulsion polymerization in that it also uses water-soluble radical initiators [18]. Particle nucleation mainly occurs in the miniemulsion droplets after the entry of oligomeric radicals, which are generated *via* the chain propagation reaction. This is because micelles are rarely present in these systems, and also because there is insufficient free surfactant to stabilize any primary particles formed by homogeneous nucleation in the aqueous phase (Fig. 1-5). Ideally, all the miniemulsion droplets should be converted to particles by the oligomeric radicals.

The costabilizer (also called hydrophobe) is added to suppress the Ostwald ripening of miniemulsion droplets. The monomer should be soluble in the costabilizer but hardly soluble in the aqueous phase, so as to retard outward monomer diffusion into the aqueous phase from the miniemulsion droplets. For example, cetyl alcohol [24], hexadecane [24-27], and polystyrene (PS) [24] have been used as costabilizers. Miniemulsion polymerization has also been employed to encapsulate various organic (drugs [28], dyes [29], and scents [30]) or inorganic (pigments [24, 26], clays [31], and magnetite [32]) compounds that are difficult to dissolve or disperse in the aqueous phase.

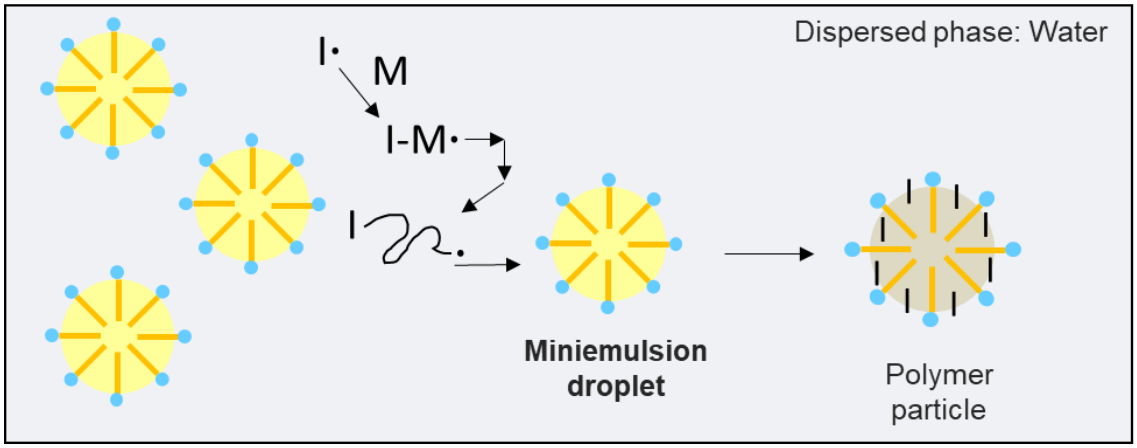

Fig. 1-5. Schematic diagram of nucleation mechanism in miniemulsion polymerization.

1.3.4 Water-Soluble Azo Radical Initiators

Several types of radical initiators have been developed [33]. The water-soluble ones consist of peroxides and azo compounds. An azo radical initiator generates nitrogen-containing free radicals during decomposition of the azo group (Fig. 1-6), and this system has some attractive features compared to peroxides. For instance, azo radical initiators suppress side reactions such as hydrogen atom abstraction, and functional groups are more easily introduced into azo radical initiators compared to peroxides. Focusing on ionic functionalized azo radical initiators, anionic, cationic, and zwitterionic structures have been developed. In 1979, Goodwin *et al*. prepared cationic PS latex particles using a cationic azo radical initiator [34]. This initiator was used with HCl, because its secondary or tertiary amine needs to be protonated by Brønsted-Lowry acids such as HCl.

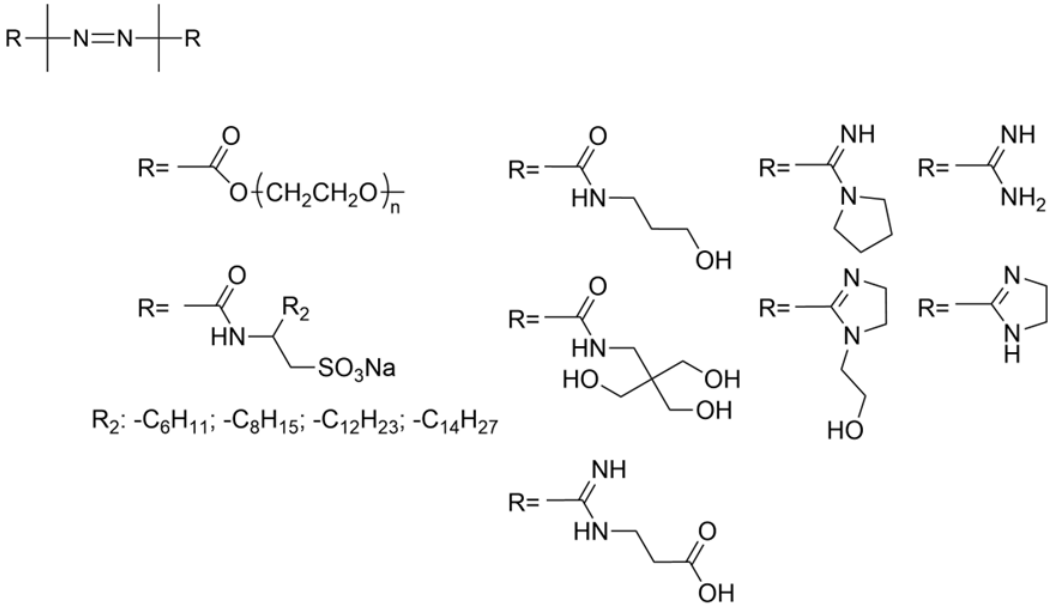

Fig. 1-6. Functional groups of various azo radical initiators.

1.3.5 Azo Radical Initiators with Quaternary Ammonium Structure

In 2018, Uchiyama *et al*. reported a new azo radical initiator with a quaternary ammonium structure {2,2′-azobis-[2-(1,3-dimethyl-4,5-dihydro-1*H*-imidazol-3-ium-2-yl)]propane triflate, ADIP, Fig. 1-7} [35]. The imidazolium structure, which is a quaternized moiety of ADIP, has attracted attention as a cationic group with high biological activity. In 2022, Suga *et al.* reported antimicrobial cationic PS particles prepared using ADIP [36]. The antimicrobial effect of these particles was predicted to be driven by membrane damage, through the so-called "contact-killing" mechanism. Specifically, membrane damage is induced by electrostatic interaction between the cationic particle surface and anionic bacterial membrane [37]. Moreover, those authors found that PS particles synthesized using ADIP had a stronger antimicrobial effect compared to those synthesized using other types of cationic azo radical initiators.

The trifluoromethanesulfonate anion (triflate, $CF_3SO_3^-$), which is the counterion of ADIP, is derived from methyl triflate that is used here for efficient methylation reaction (Fig. 1-7). Triflate has a unique surface activity. Lima *et al.* reported that the sodium triflate aqueous solution changes its surface tension drastically with the concentration. They predicted that the trifluoromethyl group may be dehydrated at the air-water interface, resulting in self-aggregated structures [38]. Despite such a unique characteristic, the influence of triflate toward colloidal interfacial activity (especially cationic polymeric particle dispersions) has not been reported yet. Moreover, it remains unclear how the counterion species of the cationic radical initiator impacts the polymer particle dispersion.

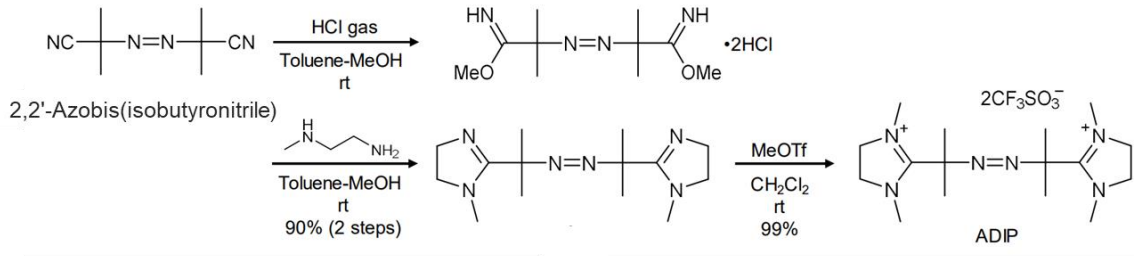

Fig. 1-7. Synthetic route of ADIP.

1.3.6 Polymeric Surfactants

Polymeric surfactants can be used to prevent coalescence and stabilize emulsion or miniemulsion droplets during polymerization, while avoiding the negative impact of surfactants described in Section 1.3.2. Polymers consisting of a PS block (3000 $g \cdot mol^{-1}$) and a poly(ethylene oxide) block (3000 $g \cdot mol^{-1}$) [39], poly(ethylene glycol) [39], poly(n-butyl methacrylate)-co-(tert-butyl methacrylate) prepared by reversible addition fragmentation chain are capable of transferring living free radical polymerization by γ-ray radiation [40]. Poly(dimethylamino)ethyl-methacrylate was also used for this purpose [41].

Poly(vinyl alcohol) (PVA) is a water-soluble polymer with excellent biocompatibility and chemical properties. It has been used in many industries, including as a polymeric surfactant in emulsion or miniemulsion polymerization. However, its utilization as a polymeric surfactant has been limited to vinyl acetate or vinyl chloride monomers, while it faces difficulties in the emulsion polymerization of conjugate monomers such as styrene and acrylic monomers due to the formation of coagulum [42]. This is because PVA molecules form a pseudo-micelle structure [43] rather than adsorbing onto the emulsion interface, resulting in destabilized monomer droplets and failure of polymerization. If the formation of pseudo-micelle structures can be suppressed, then PVA may be successfully applied to the polymerization of other monomer species.

1.4 Applications of Polymer Particles

1.4.1 Polystyrene Particles

PS particles are used for calibration and verification of instruments used for measuring the cleanliness and contamination control in semiconductors, pharmaceuticals, and drinking water [44]. Such PS particles are synthesized using potassium peroxide *via* emulsion polymerization or SFEP, and sulfonate groups are localized on the particle surface to yield a negative charge. To improve the dispersion stability in aqueous medium, carboxy group is introduced onto the particle surface by using carboxy acid vinyl monomer *via* copolymerization. Researchers have also encapsulated water-insoluble compound in PS particles *via* miniemulsion polymerization, as described in Section 1.3.3.

PS particles are also used in diagnostics. Fluorescent PS particles are prepared by either incorporating selected fluorophores into monodisperse particles using a swelling process or direct copolymerization of styrene with various organic fluorescent dyes. Several strategies have been developed to attach biological ligands to PS particles as a solid phase support in immunological tests and assays, such as adsorption to plain PS particles, covalent attachment to surface-functionalized particles, and attachment of the ligand of interest to particles that are pre-

coated with a binding protein [45]. Moreover, amino-functionalized cationic PS nanoparticles with positive charge have been utilized as markers for cells in research fields [46].

1.4.2 Poly(methyl methacrylate) Particles

Poly(methyl methacrylate) (PMMA) particles, which are prepared by polymerization of methyl methacrylate (MMA) monomer, have been widely used in paints and adhesives [47] and more recently in biological applications because of its biocompatibility. In cosmetics, PMMA particles can enhance the sensation of softness and hiding power of the product. In dentistry, they are used as a base resin for dentures [48]. Injectable PMMA particles are also developed as a soft filler for treating wrinkles and skin defects with long-lasting effects and high safety [49]. For example, ArteFill ™ consists of PMMA microspheres (20 vol%, 30–50 μm in diameter) suspended in 3.5% bovine collagen solution (80 vol%) for long-term wrinkle correction [49-51].

Submicron or nanosized PMMA particles have been used to manufacture pharmaceuticals with controlled-release characteristics. For instance, the coating reagent Kollicoat™ is composed of MMA and methacrylic acid vinyl ester with quaternary ammonium groups [52]. This latex dispersion contains a surfactant because it is prepared *via* emulsion polymerization. To achieve better biocompatibility, a coating reagent without surfactant was also developed, namely EUDRAGIT™ with non-spherical linear type of cationic PMMA. However, fabricating particulates composed of EUDRAGIT™ in aqueous medium is an additional process for drug pelletization [52]. In this context, the ability to prepare submicron cationic PMMA latex dispersion without surfactant *via* SFEP is crucial for optimizing the pharmaceutical manufacturing process.

1.4.3 Particle-Stabilized Emulsions *via* Interfacial Assembly of Polymer Particles

Emulsions stabilized by solid particles, also known as Pickering emulsions (PEs), were discovered by Ramsden [53] and Pickering [54]. PEs display particularly good stability (sometimes up to several years) thanks to their high resistance to coalescence [55]. Many types of mineral and organic particles have been used to prepare PEs. An important parameter controlling the interfacial desorption energy of these particles is their wettability, which can be estimated by measuring the three-phase contact angle of particles adsorbed at the oil-water interface according to the following equation Eq. (1.7).

$$\Delta E = \pi r^2 \gamma_{O/W} (1 - |\cos \theta_w|)^2 \quad (1.7)$$

where r is the radius of particles, $\gamma_{O/W}$ is the oil/water interfacial tension, and θ_w is the three-phase contact angle as reported by Binks [56].

The wettability of particles *via* surface modification for stabilizing PEs was discussed by Xiao *et al.* [57]. The stability of PEs can be improved by adsorbing small molecules on the particle surface, such as 8-hydroxyquinoline [58], fatty acids [59] or surfactants [60]. Compared to small molecules, particles that are anchored with polymers through chemical bonding or physical adsorption may create more stable PEs. For example, particles grafted with poly(2-(dimethylamino)ethyl methacrylate) [61] or poly(*N*-isopropylacrylamide) [62], as well as inorganic particles with physically adsorbed poly(ethylene imine) [63] or poly(ethylene glycol) [64], have been reported. The emulsification properties of these materials can change in response to stimuli such as heat and pH, depending on the characteristics of the polymers used for surface modification [57]. Several studies applied PVA as a surface modifier *via* physical adsorption [55, 65].

Synthetic polymeric particles offer certain advantages in their physical properties such as good size control, homogeneous size distribution, and variation in the modified surfaces. The amphiphilicity of particles determines the type of emulsion they form particles with hydrophilic and hydrophobic surfaces tend to form oil-in-water (O/W) and water-in-oil (W/O) emulsions, respectively.

1.5 Overview of the Dissertation

As mentioned above, introducing electric charge onto the surface of submicron polymer particles is a crucial technique for controlling the latex's dispersion/aggregation behavior and functionality. Positively charged particles are particularly attractive for biological applications.

In addition to inserting positive charges, composite particles with even better properties can be obtained *via* polymerization (*e.g.*, miniemulsion polymerization) or post-synthesis modification. In any case, it is important to select suitable materials to ensure particle dispersion without any aggregation. Some materials that could be useful for polymer particles have not been sufficiently investigated, while others already in use do not have their mechanisms clarified. For instance, the dispersion/aggregation effect of the counterion of cationic azo radical initiators has not been adequately discussed. Before the development of ADIP in 2018, using conventional cationic azo radical initiators was a useful technique to insert cationic moiety onto the particle surface. On the other hand, the prepared particles have to be protonated by hydrogen ion donors in aqueous condition. After the development of ADIP, the quaternary ammonium structure can be simply inserted onto the particle surface just by using the radical initiator. Nevertheless, the effect of the counterion of ADIP toward dispersion stability should be considered, whereas most conventional

cationic azo radical initiators have chloride as the counterion, which has a low aggregation effect based on the Hofmeister series. In particular, the influence of triflate (counterion of ADIP) on the colloidal interfacial activity of cationic polymeric particle dispersions has not been reported.

In the case of ADIP, only PS particles have been successfully prepared without any problem in dispersion stability. To expand the usage of ADIP in biological fields, I prepared PMMA particles using ADIP for the first time *via* SFEP. However, the stability of the resultant PMMA dispersion was quite low during storage. This phenomenon provides a motivation to investigate dispersion control of cationic polymer particles in the presence of the counterion of ADIP and functionalization of cationic polymer particles.

A second motivation of my research concerns PVA, whose utilization as a polymeric surfactant is still limited, as mentioned in Section 1.3.4. In fact, PVA comes in many types depending on the degrees of polymerization and saponification, but only a few types have been considered as polymeric surfactants. Moreover, there is little discussion on using PVA as a surface modifier to create particle stabilizers for PEs, *i.e.*, which types of PVA are suitable for preparing PEs with good stability.

The rest of the Dissertation consists of four Chapters. Chapter 2 describes the synthesis of PMMA particles *via* SFEP, using MMA monomer and ADIP as a radical initiator. The dispersion stability of synthesized cationic PMMA particles was evaluated. Fast sedimentation of dispersion during storage was only observed when ADIP was used in particle synthesis. Further investigation revealed that cationic PMMA particles aggregate significantly in the presence of triflate anion compared to halides or polyatomic anions. To overcome this problem, I developed ADIP-Cl, an ADIP derivative with the triflate counter anion replaced with chloride. When using ADIP-Cl, cationic PMMA particles were successfully prepared without any sedimentation.

Chapter 3 discusses the reason why triflate causes the aggregation of cationic PMMA latex particles. The surface charge of these particles was significantly reduced in the presence of triflate at a lower concentration compared to the other anions. This is because triflate more strongly absorbs onto the hydrophobic surface. The mechanism of aggregation induced by triflate would mainly be the vdW force between particles because the cationic surface is neutralized by adsorbed triflate anions, resulting in a weaker electrostatic repulsive force. Accordingly, the transition between dispersion and aggregation in the presence of electrolyte was kinetically evaluated.

Chapter 4 describes the functionalization of cationic PMMA particles prepared using ADIP-Cl, in order to create PEs with possible industrial applications. Cationic particles are expected to be more suitable for PEs, because the oil-water interface carries negative charge [66] and therefore

cationic particles are more prone to adsorb there through electrostatic interactions. Experimentally, however, phase separation occurred soon after agitating a system of oil, water, and the cationic PMMA particles. To suppress emulsion collapse, the particle surface could be modified to enhance their adsorption onto the interface [31]. PVA was previously used to modify particles for forming PEs [55, 65]. PVA, a water-soluble polymer synthesized through hydrolysis of poly(vinyl acetate), contains hydroxy and acetate groups along the chain. Yet, there has been no report on the optimal ratio between these two groups for forming PEs. Thus, I evaluated the hydrolysis level of PVA in order to modify the cationic PMMA particle surface with PVA for successful emulsion preparation.

In Chapter 5, an ultraviolet (UV) absorber was encapsulated in cationic PS particles and dispersed in water using miniemulsion polymerization. To stabilize the miniemulsion droplets composed of styrene monomer and the UV absorber, I investigated which type of PVA is suitable as a polymeric surfactant. For the first time, low-molecular-weight PVA was shown to works as an emulsifier to facilitate both the formation of miniemulsion droplets and the subsequent polymerization process. Importantly, the inclusion of PS in the monomer droplet increased the solid content and functioned as a costabilizer, thereby enhancing the encapsulation efficiency of the UV absorber. Additionally, adding aqueous alcohol as an antibacterial agent did not cause the UV absorber to leach from the capsule particles. Test results further revealed that compared to the anionic PS capsule particles, the cationic ones adhered more effectively to human hair. The cationic PS particles with the UV absorber also had superior performance in mitigating UV-induced hair protein loss in the 320–400 nm range, compared to particles without the UV absorber. In summary, the research described in Chapter 5 facilitates the development of water-dispersible cationic PS particles with significant applications in polymer science and cosmetics, owing to their efficient UV absorption and effective hair adhesion capabilities.

1.6 References

[1]. Kitahara, A. (1970). A few basic knowledges on solid-liquid interface. *J. Jpn. Soc. Colour Mater.*, 43(12), 622-628 in Japanese.

[2]. Kamiya, H. (2016). Aggregation and dispersion behavior control of nanoparticles by surface structure design. *Oleoscience*, 16(2), 57-63 in Japanese.

[3]. Hidalgo-Alvarez, R., Martin, A., Fernandez, A., Bastos, D., Martinez, F., & De Las Nieves, F. J. (1996). Electrokinetic properties, colloidal stability and aggregation kinetics of polymer colloids. *Adv. Colloid Interface Sci*., 67, 1-118.

[4]. Wilemski, G. (1976). On the derivation of Smoluchowski equations with corrections in the classical theory of Brownian motion. *J. Stat. Phys.*, 14, 153-169.

[5]. Helmut, H., Egelhaaf, S. U., Borkovec, M., Schurtenberger, P., & Sticher, H. (1996). Coagulation rate measurements of colloidal particles by simultaneous static and dynamic light scattering. *Langmuir*, 12(23), 5541-5549.

[6]. Kobayashi, M. (2012). Aggregation kinetics of colloidal particles. In: Electrical Phenomena at Interfaces and Biointerfaces: Fundamentals and Applications in Nano-, Bio-, and Environmental Sciences, John Wiley & Sons, 173-191.

[7]. Ninham, B. W. (1999). On progress in forces since the DLVO theory. *Adv. Colloid Interface Sci.*, 83(1-3), 1-17.

[8]. Hall, S. B., Duffield, J. R., & Williams, D. R. (1991). A reassessment of the applicability of the DLVO theory as an explanation for the Schulze-Hardy rule for colloid aggregation. *J. Colloid Interface Sci.*, 143(2), 411-415.

[9]. Oncsik, T., Trefalt, G., Borkovec, M., & Szilagyi, I. (2015). Specific ion effects on particle aggregation induced by monovalent salts within the Hofmeister series. *Langmuir*, 31(13), 3799-3807.

[10]. Eom, N., Parsons, D. F., & Craig, V. S. (2017). Roughness in surface force measurements: Extension of DLVO theory to describe the forces between hafnia surfaces. *J. Phys. Chem. B*, 121(26), 6442-6453.

[11]. Calero, C., Faraudo, J., & Bastos-Gonzalez, D. (2011). Interaction of monovalent ions with hydrophobic and hydrophilic colloids: Charge inversion and ionic specificity. *J. Am. Chem. Soc*., 133(38), 15025-15035.

[12]. Cao, T., Trefalt, G., & Borkovec, M. (2018). Aggregation of colloidal particles in the presence of hydrophobic anions: Importance of attractive non-DLVO forces. *Langmuir*, 34(47), 14368-14377.

[13]. Sugimoto, T., Cao, T., Szilagyi, I., Borkovec, M., & Trefalt, G. (2018). Aggregation and charging of sulfate and amidine latex particles in the presence of oxyanions. *J. Colloid Interface Sci.*, 524, 456-464.

[14]. Antonietti, M., & Tauer, K. (2003). 90 years of polymer latexes and heterophase polymerization: more vital than ever. *Macromol. Chem. Phys.*, 204(2), 207-219.

[15]. Harkins, W. D. (1947). A general theory of the mechanism of emulsion polymerization[1]. *J. Am. Chem. Soc*., 69(6), 1428-1444.

[16]. Harkins, W. D. (1950). General theory of mechanism of emulsion polymerization. II. *J. Polym. Sci*., 5(2), 217-251.

[17]. Smith, W. V., & Ewart, R. H. (1948). Kinetics of emulsion polymerization. *J. Chem. Phys.*, 16(6), 592-599.

[18]. Lovell, P. A., & Schork, F. J. (2020). Fundamentals of emulsion polymerization. *Biomacromolecules*, 21(11), 4396-4441.

[19]. Kawaguchi, H. (2005). Emulsion polymerization. *NIHON GAZO GAKKAISHI: Journal of the Imaging Society of Japan*, 44(5), 369-374 in Japanese.

[20]. Schoonbrood, H. A., & Asua, J. M. (1997). Reactive surfactants in heterophase polymerization. 9. Optimum surfmer behavior in emulsion polymerization. *Macromolecules*, 30(20), 6034-6041.

[21]. Goodall, A. R., Wilkinson, M. C., & Hearn, J. (1977). Mechanism of emulsion polymerization of styrene in soap-free systems. *J. Polym. Sci.*: *Polymer Chemistry Edition*, 15(9), 2193-2218.

[22]. Shibuya, K., Nagao, D., Ishii, H., & Konno, M. (2014). Advanced soap-free emulsion polymerization for highly pure, micron-sized, monodisperse polymer particles. *Polymer*, 55(2), 535-539.

[23]. Ugelstad, J., El-Aasser, M. S., & Vanderhoff, J. W. (1973). Emulsion polymerization: Initiation of polymerization in monomer droplets. *J. Polym. Sci., Polymer Letters Edition*, 11(8), 503-513.

[24]. Lelu, S., Novat, C., Graillat, C., Guyot, A., & Bourgeat-Lami, E. (2003). Encapsulation of an organic phthalocyanine blue pigment into polystyrene latex particles using a miniemulsion polymerization process. *Polym. Int*., 52(4), 542-547.

[25]. Tiarks, F., Landfester, K., & Antonietti, M. (2001). Preparation of polymeric nanocapsules by miniemulsion polymerization. *Langmuir*, 17(3), 908-918.

[26]. Steiert, N., & Landfester, K. (2007). Encapsulation of organic pigment particles via miniemulsion polymerization. *Macromol. Mater. Eng.*, 292(10-11), 1111-1125.

[27]. Cao, Z. H., Shan, G. R., Sheibat-Othman, N., Putaux, J. L., & Bourgeat-Lami, E. (2010). Synthesis of oily core-hybrid shell nanocapsules through interfacial free radical copolymerization in miniemulsion: Droplet formation and nucleation. *J. Polym. Sci. Part A: Polym. Chem.*, 48(3), 593-603.

[28]. Landfester, K., & Mailänder, V. (2013). Nanocapsules with specific targeting and release properties using miniemulsion polymerization. *Expert Opin. Drug Delivery*, 10(5), 593-609.

[29]. Li, J., Fan, J., Cao, R., Zhang, Z., Du, J., & Peng, X. (2018). Encapsulated dye/polymer nanoparticles prepared via miniemulsion polymerization for inkjet printing. *ACS Omega*, 3(7), 7380-7387.

[30]. Kaur, R., Kukkar, D., Bhardwaj, S. K., Kim, K. H., & Deep, A. (2018). Potential use of polymers and their complexes as media for storage and delivery of fragrances. *J. Controlled Release*, 285, 81-95.

[31]. Hu, J., Chen, M., & Wu, L. (2011). Organic-inorganic nanocomposites synthesized via miniemulsion polymerization. *Polym. Chem*., 2(4), 760-772.

[32]. Hoffmann, D., Landfester, K., & Antonietti, M. (2001). Encapsulation of magnetite in polymer particles via the miniemulsion polymerization process. *Magnetohydrodynamics*, 37(3), 217-221.

[33]. Androvič, L., Bartáček, J., & Sedlák, M. (2016). Recent advances in the synthesis and applications of azo initiators. *Res. Chem. Intermed.*, 42, 5133-5145.

[34]. Goodwin, J. W., Ottewill, R. H., & Pelton, R. (1979). Studies on the preparation and characterization of monodisperse polystyrene latices V.: The preparation of cationic latices. *Colloid. Polym. Sci.*, 257, 61-69.

[35]. Uchiyama, S., Tsuji, T., Kawamoto, K., Okano, K., Fukatsu, E., Noro, T., Ikado, K., Yamada, S., Shibata, Y., Hayashi, T., Inada, N., Kato, M., Koizumi, H., & Tokuyama, H. (2018). A cell-targeted non-cytotoxic fluorescent nanogel thermometer created with an imidazolium-containing cationic radical initiator. *Angew. Chem. Int. Ed*., 57(19), 5413-5417.

[36]. Suga, K., Murakami, M., Nakayama, S., Watanabe, K., Yamada, S., Tsuji, T., & Nagao, D. (2022). Surface characteristics of antibacterial polystyrene nanoparticles synthesized using cationic initiator and comonomers. *ACS Appl. Bio. Mater*., 5(5), 2202-2211.

[37]. Kaur, R., & Liu, S. (2016). Antibacterial surface design–Contact kill. *Prog. Surf. Sci.*, 91(3), 136-153.

[38]. Lima, F. S., Maximiano, F. A., Cuccovia, I. M., & Chaimovich, H. (2011). Surface activity of the triflate ion at the air/water interface and properties of *N*,*N*,*N*-trimethyl-*N*-dodecylammonium triflate aqueous solutions. *Langmuir*, 27(8), 4319-4323.

[39]. Tiarks, F., Landfester, K., & Antonietti, M. (2001). Preparation of polymeric nanocapsules by miniemulsion polymerization. *Langmuir*, 17, 908-918.

[40]. Wang, S., Qiang, Y., Zhang, Z., & Wang, X. (2006). Emulsion polymerization stabilized by polymeric surfactant prepared by γ-ray radiation. *Colloids Surf. A*, 281(1-3), 156-162.

[41]. Ni, P., Zhang, M., Ma, L., & Fu, S. (2006). Poly (dimethylamino) ethyl methacrylate for use as a surfactant in the miniemulsion polymerization of styrene. *Langmuir*, 22(14), 6016-6023.

[42]. Lu, Y., Liu, X., & Luo, G. (2017). Synthesis of polystyrene latex via emulsion polymerization with poly(vinyl alcohol) as sole stabilizer. *J. Appl. Polym. Sci.*, 134(32), 45111.

[43]. Budhlall, B. M., Landfester, K., Sudol, E. D., Dimonie, V. L., Klein, A., & El-Aasser, M. S. (2003). Characterization of partially hydrolyzed poly(vinyl alcohol). Effect of poly(vinyl alcohol) molecular architecture on aqueous phase conformation. *Macromolecules*, 36, 9477-9484.

[44]. Hikata, M., Sakuma, M., & Fukai, Y. (2007). Manufacture of polystyrene standard particles and their applications. *Earozoru Kenkyu*, 22(4), 282-288 in Japanese.

[45]. Cantarero, L. A., Butler, J. E., & Osborne, J. W. (1980). The adsorptive characteristics of proteins for polystyrene and their significance in solid-phase immunoassays. *Anal. Biochem.*, 105(1), 375-382.

[46]. Holzapfel, V., Musyanovych, A., Landfester, K., Lorenz, M. R., & Mailänder, V. (2005). Preparation of fluorescent carboxyl and amino functionalized polystyrene particles by miniemulsion polymerization as markers for cells. *Macromol. Chem. Phys.*, 206(24), 2440-2449.

[47]. Croll, S. G. (1983). Adhesion and internal strain in polymeric coatings. In: Adhesion Aspects of Polymeric Coatings (pp. 107-129). Boston, MA: Springer US.

[48]. Kaur, H., & Thakur, A. (2022). Applications of poly(methyl methacrylate) polymer in dentistry: A review. *Mater. Today Proc.*, 50, 1619-1625.

[49]. Lemperle, G. (2018). Biocompatibility of injectable microspheres. *Biomed. J. Sci. & Tech. Res.*, 2(1), 11.

[50]. Lemperle, G., Knapp, T. R., Sadick, N. S., & Lemperle, S. M. (2010). ArteFill® permanent injectable for soft tissue augmentation: I. Mechanism of action and injection techniques. *Aesthetic Plast. Surg.*, 34, 264-272.

[51]. Lemperle, G., Neugebauer, P., Kernke, R., Lerche, K. H., & Lemperle, S. M. (2017). Microspheres for cosmetic and medical injections must be free of phagocytosable microparticles under 20 microns. *Biomed. J. Sci. & Tech. Res.*, 1(6), 1982-1686.

[52]. Kondo, K. (2024). Development of solventless pharmaceutical technique for manufacture of pharmaceuticals. *YAKUGAKU ZASSHI: Journal of the Pharmaceutical Society of Japan*, 144(10), 919-930 in Japanese.

[53]. Ramsden, W. (1904). Separation of solids in the surface-layers of solutions and ‘suspensions’(observations on surface-membranes, bubbles, emulsions, and mechanical coagulation).—Preliminary account. *Proc. R. Soc. London*, 72(477-486), 156-164.

[54]. Pickering, S. U. (1907). CXCVI.—Emulsions, *J. Chem. Soc., Trans.*, 91, 2001-2021.

[55]. Albert, C., Huang, N., Tsapis, N., Geiger, S., Rosilio, V., Mekhloufi, G., Chapron, D., Robin, B., Beladjine, M., Nicolas, V., Fattal, E., & Agnely, F. (2018). Bare and sterically stabilized PLGA nanoparticles for the stabilization of Pickering emulsions. *Langmuir*, 34(46), 13935-13945.

[56]. Binks, B. P. (2002). Particles as surfactants—similarities and differences. *Curr. Opin. Colloid Interface Sci.*, 7(1-2), 21-41.

[57]. Xiao, M., Xu, A., Zhang, T., & Hong, L. (2018). Tailoring the wettability of colloidal particles for Pickering emulsions via surface modification and roughness. *Front. Chem*., 6, 225.

[58]. Haase, M. F., Grigoriev, D., Moehwald, H., Tiersch, B., & Shchukin, D. G. (2010). Encapsulation of amphoteric substances in a pH-sensitive Pickering emulsion. *J. Phys. Chem. C*, 114(41), 17304-17310.

[59]. Tabatabaei, M., Rajaei, A., Hosseini, E., Aghbashlo, M., Gupta, V. K., & Lam, S. S. (2022). Effect of type of fatty acid attached to chitosan on walnut oil-in-water Pickering emulsion properties. *Carbohydr. Polym.*, 291, 119566.

[60]. Wang, S., Shen, Y., Chen, X., Dong, L., Yu, H., Bao, M., & Li, Y. (2022). Cationic surfactant-modified palygorskite particles as effective stabilizer for Pickering emulsion gel formation. *Appl. Clay Sci*., 219, 106439.

[61]. Saigal, T., Dong, H., Matyjaszewski, K., & Tilton, R. D. (2010). Pickering emulsions stabilized by nanoparticles with thermally responsive grafted polymer brushes. *Langmuir*, 26(19), 15200-15209.

[62]. Pei, X., Zhai, K., Wang, C., Deng, Y., Tan, Y., Zhang, B., ... & Wang, P. (2019). Polymer brush graft-modified starch-based nanoparticles as Pickering emulsifiers. *Langmuir*, 35(22), 7222-7230.

[63]. Williams, M., Armes, S. P., Verstraete, P., & Smets, J. (2014). Double emulsions and colloidosomes-in-colloidosomes using silica-based Pickering emulsifiers. *Langmuir*, 30(10), 2703-2711.

[64]. Isa, L., Amstad, E., Schwenke, K., Del Gado, E., Ilg, P., Kröger, M., & Reimhult, E. (2011). Adsorption of core-shell nanoparticles at liquid–liquid interfaces. *Soft Matter*, 7(17), 7663-7675.

[65]. Robin, B., Albert, C., Beladjine, M., Legrand, F. X., Geiger, S., Moine, L., Nicolas, V., Canette, A., Trichet, M., Tsapis, N., Agnely, F., & Huang, N. (2021). Tuning morphology of Pickering emulsions stabilised by biodegradable PLGA nanoparticles: How PLGA characteristics influence emulsion properties. *J. Colloid Interface Sci*., 595, 202-211.

[66]. Marinova, K. G., Alargova, R. G., Denkov, N. D., Velev, O. D., Petsev, D. N., Ivanov, I. B., & Borwankar, R. P. (1996). Charging of oil− water interfaces due to spontaneous adsorption of hydroxyl ions. *Langmuir*, 12(8), 2045-2051.

Chapter 2 Stability Control of Cationic PMMA Particles Using Cationic Azo Radical Initiators with Either Chloride or Triflate as Counter Anion

2.1 Introduction

This chapter describes how the counterion of cationic azo radical initiators affects the dispersion of the resultant polymer particles. As mentioned in Section 1.5, few studies have examined the dispersion/aggregation effect of counterion of these initiators toward polymer particle dispersion. Originally, I synthesized PMMA latex particles *via* SFEP using ADIP, but their dispersion was far less stable than those prepared using another cationic azo radical initiator. Cationic colloidal dispersions in the presence of triflate (the counterion of ADIP), have also not been reported to date. Even when using ions of the same valance, the surface charge density of particles varies systematically with the ion type, as can be expected for a hydrophobic surface within the Hofmeister series as mentioned in Section 1.2.3. Accordingly, research described in this chapter aims to identify the reason for the sedimentation of those cationic PMMA particles and modify ADIP to improve the dispersion stability.

2.2 Materials & Methods

2.2.1 Reagents

Water treated by reverse osmosis and electrodeionization was used in all the experiments. Acetone, methanol, ethanol, hydrochloric acid, methyl methacrylate (MMA, purity ≥ 98.0%), 2,2'-azobis(2-methylpropionamidine) dihydrochloride (V-50), 2,2'-azobis[2-(2-imidazolin-2-yl)propane]dihydrochloride (VA-044), potassium chloride (KCl, purity ≥ 99.5%), potassium bromide (KBr, purity ≥ 99.0%), potassium iodide (KI, purity ≥ 99.5%), potassium nitrate (KNO_3, purity ≥ 99.0%), potassium sulfate (K_2SO_4, purity ≥ 99.0%), and potassium triflate (KCF_3SO_3, purity > 98.0%) were purchased from Fujifilm Wako Pure Chemical Corporation, Japan. Styrene and potassium methanesulfonate (KCH_3SO_3, purity > 98.0%) were purchased from Tokyo Chemical Industry Corporation, Japan. ADIP was synthesized following the literature procedure [1]. Insert Sep® SAX-2 (catalog number: 5010-61707) was purchased from GL Sciences, Japan, and it consists of silica gels modified with trimethylaminopropyl group.

2.2.2 Particle Synthesis and Evaluation

Synthesis

All solvents were deoxygenated by bubbling with dry nitrogen gas. Prior to use, MMA was processed with an inhibitor remover (catalog number: 311332, Sigma-Aldrich Corporation, USA) to eliminate hydroquinone as a polymerization inhibitor. All polymerization reactions were conducted under magnetic stirring in sealed 30-mL glass vials (height: 65 mm, ϕ30 mm) in a temperature-controlled water bath. The length and ϕ of the stirrer were 12 mm and 4.5 mm, respectively. To prepare PMMA particles in aqueous media, MMA and an initiator were added to water, and polymerization was conducted for 16 h at 60 °C. Afterwards, all emulsions were cooled to room temperature and then characterized.

Conversion

The amount of PMMA particles in the polymer dispersion was calculated based on the weight after drying in an oven at 100 ℃ for 1 h.

Dynamic light scattering

The average hydrodynamic diameter {$D(H)$, Eq. (2.1)} and polydispersity index {PDI, Eq. (2.2)} of PMMA particles were determined using a dynamic light scattering (DLS) instrument (Zetasizer Nano ZSP, Malvern Instruments Limited, UK) equipped with a 10 mW He-Ne laser with a wavelength of 633 nm. Data were collected and analyzed using Dispersion Technology software (version 7.13; Malvern Instruments Limited). The measurements were initiated after a delay of 30 s to allow the sample to equilibrate. The instrument was operated in the backscatter mode at an angle of 173° (noninvasive backscatter, NIBS®), and 11 runs (10 s per run) were performed on each sample in cuvettes (DTS1070, Malvern).

$$D(H) = \frac{k_B T}{3\pi\eta D} \tag{2.1}$$

where z is the diffusion coefficient, k_B is Boltzmann constant, T is the temperature, and η is the viscosity of the medium.

$$\text{PDI} = \frac{\mu_2}{\bar{\Gamma}^2} \tag{2.2}$$

where μ_2 is the second moment and Γ is the average decay rate.

Scanning electron microscopy

Scanning electron microscopy (SEM, Nova NanoSEM 450, FEI Co., USA) analysis was conducted at an accelerating voltage of 700 V and a magnification of 20,000×. Each PMMA

emulsion (1 μL) was dropped onto a cleaned aluminum foil, dried well, and observed directly under SEM. The obtained images were analyzed by the NaviCam software (Sony Computer Science Laboratories, Inc., Japan). The average diameter (d_{SEM}) of the synthesized polymer particles was calculated based on 10 particles in the images.

Macroscopic observation

The PMMA particle dispersion was placed in a 10-mL vial at 25 ℃, and its appearance was monitored to evaluate the stability. After three months, the vial was turned upside down to check for sedimentation at the bottom.

2.2.3 Relationship between Diameter and Dispersion or Sedimentation

This relationship was derived based on Stokes' law (Eq. 2.3) and Brownian motion (Eq. 2.4) [2]:

$$u = \frac{D_p(\rho - \rho_0)g}{18\eta} \tag{2.3}$$

where D_p is the polymer particle diameter, ρ is the particle density, ρ_0 is the density of the medium, and g is the gravitational constant.

$$\langle x \rangle = \left(\frac{k_B T}{6\pi\eta D_p} \right)^{0.5} \tag{2.4}$$

Figure 2-1 shows the relationship between dispersion and sedimentation of PMMA particles. The threshold of dispersion stability corresponds to the intersection of the lines for Eqs. (2.3) and (2.4). Particles with a diameter less than ~2 μm are dominated by dispersion, whereas larger particles are dominated by sedimentation.

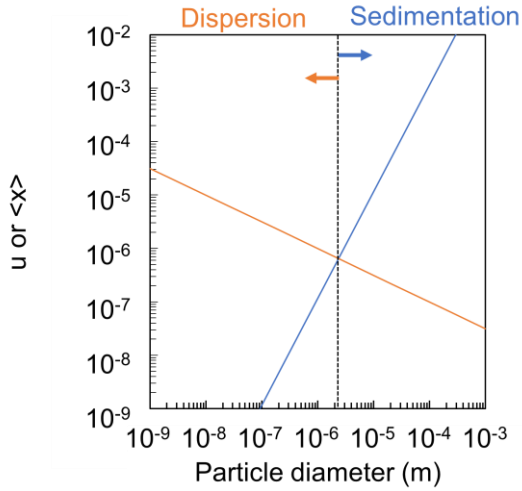

Fig. 2-1. Stokes's law (u) and Brownian motion (<x>) of PMMA latex particles dispersed in water versus particle size. $\rho = 1.19 \times 10^3 (\mathrm{kg/m^3})$, $\rho_0 = 1.0 \times 10^3 (\mathrm{kg/m^3})$, $g = 9.78\ (\mathrm{m/s^2})$, $\eta = 8.94 \times 10^{-4} (\mathrm{kg/m/s})$, $k_B = 1.38 \times 10^{-23} (\mathrm{J/K})$, $T = 298 (\mathrm{K})$.

2.2.4 Aggregation of Cationic PMMA Latex Particles in the Presence of Electrolytes

A cationic PMMA emulsion was synthesized using V-50 (2 mM) as the initiator and 1 M MMA at 60 ℃ for 16 h. The prepared emulsion was diluted by a salt solution to a final salt concentration of 7.5 mM and a final particle concentration of 0.14 mg/mL. Then, the $D(H)$ and PDI values were immediately measured by DLS.

2.2.5 Counterion Exchange of ADIP

Ion exchange

All the solutions used for this experiment were cooled on ice to prevent the decomposition of ADIP. Anion exchange was conducted using an Insert Sep® SAX-2 column with a vacuum manifold. The column was activated by methanol (15 mL) prior to use. A solution of ADIP in methanol (6 mL, 50 mg/mL) was applied to the column, and the eluate was collected in a 15-mL conical tube. To recover ADIP remaining in the column, methanol (6 mL) was loaded, and the eluate was collected in the same tube. The combined eluate was concentrated under low pressure at 5–10 ℃ and then evaporated under reduced pressure (<10 Pa) at 0 ℃. The obtained solid of ADIP-Cl was kept in a freezer at -20 ℃ to avoid decomposition.

Elemental analysis

Quantitative determination of carbon, hydrogen, and nitrogen was performed in a CHN-corder (MT-5, Yanako, Japan). Quantitative determination of fluorine, chloride, and sulfur was

performed using a coupled combustion-ion chromatography instrument (Yanako, Japan) [3]. The results are shown in Table 2-1.

Based on the elemental analysis results, the anion exchange efficiency was calculated using Eq. (2.5).

$$\text{Anion exchange efficiency } \% = \left(1 - \frac{\%\text{F}_{\text{ADIP-Cl}}}{\%\text{F}_{\text{ADIP}}}\right) \times 100 \tag{2.5}$$

Table 2-1. Results of elemental analysis.

Sample	ADIP calcd %	ADIP found %	ADIP-Cl calcd %	ADIP-Cl found %
C	35.64	35.22	50.66	48.08
H	5.32	4.92	8.50	8.54
N	13.85	13.58	22.15	20.84
F	18.79	16.41	0.00	0.23
Cl	0.00	0.71	18.69	16.97
S	10.57	10.05	00.00	0.27

Nuclear magnetic resonance

Proton nuclear magnetic resonance (^{1}H NMR) spectra were obtained using a Bruker AV400M operating at 400 MHz. ^{1}H NMR (400 MHz, heavy water) δ = 3.96 (s, 8H), 3.19 (s, 12H), 1.70 ppm (s, 12H) (Figs. S2-2 and S2-3). ^{19}F NMR spectra were obtained using an AVANCE NEO300 (Fig. S2-4).

Thermal decomposition and Arrhenius parameters

The rate constant of ADIP thermal decomposition (k_d) in water at a constant temperature was estimated using a previously published method [1]. Absorbance spectra of an aqueous ADIP-Cl solution (8 mM) were obtained using a UV-Vis spectrophotometer (GeneQuant 1300, GE Healthcare, USA) (Fig. S2-5a). Considering that the thermal decomposition of ADIP-Cl is a first-order reaction, k_d was estimated using Eq. (2.6).

$$-\ln\left(\frac{[\text{ADIP} - \text{Cl}]}{[\text{ADIP} - \text{Cl}]_0}\right) = -\ln\left(\frac{[A(t)]}{[A(0)]}\right) = k_d t \tag{2.6}$$

where $[A(t)]$ is the absorbance value of the sample at 375 nm at time *t*.

The activation energy (E_a), logarithm of the pre-exponential factor (ln *A*), and 10-hour half-life time temperature were determined from Eq. (2.7).

$$\ln k_d = -\frac{E_a}{RT} + \ln A \tag{2.7}$$

2.3 Results

2.3.1 Synthesis of PMMA Particles

Table 2-2 shows the results of particle synthesis. The conversion was >90% in most conditions, indicating successful polymerization. The $D(H)$ values of PMMA particles synthesized using VA-044 and V-50 (sample Nos. 8 and 4, respectively) were around 300 to 400 nm. On the other hand, the $D(H)$ of particles synthesized using ADIP was above 1,000 nm (sample No. 12). Moreover, the PDI of particles synthesized using ADIP was 0.252, indicating a broad size distribution. These observations suggest that PMMA particles prepared using ADIP would display aggregation in water.

Table 2-2. Characteristics of PMMA latex particles.

Sample No.	Initiator	Conc. (mM)	MMA Conc. (M)	Solid content wt%	Conversion %	D_{SEM} (nm)	$D(H)$ (nm)	PDI (-)
1	V-50	1	0.2	1.9	92.8	141±5	-	-
2	V-50	1	0.4	3.8	93.3	193±7	-	-
3	V-50	1	0.6	5.9	97.6	230±5	258.3	0.053
4	V-50	2	1	8.7	86.8	281±16	367.8	0.170
5	VA-044	1	0.2	1.9	94.1	136±5	-	-
6	VA-044	1	0.4	3.9	97.9	191±7	-	-
7	VA-044	1	0.6	5.8	96.6	227±5	244.7	0.013
8	VA-044	2	1	9.2	91.0	254±11	304.9	0.063
9	ADIP	1	0.2	2.0	98.7	234±8	-	-
10	ADIP	1	0.4	3.8	94.0	293±8	-	-
11	ADIP	1	0.6	5.7	93.5	337±9	-	-
12	ADIP	2	1	9.1	90.9	410±24	1580	0.252
13	ADIP-Cl	1	0.2	1.9	93.9	139±8	-	-
14	ADIP-Cl	1	0.4	4.0	98.4	178±5	-	-
15	ADIP-Cl	1	0.6	5.9	97.6	232±6	255.8	0.017
16	ADIP-Cl	2	1	9.2	91.7	267±16	368.9	0.057

2.3.2 Dispersion Stability of PMMA Latex Particles

The dispersion stability of cationic PMMA latex particles is shown in Fig. 2-2. The structure of the cationic azo radical initiator is shown in Fig. 2-2a, and those of various other initiators are shown in Fig. 2-2b to the left of the photographs. The PMMA particles synthesized using V-50 or VA-044 did not change after 14 days of storage. On the other hand, those synthesized using ADIP settled after only 7 days. Based on the theory illustrated in Fig. 2-1, the threshold diameter of PMMA particles to form a stable dispersion is around 2 μm. Although all particles synthesized using ADIP had D_{SEM} < 2 μm (Table 2-2), sedimentation still occurred. Moreover, after storing the dispersions for 3 months, hard cakes were formed at the bottom of vials enclosing PMMA dispersion prepared using ADIP because of sedimentation (Fig. 2-3).

These results suggest that some factors other than particle size is responsible for the easy sedimentation of cationic PMMA latex particles in water. The most obvious factor is the structure of the counter ion (triflate in the case of ADIP), which will be discussed below.

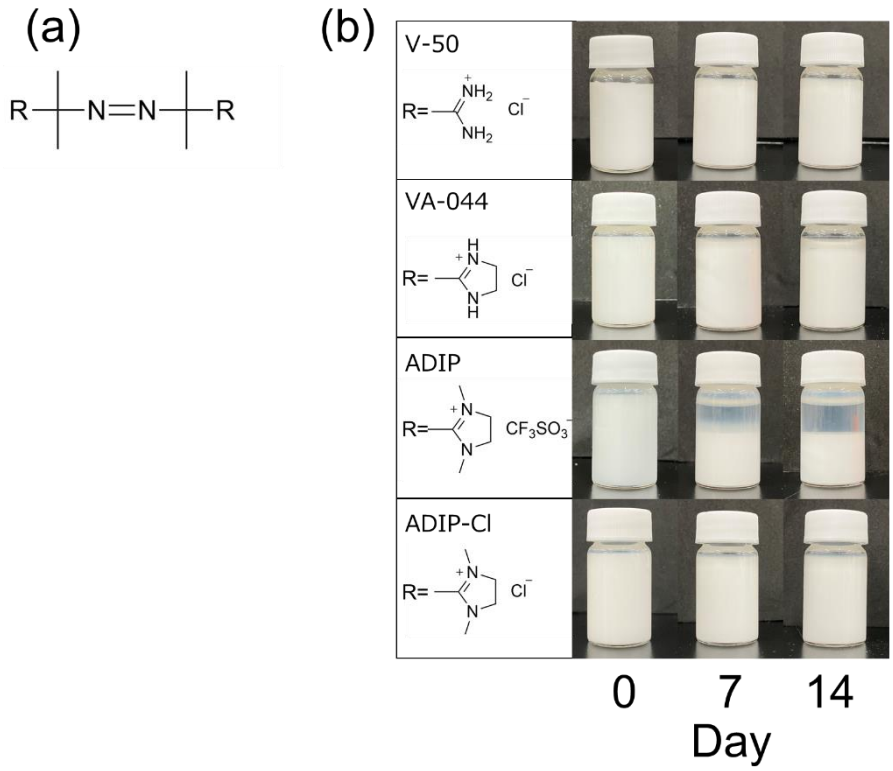

Fig. 2-2. (a) Structure of the azo radical initiator. (b) Photographs of PMMA latex particles stored in vials at 25 ℃. For properties of dispersions prepared using V-50, VA-044, ADIP, and ADIP-Cl see Table 2-2 (sample Nos. 3, 7, 11, and 15, respectively).

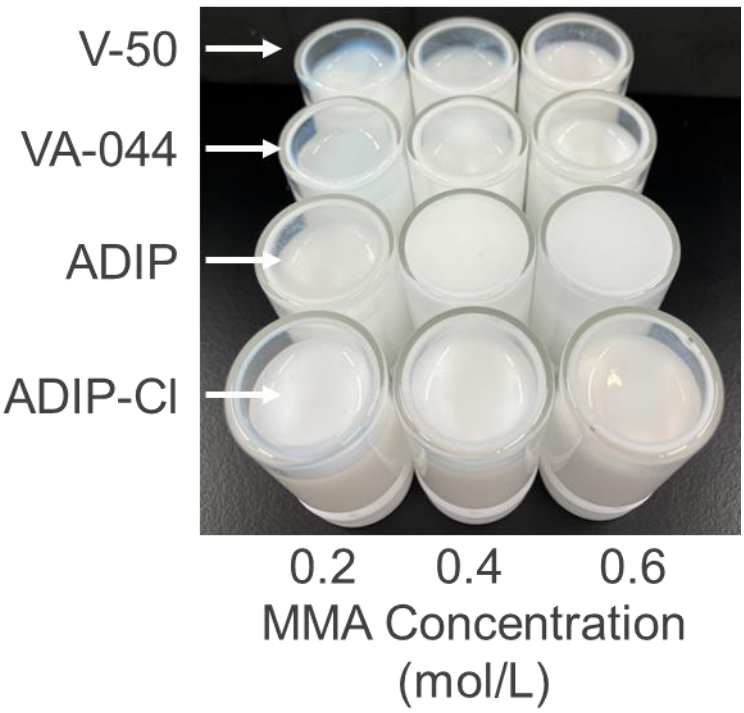

Fig. 2-3. Bottom of vials containing PMMA latex particles after storage at 25 ℃ for 3 months.

2.3.3 Effect of Anion on the Aggregation of Cationic PMMA Latex Particles

To investigate the effect of triflate, the counter anion of ADIP, on emulsion stability, various potassium salts were added to the stable PMMA emulsion synthesized using V-50 (sample No. 4). As shown in Table 2-3, the $D(H)$ and PDI values increased drastically upon the addition of KCF_3SO_3 or K_2SO_4 compared to other potassium salts. According to the Schultz and Hardy rules [4] and DLVO theory of particle stability, the divalent sulfate ion should promote aggregation by a factor of 64 compared to monovalent ions. The greater increase in both $D(H)$ and PDI upon adding triflate compared to sulfate ion suggests that the former ion more strongly promotes the aggregation of cationic PMMA particle emulsions.

Table 2-3. Diameter of PMMA latex particles dispersed in various electrolytes at a concentration of 140 mg/L.

Electrolyte	$D(H)$ (nm)	STDEV.P	PDI (-)	STDEV.P
None	382	50	0.23	0.08
KCl	378	46	0.25	0.11
KBr	417	90	0.29	0.12
KI	424	79	0.28	0.12
KNO_3	442	99	0.31	0.09
KCH_3SO_3	366	1	0.21	0.03
KCF_3SO_3	1169	224	0.58	0.08
K_2SO_4	740	260	0.43	0.14

2.3.4 Synthesis of ADIP-Cl

The results described in Section 2.3.3 show that other monovalent anions have a much weaker effect than the triflate anion on the aggregation of PMMA particles. Next, I synthesize a novel ADIP derivative ADIP-Cl, in which the triflate counter anion is replaced by the chloride anion. ADIP-Cl was obtained from ADIP using an anion exchange column (see Section 2.2.5). According to the ^{1}H NMR spectra, there was no change in the structure of the cationic azo group after the anion exchange (Figs. 2-4 and 2-5). Moreover, ^{19}F NMR spectra indicated the absence of fluorine after treatment by the silica gel column (Fig. 2-6). From the elemental analysis results, the sum of all measured elemental fractions was 94.9% (see Section 2.2.5). The remaining 5.1% should come from water in ADIP-Cl, because the oxygen fraction in water content of ADIP-Cl calculated by the standard addition method using ^{1}H NMR was 5.2%. The anion exchange efficiency calculated using Eq. (2.5) was 98.6%, indicating that triflate in ADIP was almost completely replaced by chloride through treatment by silica gel column with the trimethylaminopropyl group.

Figure 2-7 shows the thermal decomposition kinetics of ADIP-Cl in water at 50 °C. The kinetics is first-order for both ADIP and ADIP-Cl, with a rate constant (k_d) of 1.13×10^{-4} (Ref. [1]) and 0.96×10^{-4} s^{-1}, respectively. Hence, these two radical initiators have almost identical decomposition rates in water. I further investigated the characteristics of ADIP-Cl to confirm its role as an initiator for preparing polymer particles. First-order decomposition kinetics was also observed at 60 °C (Fig. 2-8), which is the SFEP reaction temperature used in this work. An Arrhenius plot of the k_d data for ADIP-Cl in water was used to obtain the activation energy (E_a), logarithm of the pre-exponential factor ($\ln A$), and 10-hour half-life time temperature as 108 kJ mol^{-1}, 31.0, and 36.4 °C, respectively (Fig. 2-9).

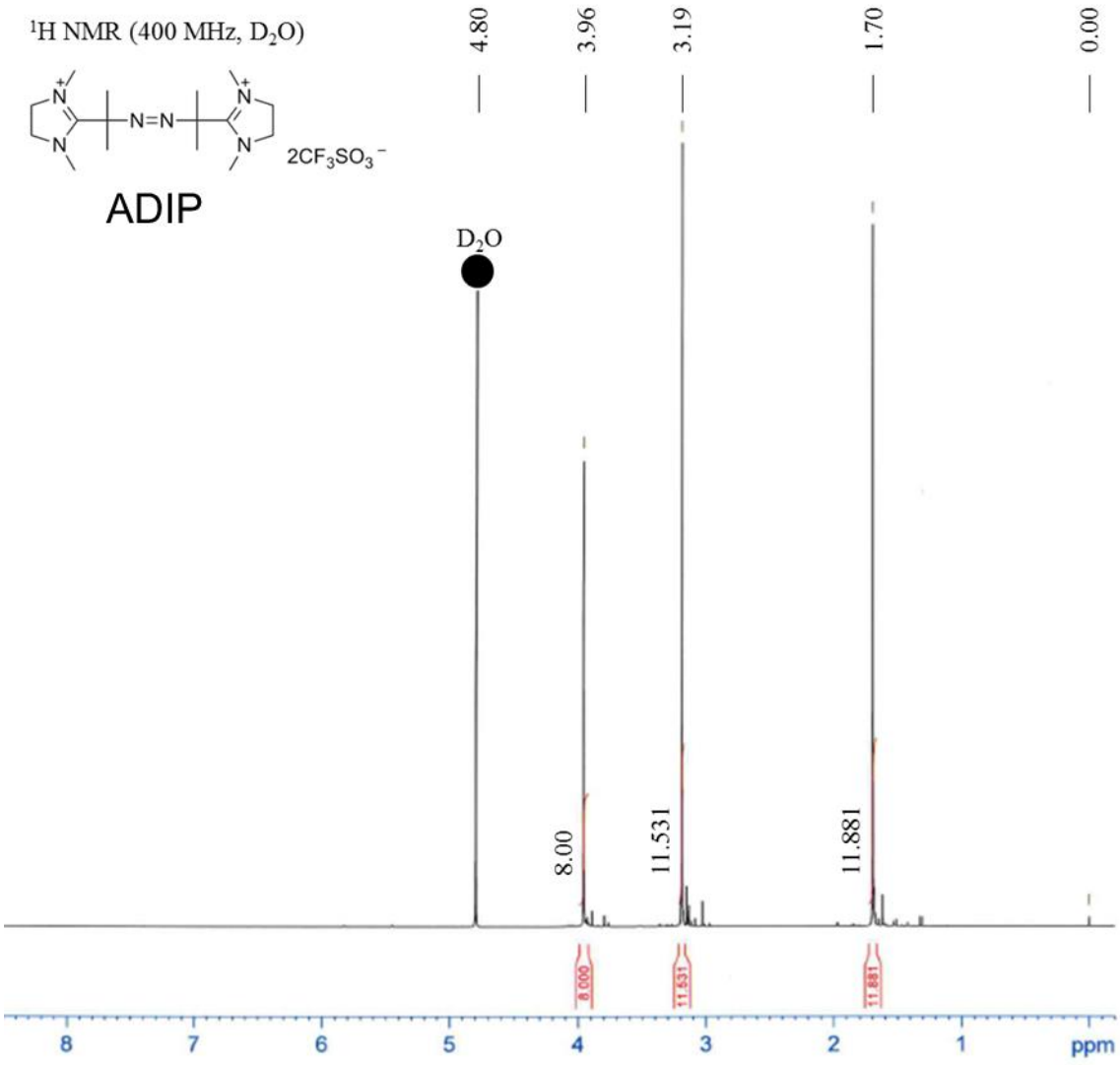

Fig. 2-4. ^{1}H NMR spectrum of ADIP.

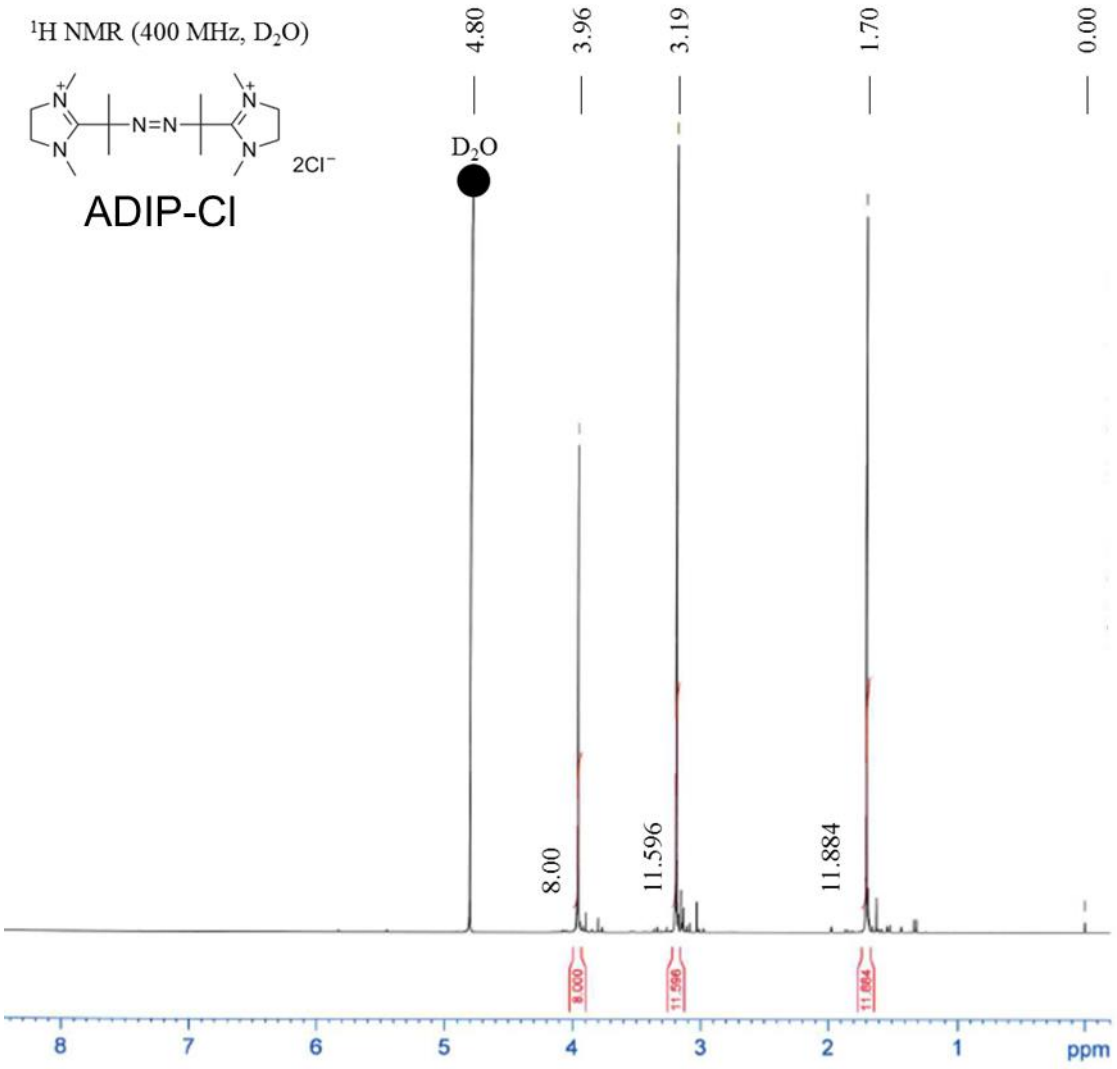

Fig. 2-5. ^{1}H NMR spectrum of ADIP-Cl.

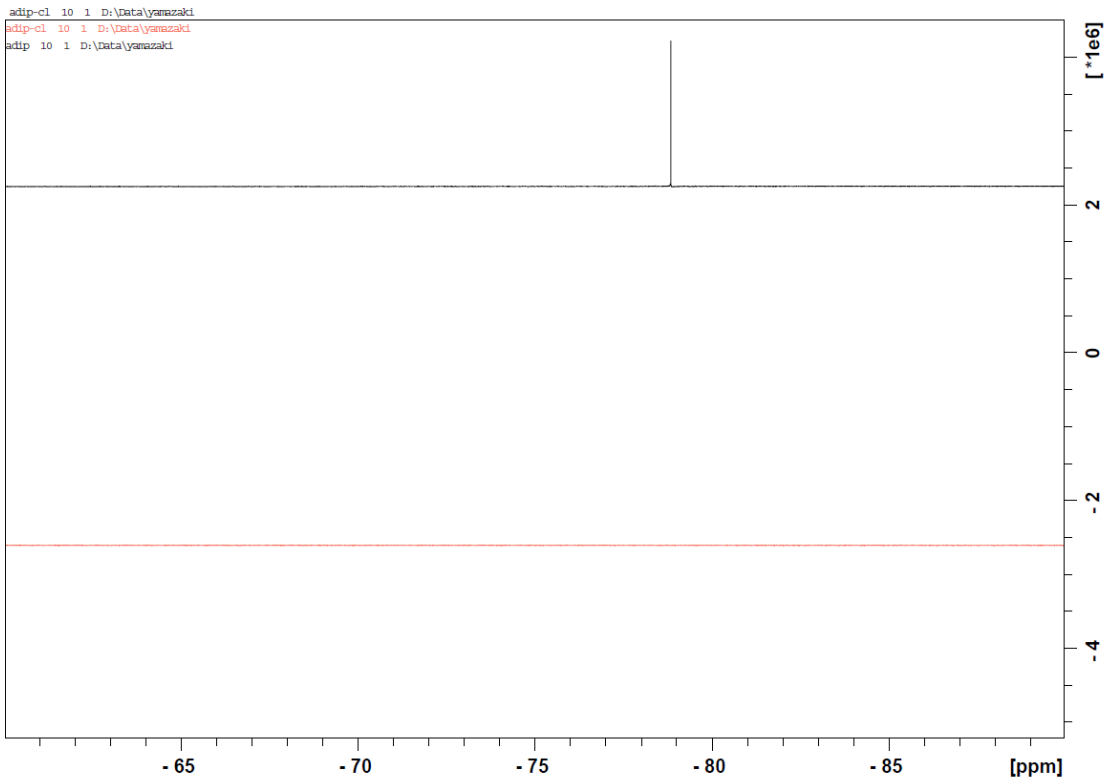

Fig. 2-6. ^{19}F NMR spectra of ADIP (black) and ADIP-Cl (red).

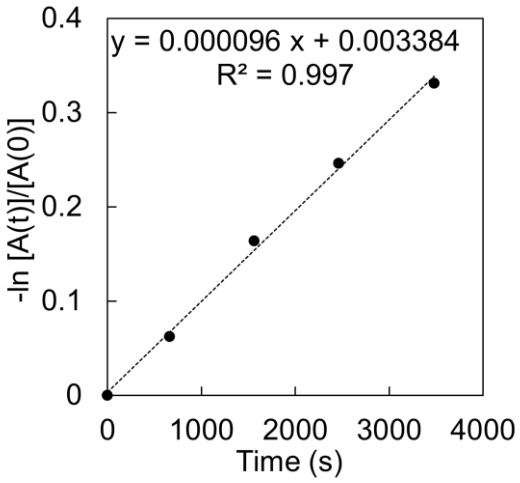

Fig. 2-7. Thermal decomposition kinetic data of ADIP-Cl in water at 50 ℃.

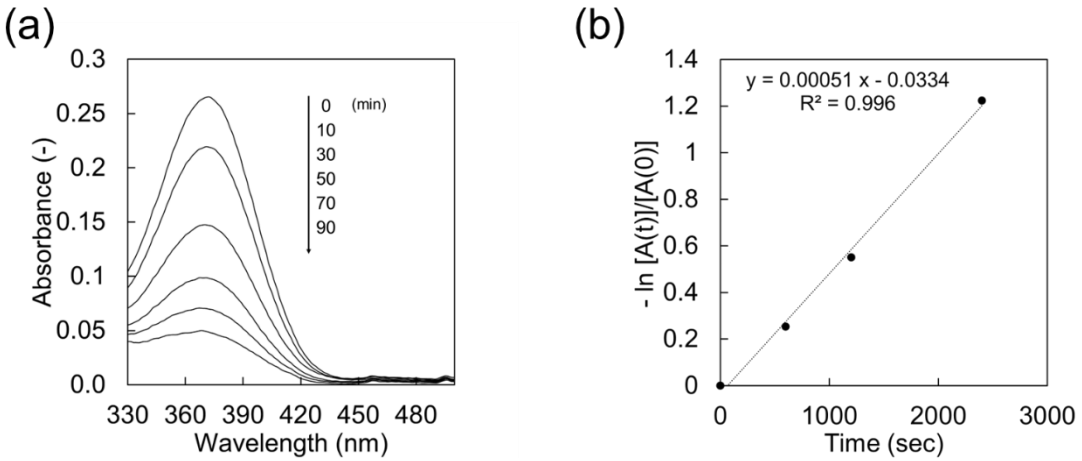

Fig. 2-8. (a) Absorbance spectra of ADIP-Cl (8 mM) in water at 60 °C. (b) First-order thermal decomposition kinetic data of ADIP-Cl in water at 60 ℃.

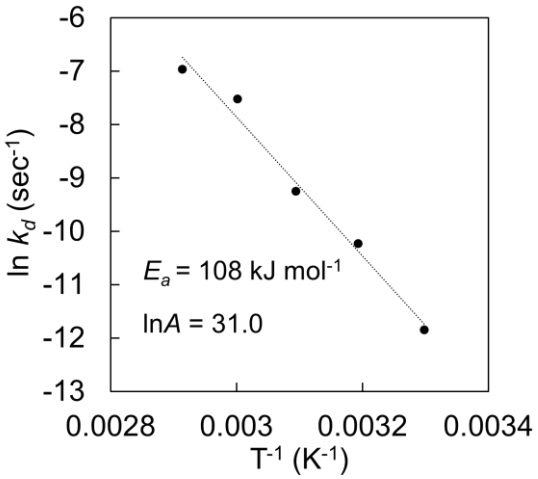

Fig. 2-9. Arrhenius plot for the thermal decomposition rate constant of ADIP-Cl in water.

2.3.5 Synthesis of PMMA Latex Particles using ADIP-Cl

Properties of PMMA particles prepared using ADIP-Cl are shown in Table 2-2 (sample Nos. 13–16). Compared to the particles prepared using ADIP (sample No. 12), the PDI value of sample No. 15 was 0.057, indicating successful SFEP with a narrow particle size distribution. Moreover, sample No. 15 also showed no sedimentation during the storage test (Fig. 2-2). Therefore, replacing the triflate anion in ADIP with the chloride anion effectively improved the dispersion stability of PMMA latex particles.

2.4 Discussion

2.4.1 Aggregation Mechanism in the Presence of Triflate

Particle aggregation is controlled by the competition between attractive vdW interactions (V_{vdW}) that favor aggregation and repulsive electrostatic interactions (V_{EDL}) between similarly charged particles that favor dispersion [5-7]. I believe that triflate significantly changes the PMMA particle surface by binding to the surface *via* hydrophobic interactions in addition to electrostatic interaction. To support this claim, I calculated the partition coefficient (log P, a measure of hydrophobicity) using ChemDraw software (version 11.0.1, Cambridge Software Ltd., USA). The obtained log P values were 0.32, -0.99, and 1.18 for hydrochloric acid, methanesulfonic acid, and trifluoromethanesulfonic acid, respectively. Furthermore, Friesen *et al*. suggested that triflate may be inserted into the surface of 1-dodecyl-3-methylimidazolium micelles [8]. Therefore, the strong adsorption of triflate on the surface of PMMA particles probably causes the attractive vdW force to become dominant, which promotes aggregation. However, further investigations are required to verify this hypothesis.

2.4.2 Synthesis of ADIP-Cl

PMMA latex particles prepared using ADIP-Cl, a derivative of ADIP, showed drastically improved dispersion stability. Therefore, I expect that ADIP-Cl can be used for SFEP with other vinyl monomers to achieve good dispersion stability. The counterion of cationic azo radical initiator should be selected carefully from the list in Table 2-3 without causing aggregation. Specifically, divalent anions or anions on the right side of the indirect Hofmeister series (Fig. 1-2) should be avoided, because such ions induce the destabilization of cationic particles. In this study, counterion exchange was performed in an ion exchange column to convert ADIP to ADIP-Cl. It is also conceivable to realize counterion exchange by choosing suitable reagents and conditions for the methylation step during ADIP synthesis (Fig. 1-7). However, such a reaction path has not been identified yet.

2.5 Summary

In Chapter 2, I successfully controlled the dispersion stability of cationic PMMA latex particles prepared using a cationic azo radical initiator with quaternary ammonium structure. To the best of my knowledge, few previous studies have reported the effect of the counterion of the azo radical initiator on the dispersion stability of cationic polymer particles. The results revealed that the counterion has a significant effect on the dispersion stability of cationic PMMA latex particles. Moreover, the triflate anion caused substantial aggregation of these particles, even though it has

not been known to exert a strong destabilization power on cationic polymer particles and is not listed in the Hofmeister series, as described in Section 1.2.3. In the next chapter, the aggregation mechanism of triflate is further investigated and reported.

2.6 References

[1]. Uchiyama, S., Tsuji, T., Kawamoto, K., Okano, K., Fukatsu, E., Noro, T., Ikado, K., Yamada, S., Shibata, Y., Hayashi, T., Inada, N., Kato, M., Koizumi, H., & Tokuyama, H. (2018). A cell-targeted non-cytotoxic fluorescent nanogel thermometer created with an imidazolium-containing cationic radical initiator. *Angew. Chem. Int. Ed.*, 57(19), 5413-5417.

[2]. Kamiya, H. (2013). Fundamental introduction of fine particle dispersions in liquids. *J. Jpn. Soc. Colour Mater.*, 86(1), 26-30.

[3]. Nagashima, H. & Dewa, Y. (2017). Rapid and simultaneous micro-analysis of halogens and sulfur in organic compounds by combustion - ion chromatography. *BUNSEKI KAGAKU*, 66(2), 81-87 in Japanese.

[4]. Hall, S. B., Duffield, J. R., & Williams, D. R. (1991). A reassessment of the applicability of the DLVO theory as an explanation for the Schulze-Hardy rule for colloid aggregation. *J. Colloid Interface Sci.*, 143(2), 411-415.

[5]. Kobayashi, M. (2010). 水中に懸濁した微粒子の凝集分散:基礎理論とその適用性. *Journal of Japan Coating Technology*, 11(45), 419-432 in Japanese.

[6]. Ito, F., Makino, K., Ohshima, H., Terada, H., & Omi, S. (2004). Salt effects on controlled coagulation in emulsion polymerization. *Colloids Surf., A*, 233(1-3), 171-179.

[7]. Feeney, P. J., Napper, D. H., & Gilbert, R. G. (1984). Coagulative nucleation and particle size distributions in emulsion polymerization. *Macromolecules*, 17(12), 2520-2529.

[8]. Friesen, S., Buchecker, T., Cognigni, A., Bica, K., & Buchner, R. (2017). Hydration and counterion binding of [C12MIM] micelles. *Langmuir*, 33(38), 9844-9856.

Chapter 3 Dispersion Behavior of Cationic PMMA Particles in the Presence of Triflate Anion

3.1 Introduction

Chapter 2 showed that although cationic PMMA latex particles could be synthesized *via* SFEP using ADIP as the initiator, the resultant dispersion had reduced stability in the presence of triflate. The mechanism by which triflate destabilizes cationic PMMA latex particles remains unclear. According to the DLVO theory, which describes the role of force balance in the stability of particle dispersions, the repulsive force of particles prepared by SFEP originates from surface charge. The counterion will reduce the electrostatic repulsive force, because the charge density at particle surface has been found to vary systematically with the type of ions within the Hofmeister series, as described in Section 1.2.3. This chapter describes the effects of three monovalent anions {Cl^-, methanesulfonate ($CH_3SO_3^-$), and triflate ($CF_3SO_3^-$)} on the aggregation of cationic PMMA latex particles. The counterion of these anions was potassium (K^+).

3.2 Materials & Methods

3.2.1 Reagents

Water treated by reverse osmosis and electrodeionization was used in all the experiments. Ethanol, potassium peroxodisulfate (KPS, purity ≥ 99.0%), KCl (purity ≥ 99.5%), (MMA, purity ≥ 98.0%), V-50 (purity ≥ 97.0%), and VA-044 (purity ≥ 97.0%) were obtained from Fujifilm Wako Pure Chemical Corporation (Japan). KCF_3SO_3 (purity > 98.0%) and KCH_3SO_3 (purity > 98.0%) were procured from Tokyo Chemical Industry Corporation (Japan). 6-(p-toluidino)-2-Naphthalenesulfonic acid sodium salt (TNS, purity ≥ 98%) and an inhibitor remover (catalog no. 311332) were obtained from Sigma-Aldrich Corporation (USA). ADIP and ADIP-Cl were synthesized as described in Chapter 2.

3.2.2 Particle Synthesis and Evaluation

Synthesis of PMMA particles

Cationic PMMA particles were synthesized using the method described in Section 2.2.2. Anionic PMMA particles were synthesized as follows. MMA, Milli-Q water (27.0 g), and a solution of 0.15 mmol of KPS in 1 g of Milli-Q water were added to a 30-mL glass vial and magnetically stirred. Polymerization was conducted for 4 h at 80 °C. KPS provided negatively charged polymer latex particles, because its sulfate group appeared on the particle surface.

Conversion

The conversion was calculated using the method described in Section 2.2.2.

Zeta potentials

The particles' zeta potential was evaluated using Zetasizer Nano ZSP with the M3-PALS® method. The Smoluchowski function (Eq. 1.5) was used to calculate the zeta potential, and each sample was measured 20 times at 25 °C using a capillary cell (DTS1070, Malvern Instruments Limited). The viscosity and relative dielectric constant of water were set at 0.89 mPa·s and 78.5, respectively. The concentration of latex particles was 10 mg/L, and the applied voltage was 150 V. The electrolyte concentration varied from 0.1 to 10 mM. Note that when the electrolyte concentration exceeds 10 mM, the electrodes in the capillary cell tend to become scorched, necessitating a reduction in the applied voltage. Unfortunately, a lower applied voltage reduces the resolution, unless experimental adjustments are made such as making more repeated measurements, which were not implemented in experiments described in this Chapter. The zeta potential was derived from the measured electrophoretic mobility using Henry's equation {Eq. (3.1)}.

$$U_E = \frac{2\varepsilon z F(ka)}{3\eta} \tag{3.1}$$

where U_E is the electrophoretic mobility, ε is the permittivity, z is the zeta potential, and $F(ka)$ is Henry's coefficient.

Surface charge density

The fluorescent emission spectra of TNS were recorded to determine the cationic moieties located on the PMMA particle surface. TNS, a negatively charged compound with a hydrophobic part, exhibits quenching in an aqueous environment. On the other hand, it emits fluorescence upon electrostatic interactions with a positively charged moiety in a hydrophobic environment. The equilibrium constant (K), saturated adsorption (q_{max}), and surface charge density (σ) of the cationic PMMA latex particles were determined according to a previous study by Suga *et al*. [1].

A specific amount of TNS solution (100 μM) in 10 vol% ethanol aqueous was added to a 100 ppm PMMA aqueous dispersion. The fluorescent spectrum of the mixture was obtained at different final TNS concentrations using a fluorescence spectrophotometer (FP-8500, JASCO Corporation, Japan). As shown in Fig. 3-2a, the peak intensity occurs at approximately 420 nm. This intensity was recorded as I_{420}, and the adsorbed TNS concentration (C_{ads}) was calculated as follows:

$$C_{ads} = \frac{I_{420}}{I_{420,1\mu M}} C_{TNS} \tag{3.2}$$

$$C_{TNS} = C_{ads} + C_{eq} \tag{3.3}$$

where C_{TNS} and $I_{420,1\mu M}$ are the TNS concentration and fluorescence intensity at $C_{TNS} = 1\ \mu M$, respectively, given that 1 μM of TNS is fully adsorbed onto the cationic PMMA particles at 1000 ppm. C_{eq} is the equilibrium concentration of TNS in the solution.

Using the obtained Langmuir plot, K (μM^{-1}) and q_{max} (mol/g) were determined as follows:

$$q = \frac{q_{max} K C_{eq}}{1 + K C_{eq}} \tag{3.4}$$

For cationic PMMA latex particles at 100 ppm, Eq. (3.4) was modified as follows:

$$\frac{1}{C_{ads}} = \frac{1}{K C_{max}} \frac{1}{C_{eq}} + \frac{1}{C_{max}} \tag{3.5}$$

The surface charge density on the PMMA particles, σ (unit/nm^2), can be calculated as follows:

$$\sigma = q_{max} N_A \div \left(\frac{6}{\rho D_{SEM}} \right) \tag{3.6}$$

where N_A is Avogadro's number (6.02×10^{23} /mol), and ρ is density of PMMA (1.19×10^{-21} g/nm^3).

Dynamic light scattering

DLS measurement was performed as described in Section 2.2.2. Colloidal particles dispersed in an aqueous solution containing electrolytes aggregate over time, depending on the type and concentration of the electrolyte. In the initial aggregation stage of uniformly sized particles, the time variation of the average hydrodynamic diameter $D(H)$ is proportional to the aggregation rate constant k and the initial particle concentration C, as described by Eq. (3.7) [2].

$$\left(\frac{dD(H)}{dt} \right)_{t \to 0} = \beta k C \tag{3.7}$$

where β is an optical factor that depends on the particle size in the solution, the scattering angle of scattered light, and light wavelength.

The aggregation behavior is expressed by the stability ratio W, which is the relative aggregation rate.

$$W = \frac{k^{(f)}}{k} \tag{3.8}$$

where $k^{(f)}$ is the rate constant in the fast-aggregation regime. The time variation of the average hydrodynamic diameter $D(H)$ approaches a constant value in the region of rapid aggregation (when the repulsive force is overwhelmed by the vdW force between particles). W can be expressed using Eqs. (3.8) and (3.9):

$$W = \frac{[(dD(H)/dt)_{t\to 0}/C]^{(f)}}{[(dD(H)/dt)_{t\to 0}/C]} \tag{3.9}$$

where the superscript $^{(f)}$ in the numerator denotes the value under the fast aggregation condition. In this study, numerator of Eq. (3.9) for the fast-aggregation regime was used in a 500 mM KCl solution for each type of cationic PMMA latex particle.

The time-resolved DLS intensity was measured to calculate the stability ratio (W) of the PMMA particle dispersion. The DLS equipment was a Malvern Zetasizer ZSP with a 10 mW He-Ne laser at a wavelength of 633 nm. The sample (10 mg/L as in solid concentration) was placed in a Malvern DTS1070 cuvette and equilibrated for 30 s before measurement. The pH of the cationic PMMA latex particles at various electrolyte concentrations was adjusted to 6 using HCl and KOH. The backscattered light at 173° was measured, and a total of 11 measurements (each lasting approximately 10 s) were performed at 25 °C. A second-order cumulant fit was used to determine the diffusion coefficient and $D(H)$.

From the $D(H)$ values measured at different times, a regression line was created using the least squares method, and W was calculated using Eq. (3.9).

The critical coagulation concentration (CCC), which is the boundary between the slow coagulation region (where W depends on the electrolyte concentration) and the fast coagulation region (where it remains constant), was calculated from the intersection of the regression line for the slow coagulation region and W = 1.

Scanning electron microscopy

SEM observation was conducted as described in Section 2.2.2. A total of 20 particles were selected to measure the D_{SEM} value.

3.2.3 Surface Tension of Electrolytes

The air-electrolyte interface is a popular experimental model for evaluating the surface tension [3, 4] and zeta potential of suspensions [5-8]. Moreover, the air-water interface is called a hydrophobic surface because it lacks dissociated surface groups. To evaluate the ion adsorption behavior on this hydrophobic surface, I analyzed the surface tension of electrolytes. The following Gibbs adsorption isotherm:

$$d\gamma = -\sum_i \Gamma_i d\mu_i \tag{3.10}$$

relates the change of surface tension γ to the sum of surface excess concentration Γ_i for molecule type i multiplied by change of the respective chemical potential μ_i. Linear fitting was performed for the experimentally measured $\Delta\gamma$ as a function of electrolyte concentration (c^b_{salts}), as described in Eq. (3.11) [3, 4]:

$$\Delta\gamma = Ac^b_{salts} \tag{3.11}$$

Surface tensions were measured *via* the rising drop method [9] using a contact angle meter (DMo-502; Kyowa Interface Science Co., Ltd., Japan). A hook needle with an outer diameter of 0.7 mm was used to create a bubble in the electrolyte solution. Measurements was conducted at 25 ± 1 °C and 45 ± 5% humidity. Images of the bubbles were processed using the Young-Laplace equation in FAMAS software (version 7.2.0; Kyowa Interface Science Co., Ltd., Japan).

$$\Delta P = \gamma\left(\frac{1}{R_1} + \frac{1}{R_2}\right) \tag{3.12}$$

where ΔP is the pressure difference, and R_1 and R_2 are the radii of curvature. The surface tension of water was experimentally determined (71.2 ± 0.5 mN/m, n = 5) and used to calculate $\Delta\gamma$.

3.3 Results

3.3.1 Synthesis of PMMA Latex Particles

Three types of cationic PMMA particles were synthesized, namely sample Nos. 2, 7, and 11 in Table 2-2. The zeta potential of these particles is around + 40 mV (Table 3-1). For the sulfate-PMMA latex particles, the D_{SEM} value is 302 ± 12 nm (Fig. 3-1 and Table 3-1), and the $D(H)$, PDI, and zeta potential are 367.1 nm, 0.21, and -64 ± 6 mV, respectively.

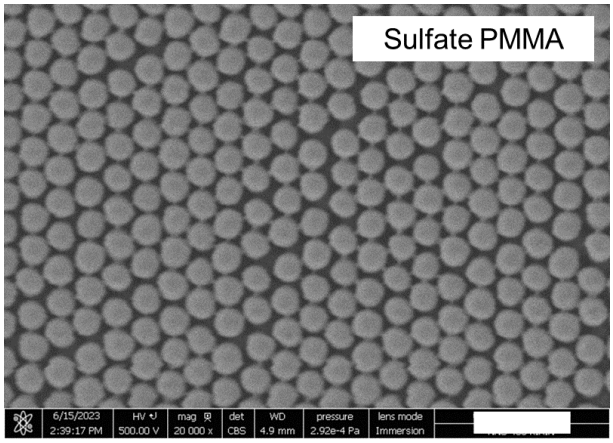

Fig. 3-1. SEM image of sulfate-PMMA latex particles. Scale bar: 1 μm.

Table 3-1. Characteristics of sulfate-PMMA latex particles.

D_{SEM} (nm)	$D(H)$ [a] (nm)	PDI [a] (-)	Zeta potential [b] (mV)
302 ± 12	367.1	0.21	-64 ± 6

[a] pH = 6, 10 mM KCl, solid content = 10 mg/L.

[b] Data were obtained in Milli-Q water, solid content = 10 mg/L, n = 20.

An anionic fluorescent probe assay was used to determine the surface charge density (σ) of the PMMA particles (Figs. 3-2 and 3-3). σ was calculated from the Langmuir isotherm of the 6-(p-toluidino)-2-naphthalenesulfonic acid sodium salt (TNS). The σ value of imidazolium-PMMA particles is 0.16 unit/nm^2, which is slightly larger than those of amidine- (0.12 unit/nm^2) and imidazoline-PMMA particles (0.11 unit/nm^2) (Table 3-2).

The binding affinity (K, μM^{-1}) of PMMA particles decreases in the order of imidazolium > imidazoline > amidine (Table 3-2). Given that the TNS molecule preferentially binds to hydrophobic sites, the K value reflects the hydrophobicity of the cationic moieties. This result indicates that the hydrophobicity of the cationic PMMA particle surface can be altered by selecting the azo initiator.

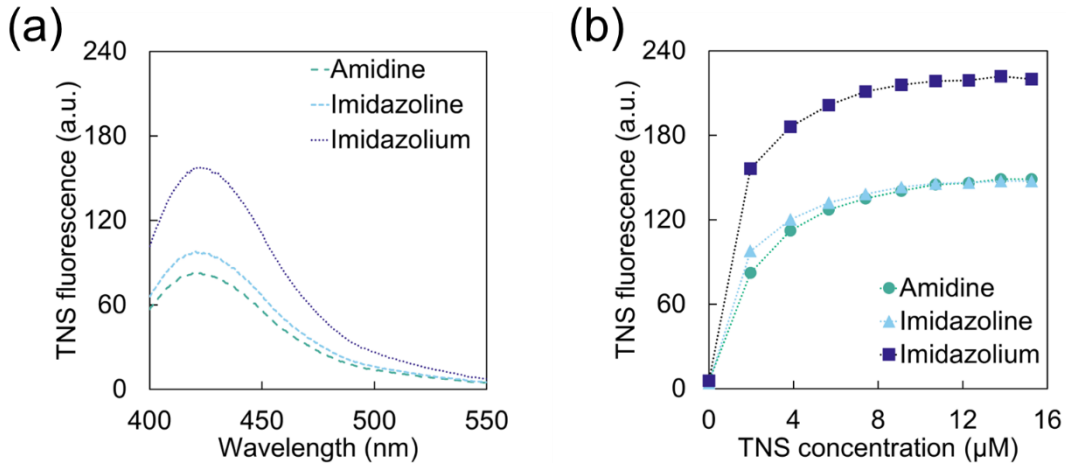

Fig. 3-2. (a) Fluorescent spectra of TNS in PMMA latex particles. The particle and TNS concentrations are 100 ppm and 2 μM, respectively. Teal curve: amidine-, cyan curve: imidazoline-, and indigo curve: imidazolium-PMMA latex particles. (b) TNS adsorption on PMMA latex particles (teal circles: amidine, cyan triangles: imidazoline, indigo squares: imidazolium).

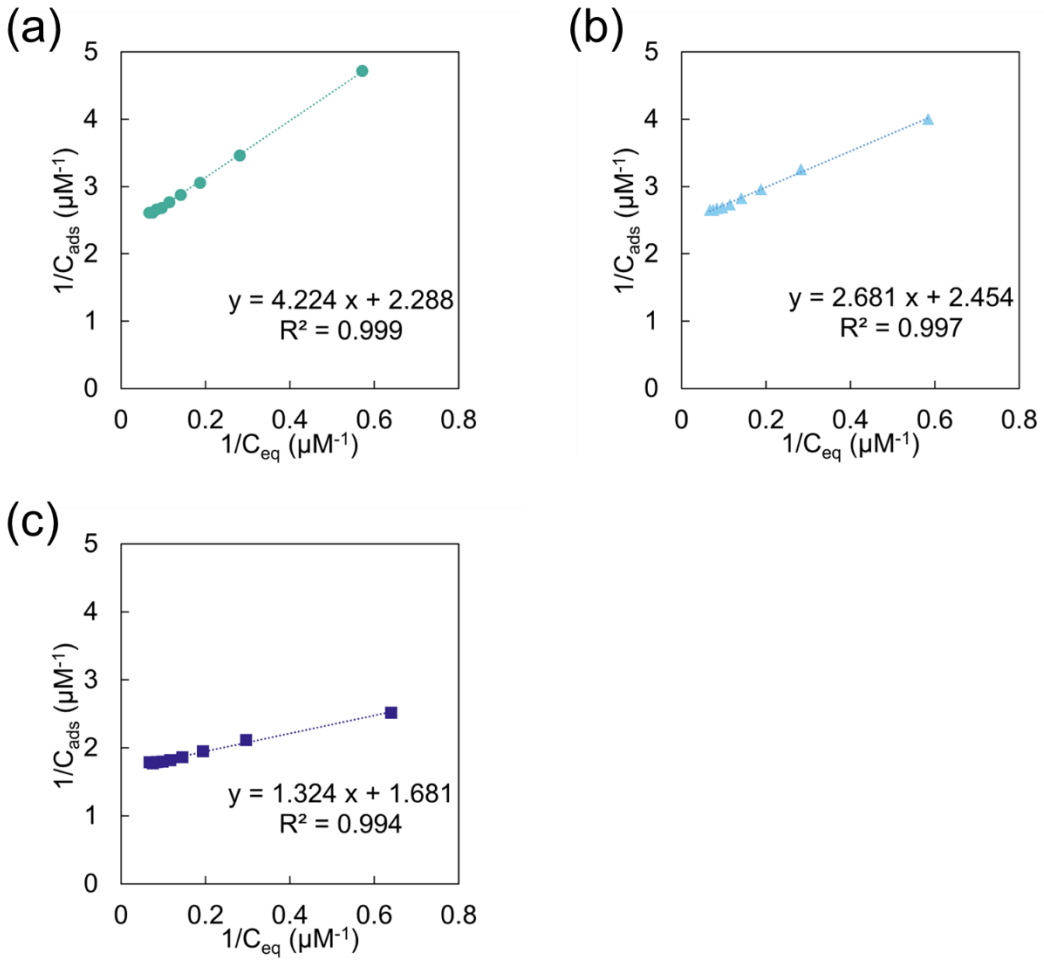

Fig. 3-3. Langmuir plots for TNS adsorption assay: (a) amidine-, (b) imidazoline-, and (c) imidazolium-PMMA latex particles.

Table 3-2. Zeta potentials of cationic PMMA latex particles in Milli-Q water (n = 20). Adsorption parameters were obtained from the Langmuir plot.

Sample No.	Moieties	Zeta potential (mV)	q_{max} (10^{-6} mol/g)	K (μM^{-1})	σ (unit/nm^2)
3	Amidine	+40 ± 5	4.37	0.54	0.12
7	Imidazoline	+44 ± 6	4.07	0.92	0.11
11	imidazolium	+41 ± 5	5.95	1.27	0.16

3.3.2 Zeta Potentials of PMMA Latex Particles Dispersed in Electrolyte Solutions

Figure 3-4 shows the zeta potentials of cationic PMMA latex particles at pH = 6 and various electrolyte concentrations. For KCF_3SO_3, the zeta potential decreases steeply as the electrolyte concentration increases, and the surface became almost neutral at 10 mM. In contrast, for KCl and potassium methane sulfonate (KCH_3SO_3), the zeta potential remained within the range of +40 to +20 mV. These phenomena occur for all three types of cationic PMMA latex particles (Fig. 3-4). Sugimoto *et al*. reported a steep decrease in the zeta potential and charge reversal of amidine-PS latex particles due to strong adsorption of oxyanions onto the particle surface [10]. Therefore, I consider $CF_3SO_3^-$ to be strongly absorbed onto the surface of these particles.

Figure 3-5 shows the zeta potentials of sulfate-PMMA latex particles at different electrolyte concentrations. A moderate increase in zeta potential was observed for all types of electrolytes. An increase in ion, which has the same charge as the anionic particles, increases the zeta potential. A similar effect was observed in a previous study [10].

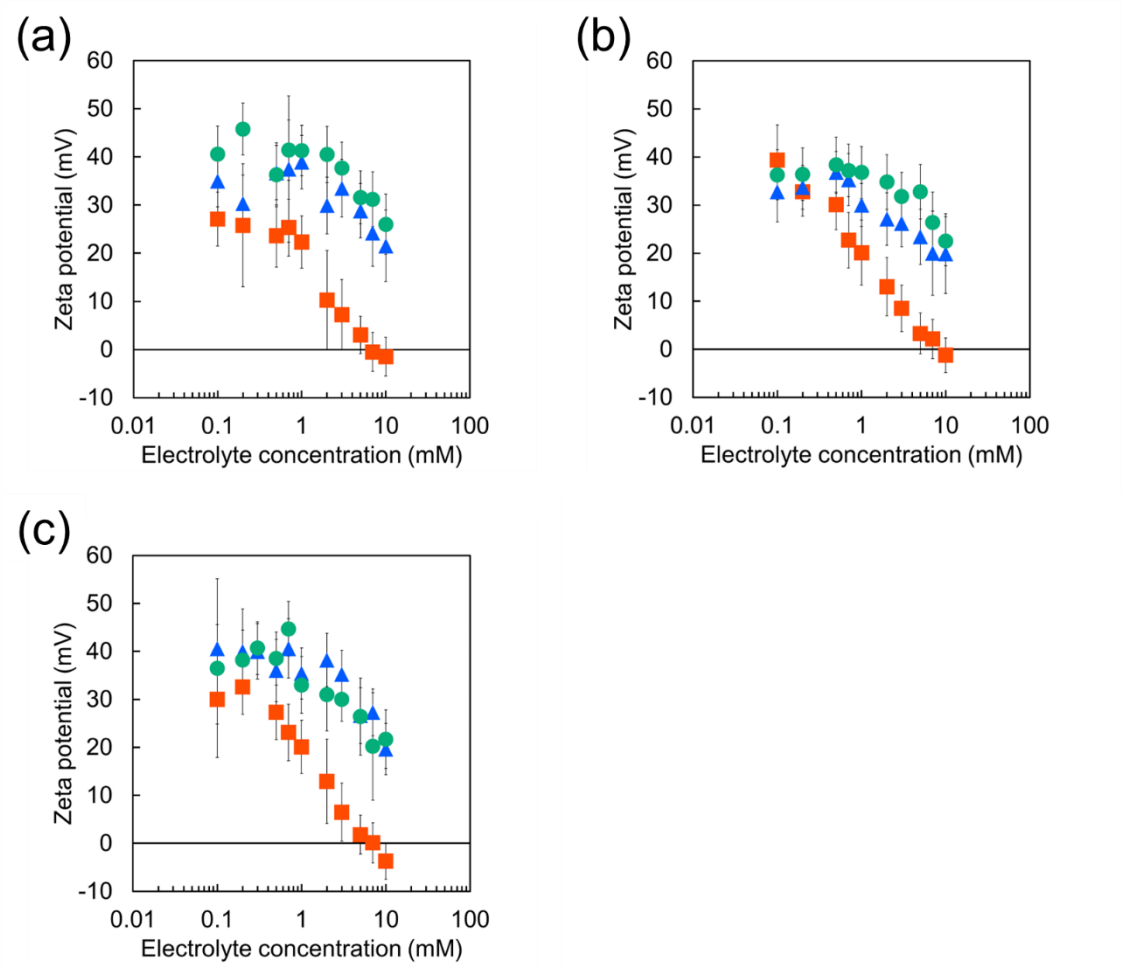

Fig. 3-4. Zeta potentials of cationic PMMA latex particles dispersed in different electrolytes. (a) Amidine-, (b) imidazoline-, and (c) imidazolium-PMMA latex particles. KCl (green circles), KCH_3SO_3 (blue triangles), and KCF_3SO_3 (red squares).

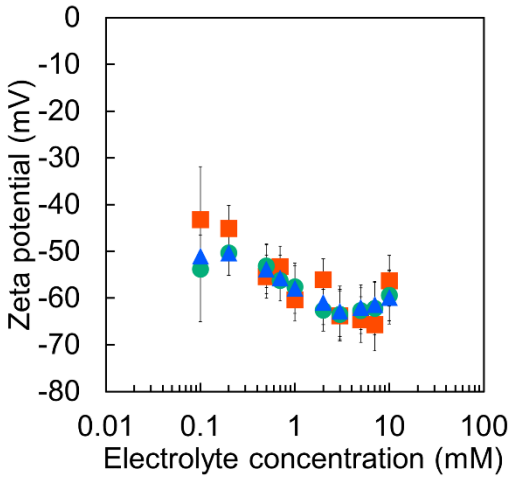

Fig. 3-5. Zeta potentials of sulfate-PMMA latex particles dispersed in different electrolytes (n = 20). KCl (green circles), KCH_3SO_3 (blue triangles), and KCF_3SO_3 (red squares).

3.3.3 Time Courses of Dynamic Light Scattering

Measured time courses of $D(H)$ in the presence of electrolytes are shown in Figs. 3-6 to 3-14. The coefficient of determination (R^2) of regression lines was generally above 0.9, although it was reduced to 0.5–0.7 under some conditions. At lower electrolyte concentrations, $D(H)$ only changed slightly, indicating high stability of the dispersion. In contrast, the particles aggregated once the electrolyte concentration exceeded a certain threshold. Furthermore, the rate of increase in $D(H)$ was proportional to the electrolyte concentration. For the sulfate-PMMA latex particles, an increase in $D(H)$ was not observed (Fig. 3-15).

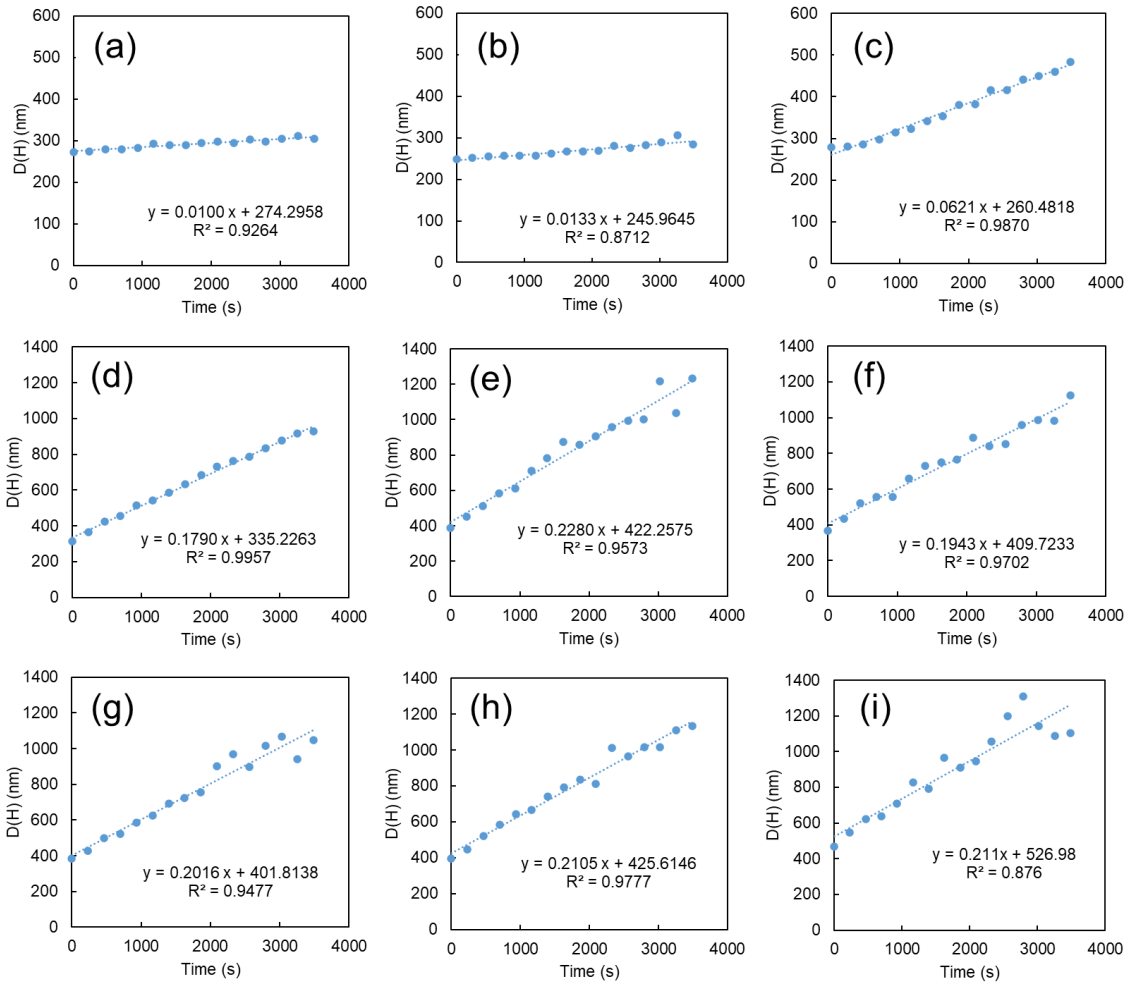

Fig. 3-6. Time course of $D(H)$ of PMMA latex particles dispersed in KCl aqueous solutions at various concentrations: (a) 20, (b) 25, (c) 30, (d) 40, (e) 50, (f) 60, (g) 70, (h) 100, and (i) 500 mM. Initiator: V-50.

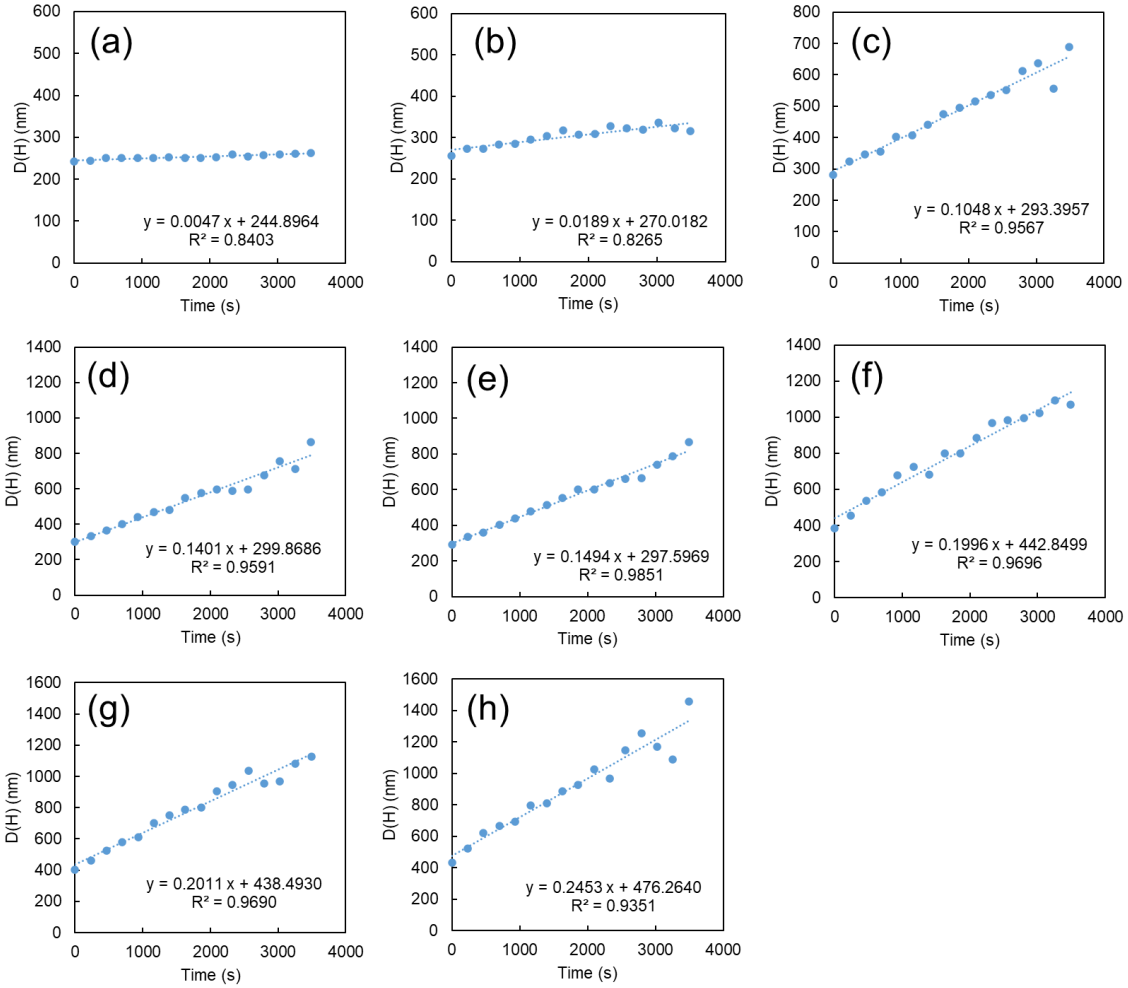

Fig. 3-7. Time course of $D(H)$ of PMMA latex particles dispersed in KCH_3SO_3 aqueous solutions at various concentrations: (a) 15, (b) 18, (c) 20, (d) 25, (e) 30, (f) 50, (g) 70, and (h) 100 mM. Initiator: V-50.

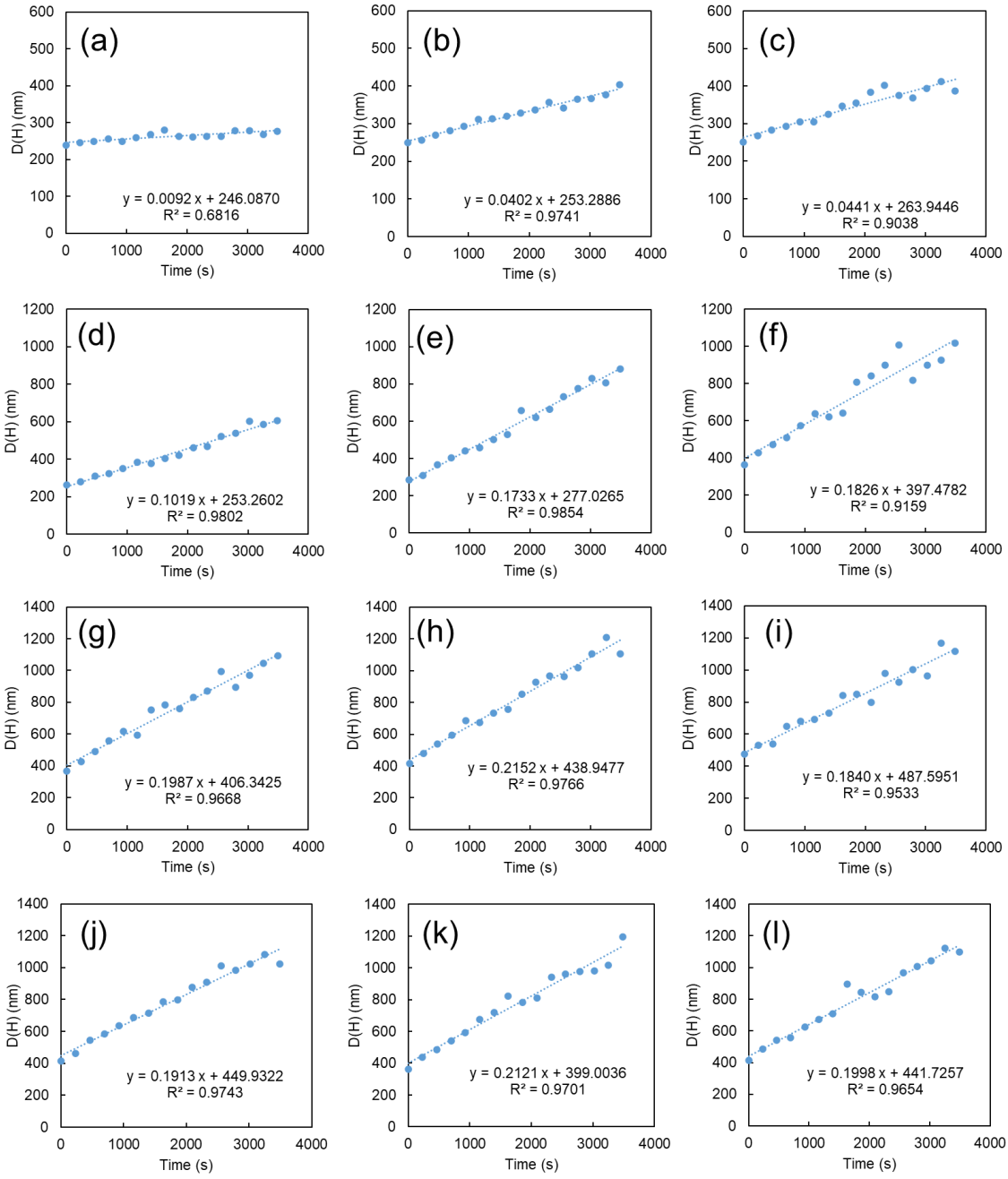

Fig. 3-8. Time course of $D(H)$ of PMMA latex particles dispersed in KCF_3SO_3 aqueous solutions at various concentrations: (a) 2.5, (b) 3, (c) 3.2, (d) 3.5, (e) 4, (f) 5, (g) 6, (h) 7, (i) 8, (j) 9, (k) 10, and (l) 20 mM. Initiator: V-50.

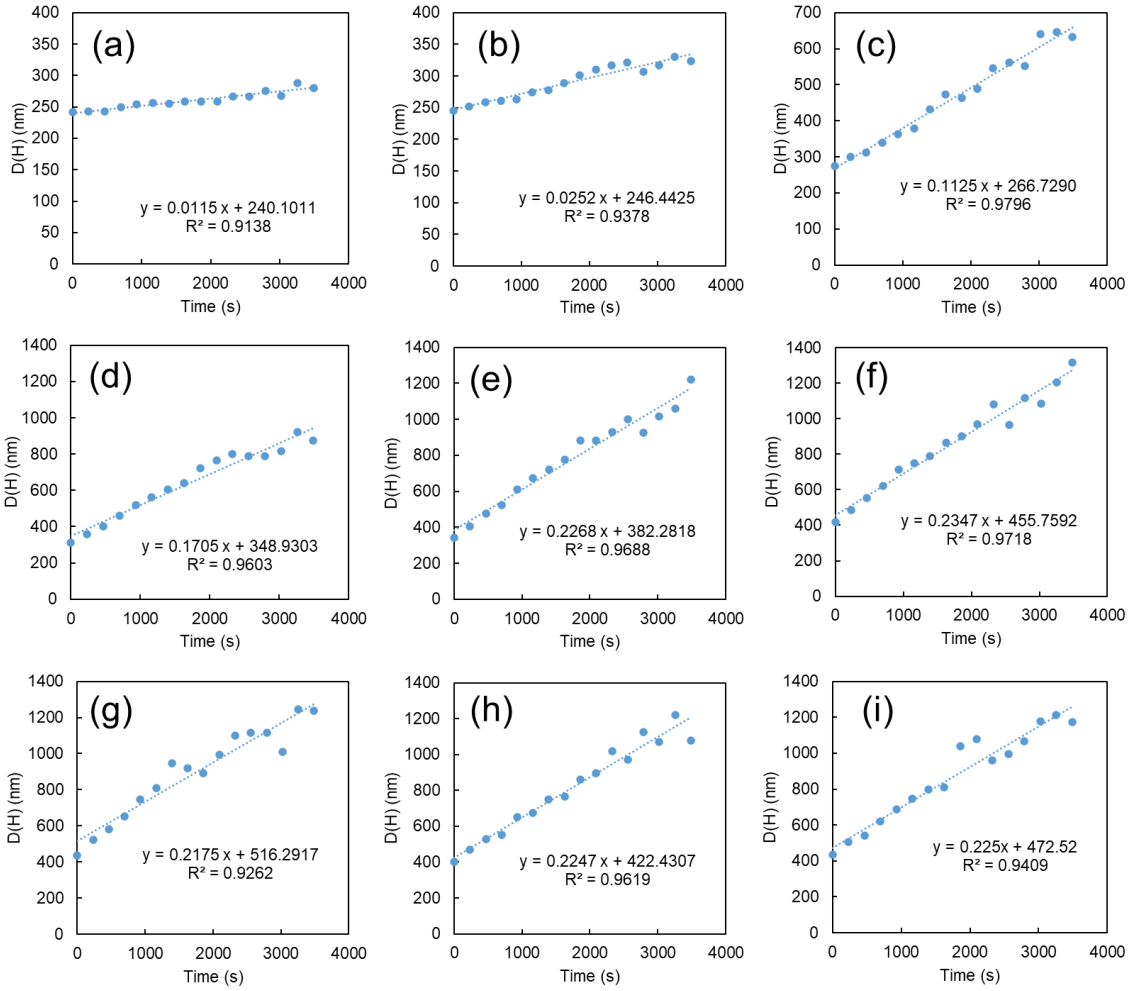

Fig. 3-9. Time course of $D(H)$ of PMMA latex particles dispersed in KCl aqueous solutions at various concentrations: (a) 18, (b) 20, (c) 25, (d) 30, (e) 40, (f) 50, (g) 70, (h) 100, and (i) 500 mM. Initiator: VA-044.

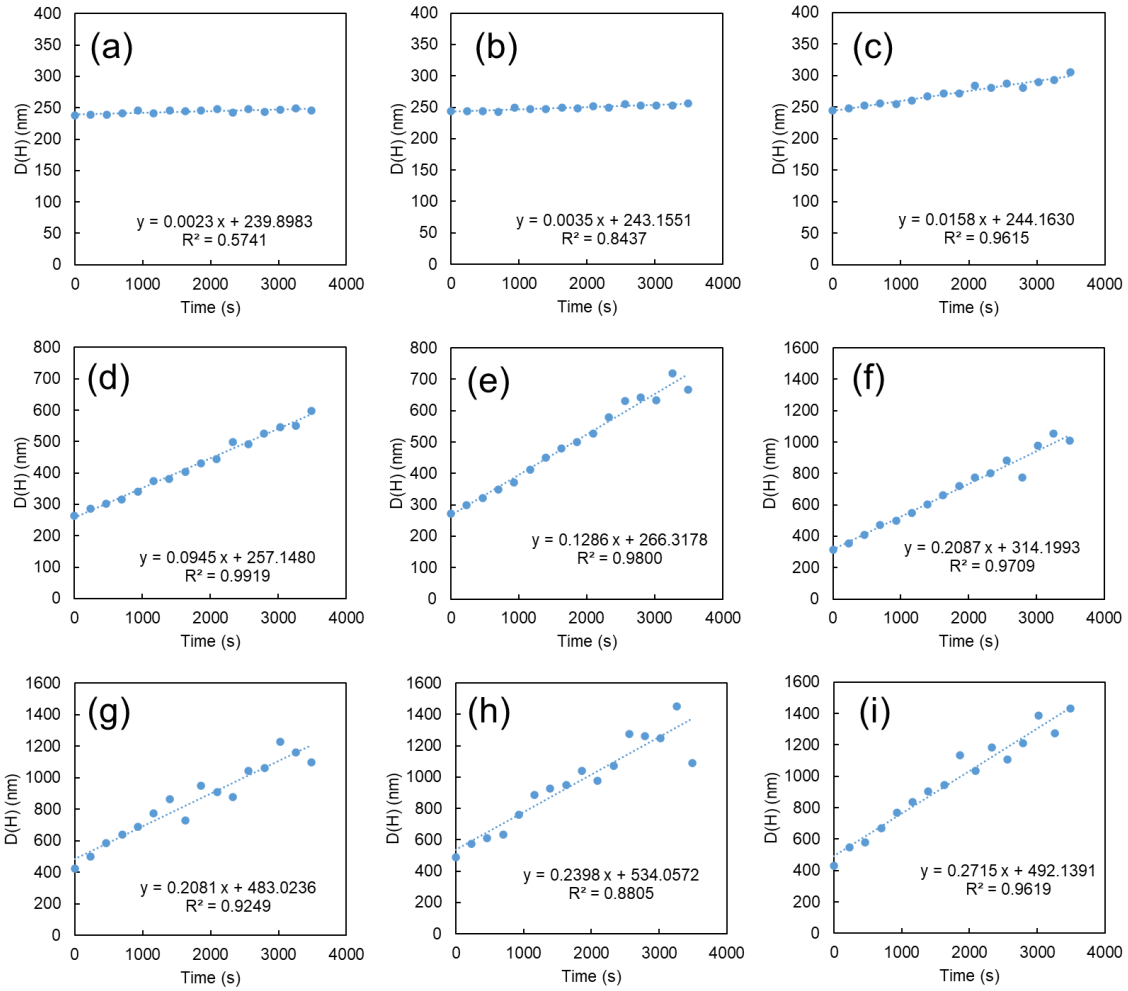

Fig. 3-10. Time course of $D(H)$ of PMMA latex particles dispersed in KCH_3SO_3 aqueous solutions at various concentrations: (a) 11, (b) 14, (c) 18, (d) 20, (e) 25, (f) 30, (g) 50, (h) 70, and (i) 100 mM. Initiator: VA-044.

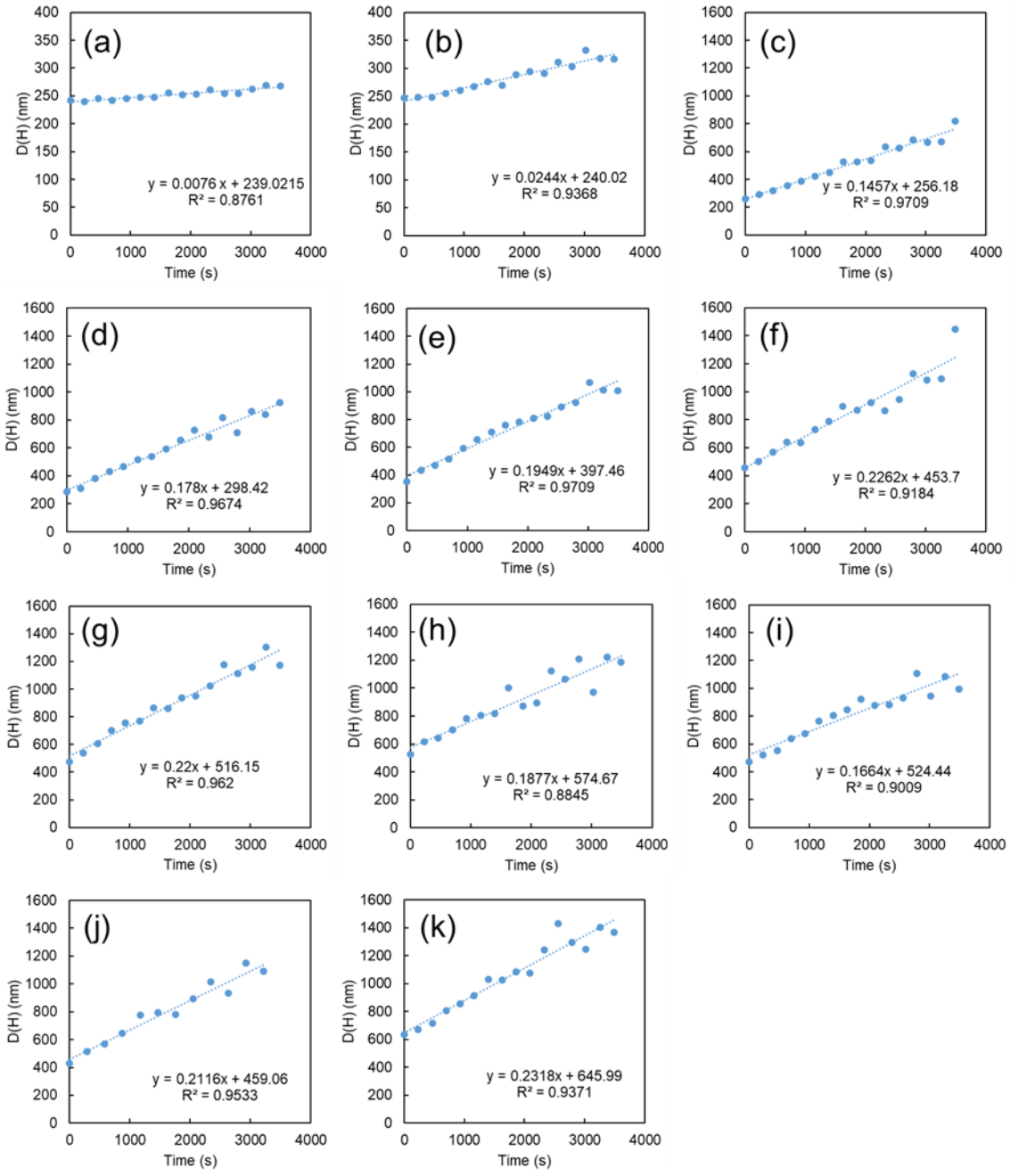

Fig. 3-11. Time course of $D(H)$ of PMMA latex particles dispersed in KCF_3SO_3 aqueous solutions at various concentrations: (a) 3, (b) 3.2, (c) 3.5, (d) 4, (e) 5, (f) 6, (g) 7, (h) 8, (i) 9, (j) 10, and (k) 20 mM. Initiator: VA-044.

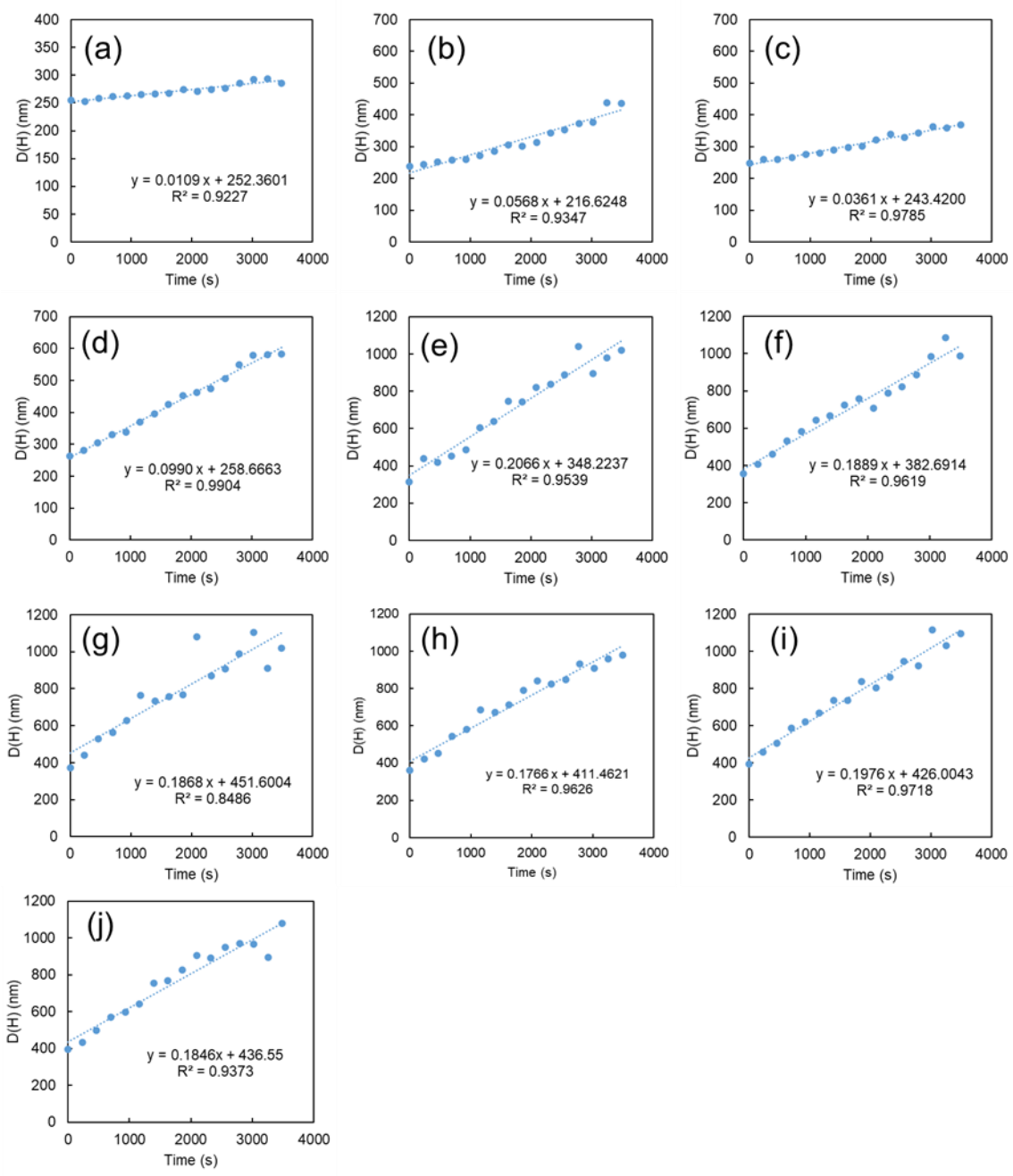

Fig. 3-12. Time course of $D(H)$ of PMMA latex particles dispersed in KCl aqueous solutions at various concentrations: (a) 16, (b) 18, (c) 20, (d) 25, (e) 30, (f) 40, (g) 50, (h) 70, (i) 100, and (j) 500 mM. Initiator: ADIP-Cl.

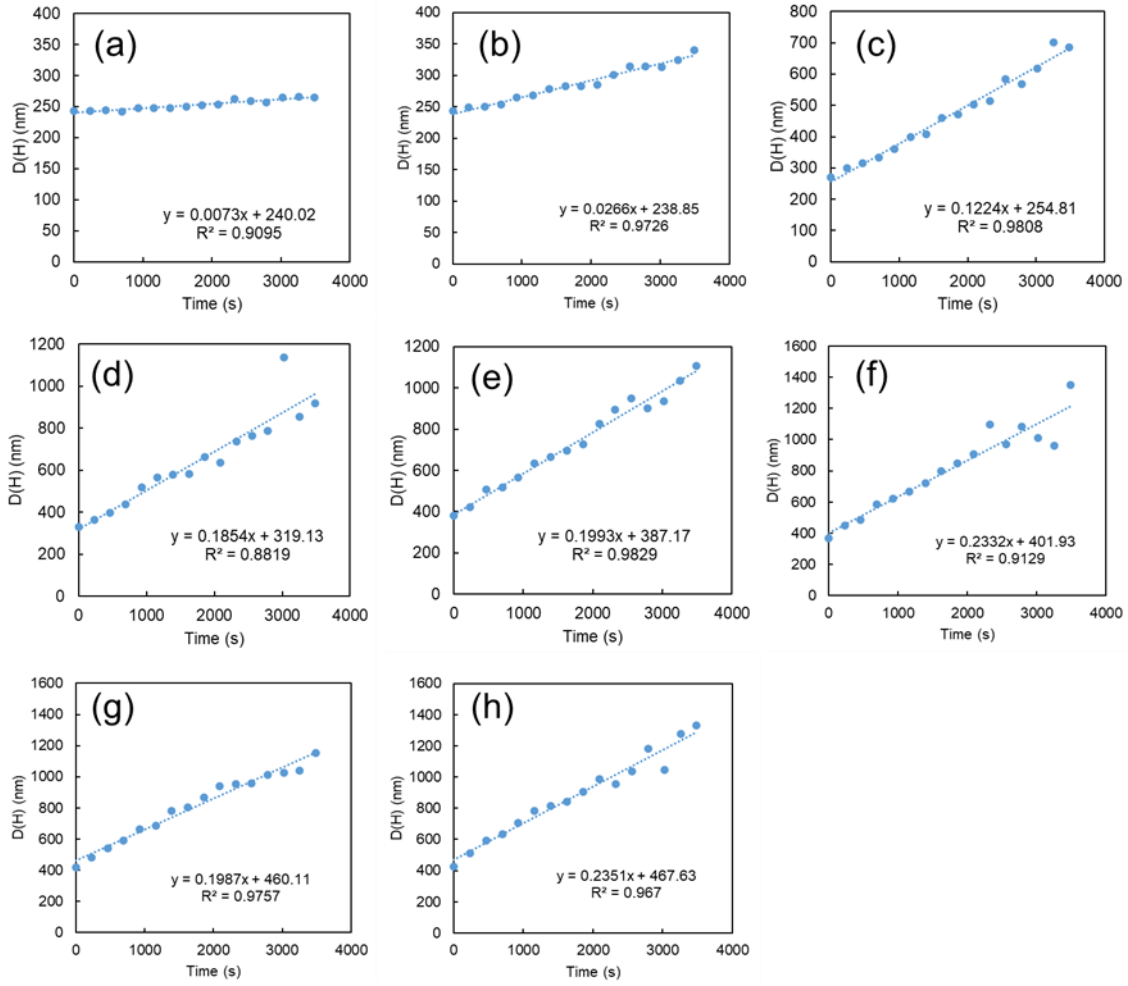

Fig. 3-13. Time course of $D(H)$ of PMMA latex particles dispersed in KCH_3SO_3 aqueous solutions at various concentrations: (a) 17, (b) 20, (c) 25, (d) 30, (e) 40, (f) 50, (g) 70, and (h) 100 mM. Initiator: ADIP-Cl.

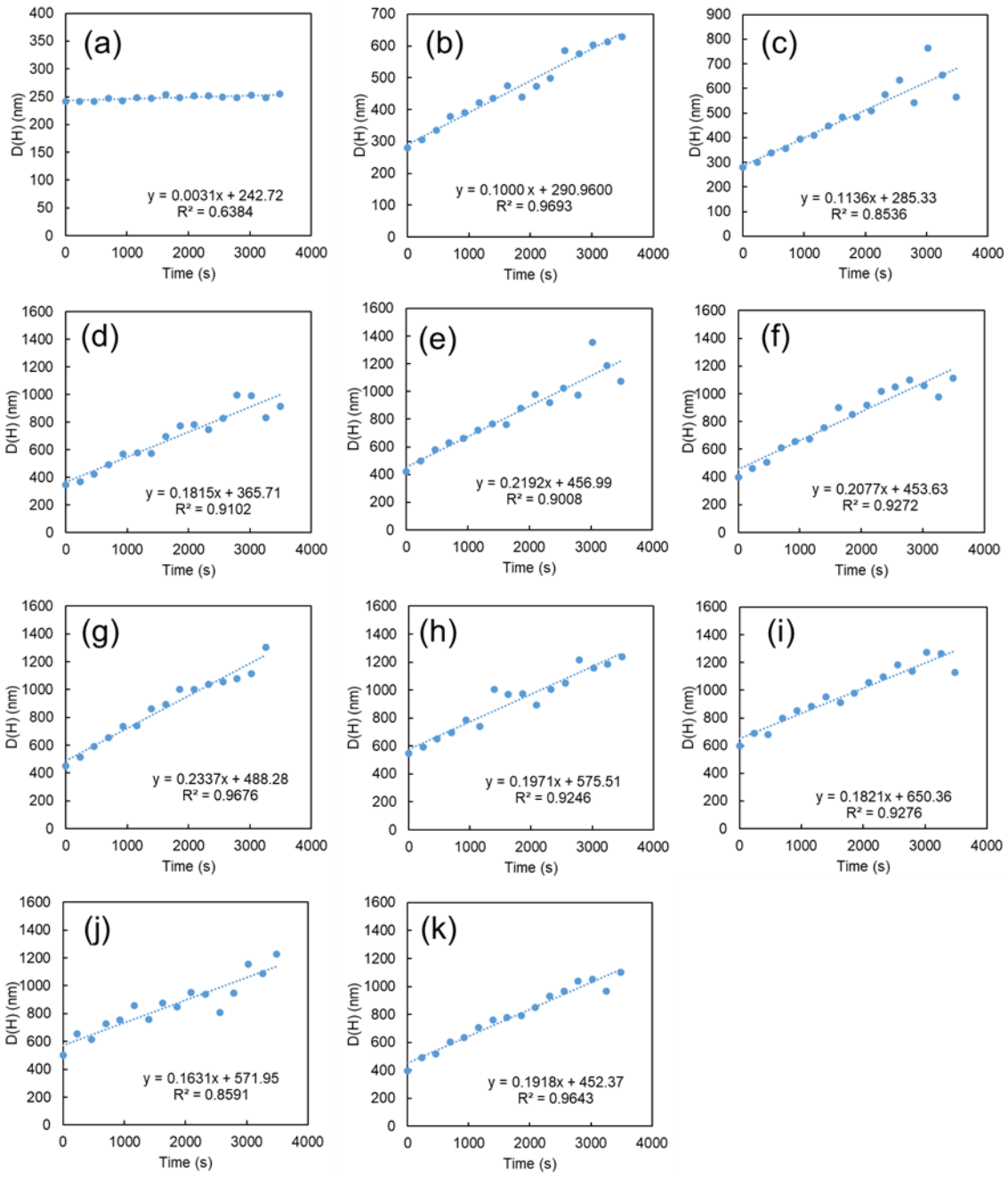

Fig. 3-14. Time course of $D(H)$ of PMMA latex particles dispersed in KCF_3SO_3 aqueous solutions at various concentrations: (a) 2, (b) 3, (c) 3.5, (d) 4, (e) 5, (f) 6, (g) 7, (h) 8, (i) 9, (j) 10, and (k) 20 mM. Initiator: ADIP-Cl.

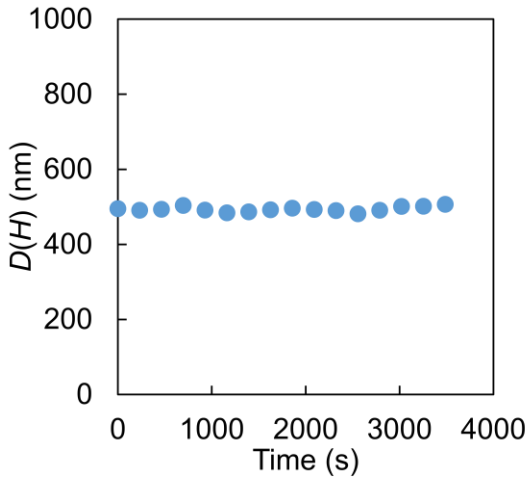

Fig. 3-15. Time course of $D(H)$ of sulfate-PMMA latex particles dispersed in 10 mM KCF_3SO_3 aqueous solution.

3.3.4 Stability Ratio of Cationic PMMA Latex Particles

Stability ratio W is plotted against the electrolyte concentration in Fig. 3-16. All cationic latex particles exhibited similar qualitative trends. For all monovalent anion species, W decreased as the electrolyte concentration increased, reaching unity above the critical coagulation concentration (CCC).

CCC is the minimum electrolyte concentration required to eliminate the repulsive barrier derived from the electrostatic double layer around the latex particles. It is predicted by the DLVO theory, according to which the inter-particle potential energy can be expressed as the sum of the electrostatic repulsive force and vdW attractive force ($V_T = V_{EDL} + V_{vdW}$). In the regime of slow aggregation, which occurs below the CCC, the electrostatic repulsive force is stronger than the vdW attractive force that is always present between approaching particles. This case is indicated by $W > 1$ in Eqs. (3.8) and (3.9). Conversely, above the CCC the repulsive force becomes much weaker, and the particle aggregation rate is dominated by the vdW attractive force and the frequency of diffusional collision of particles. This state is called the fast-aggregation regime, where W always has a value of 1 [10-14]. Here, I observed both the slow- and fast-aggregation regimes separated by the CCC.

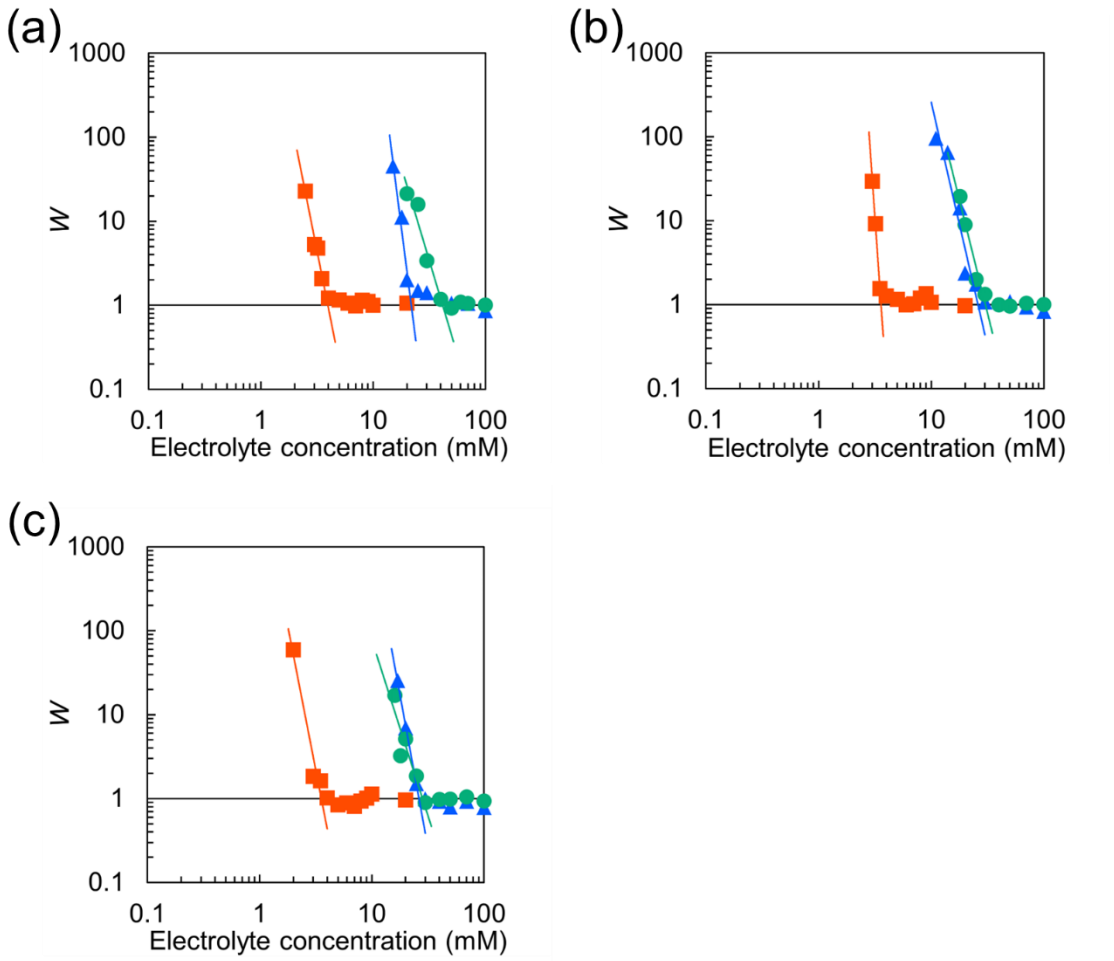

Fig. 3-16. Stability ratio of cationic PMMA latex particles dispersed in different electrolytes. (a) Amidine-, (b) imidazoline-, and (c) imidazolium-PMMA latex particles. KCl (green circles), KCH_3SO_3 (blue triangles), and KCF_3SO_3 (red squares).

3.3.5 Determination of CCC

Table 3-3 presents the CCC values of the cationic PMMA latex particles, which are determined by the intersection of the regression lines in the slow- and fast-aggregation regimes ($W = 1$) (Fig. 3-16). For all types of particles, the CCC value of KCF_3SO_3 was 4 mM, which was far lower than those of KCl and KCH_3SO_3.

Table 3-3. Experimentally determined CCC values of cationic PMMA latex particles.

Moieties	KCl (mM)	KCH_3SO_3 (mM)	KCF_3SO_3 (mM)
Amidine	42	22	4
Imidazoline	30	26	4
Imidazolium	28	26	4

3.3.6 Electrolyte Adsorption onto the Hydrophobic Interface

Figure 3-17 shows the surface tension $\Delta\gamma$ as a function of aqueous electrolyte concentration. In the case of KCl, $\Delta\gamma$ increased with the electrolyte concentration, suggesting that these ions are repelled from the hydrophobic interface. The tendency of increased surface tension agrees with a previous study [15]. In the case of KCH_3SO_3, $\Delta\gamma$ did not vary but rather remained at almost zero, indicating that $CH_3SO_3^-$ is less repelled than Cl^- by the hydrophobic interface. In the case of KCF_3SO_3, a steep decrease of $\Delta\gamma$ was observed, indicating stronger attraction of triflate ion to the hydrophobic surface compared to the other anions.

To gain additional quantitative information about the interface behavior of ions, the coefficient A was calculated from the regression lines in Fig. 3-17, and its values are shown in Table 3-4. I have $A = -0.39$ for KCH_3SO_3, indicating that the surface affinity is close to zero. The A value of KCF_3SO_3 is more than 20 times larger than that of KCF_3SO_3, supporting a stronger affinity of $CF_3SO_3^-$ for the hydrophobic air-water interface.

The air-water interface is often used as a simple experimental model to evaluate the surface affinity of ions, because this interface is free from complicities due to dissociable surface groups, unlike the surface of amidine- or imidazoline-PMMA latex particles. The experimental results described above support the hypothesis that in the presence of $CF_3SO_3^-$ hydrophobic interaction is a major force driving the aggregation of cationic PMMA latex particles. Specifically, hydrophobic adsorption of $CF_3SO_3^-$ onto the cationic PMMA particles efficiently lowers the

surface charge of these particles. The resultant weaker electrostatic force leads to particle aggregation.

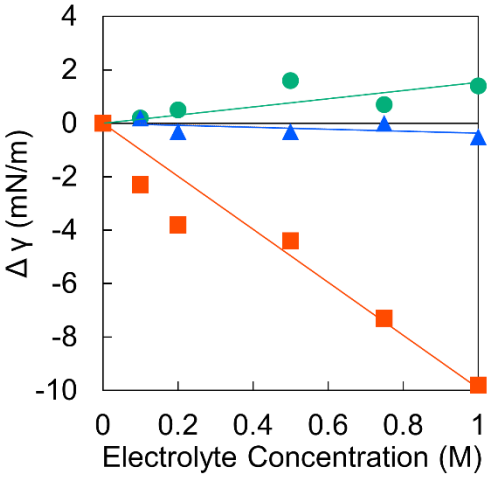

Fig. 3-17. Surface tension of electrolyte solutions. KCl (green circles), KCH_3SO_3 (blue triangles), and KCF_3SO_3 (red squares). Colored lines are regression lines.

Table 3-4. Experimentally determined *A* coefficient of electrolyte solutions.

Electrolytes	*A* (mN/m)/(mol/L)
KCl	1.3
KCH_3SO_3	-0.39
KCF_3SO_3	-8.6

3.4 Discussion

The zeta potential of cationic PMMA latex particles decreased to almost 0 mV in the presence of KCF_3SO_3. Moreover, triflate strongly adsorbed onto the hydrophobic interface. Based on these results, I conclude that triflate adsorbed onto the PMMA surface *via* hydrophobic interaction of the trifluoromethyl group. In contrast, the methyl group of $CH_3SO_3^-$ did not sufficiently adsorb onto the PMMA surface. The decrease of zeta potential would be caused by neutralization of the cationic PMMA surface due to the strong adsorption of anions, which allowed the attractive vdW force to surpass the electrostatic repulsive force between particles. The monovalent anions thiocyanate (SCN^-), perchlorate (ClO_4^-), and tetraphenyl borate (Ph_4B^-) were reported to induce aggregation at a lower concentration [13, 14], and all these anions show incredibly low hydration numbers. Similarly, the trifluoromethyl group of triflate is hardly hydrated in aqueous solutions [16]. In conclusion, the hydrophobicity of triflate is a likely cause of the aggregation of cationic PMMA latex particles.

Additional studies are needed to determine the extent to which these effects occur for other types of polymeric latex particles, especially PS, because several researchers found that other anions caused aggregation of PS latex particles *via* non-DLVO forces [13, 14]. Nevertheless, cationic latex particles of PS and PMMA presumably differ in their aggregation kinetics. Yamamoto *et al*. reported that PS particles prepared using an oil-soluble azo radical initiator showed negative charge because of π-electron cloud derived from the aromatic structure of styrene [17-19]. Although the adsorption of triflate onto the cationic PS latex particle surface is driven by the hydrophobicity of triflate, when triflate is located very close to the surface, repulsive force from π-electrons should be considered. As a result, I expect the CCC of cationic PS latex particles in the presence of triflate is higher than that of cationic PMMA latex particles.

3.5 Summary

Chapter 3 demonstrates the aggregation mechanism of cationic PMMA latex particles in the presence of triflate anion. The zeta potential of these particles significantly decreased in the presence of KCF_3SO_3. Compared to other monovalent ions, triflate caused aggregation of cationic PMMA latex particles at a lower concentration. The strong adsorption of triflate *via* its trifluoromethyl group onto the PMMA surface would contribute to surface charge neutralization. This finding would facilitate the control of dispersion/aggregation behavior of cationic latex particles.

3.6 References

[1]. Suga, K., Murakami, M., Nakayama, S., Watanabe, K., Yamada, S., Tsuji, T., & Nagao, D. (2022). Surface characteristics of antibacterial polystyrene nanoparticles synthesized using cationic initiator and comonomers. *ACS Appl. Bio Mater*., 5(5), 2202-2211.

[2]. Kretzschmar, R., Holthoff, H., & Sticher, H. (1998). Influence of pH and humic acid on coagulation kinetics of kaolinite: A dynamic light scattering study. *J. Colloid Interface Sci*., 202(1), 95-103.

[3]. Weissenborn, P. K., & Pugh, R. J. (1996). Surface tension of aqueous solutions of electrolytes: relationship with ion hydration, oxygen solubility, and bubble coalescence. *J. Colloid Interface Sci*., 184(2), 550-563.

[4]. Pegram, L. M., & Record, M. T. (2007). Hofmeister salt effects on surface tension arise from partitioning of anions and cations between bulk water and the air-water interface. *J. Phys. Chem. B*, 111(19), 5411-5417.

[5]. Brandon, N. P., Kelsall, G. H., Levine, S., & Smith, A. L. (1985). Interfacial electrical properties of electrogenerated bubbles. *J. Appl. Electrochem.*, 15, 485-493.

[6]. Graciaa, A., Morel, G., Saulner, P., Lachaise, J., & Schechter, R. S. (1995). The Zeta potential of gas bubbles. *J. Colloid Interface Sci*., 172(1), 131-136.

[7]. Zimmermann, R., Dukhin, S., & Werner, C. (2001). Electrokinetic measurements reveal interfacial charge at polymer films caused by simple electrolyte ions. *J. Phys. Chem. B*, 105(36), 8544-8549.

[8]. Roger, K., & Cabane, B. (2012). Why are hydrophobic/water interfaces negatively charged? *Angew. Chem. Int. Ed*., 51(23), 5625.

[9]. Berry, J. D., Neeson, M. J., Dagastine, R. R., Chan, D. Y., & Tabor, R. F. (2015). Measurement of surface and interfacial tension using pendant drop tensiometry. *J. Colloid Interface Sci*., 454, 226-237.

[10]. Sugimoto, T., Cao, T., Szilagyi, I., Borkovec, M., & Trefalt, G. (2018). Aggregation and charging of sulfate and amidine latex particles in the presence of oxyanions. *J. Colloid Interface Sci*., 524, 456-464.

[11]. Holthoff, H., Egelhaaf, S. U., Borkovec, M., Schurtenberger, P., & Sticher, H. (1996). Coagulation rate measurements of colloidal particles by simultaneous static and dynamic light scattering. *Langmuir*, 12(23), 5541-5549.

[12]. Behrens, S. H., Christl, D. I., Emmerzael, R., Schurtenberger, P., & Borkovec, M. (2000). Charging and aggregation properties of carboxyl latex particles: Experiments versus DLVO theory. *Langmuir*, 16(6), 2566-2575.

[13]. Cao, T., Trefalt, G., & Borkovec, M. (2018). Aggregation of colloidal particles in the presence of hydrophobic anions: Importance of attractive non-DLVO forces. *Langmuir*, 34(47), 14368-14377.

[14]. Calero, C., Faraudo, J., & Bastos-Gonzalez, D. (2011). Interaction of monovalent ions with hydrophobic and hydrophilic colloids: charge inversion and ionic specificity. *J. Am. Chem. Soc*., 133(38), 15025-15035.

[15]. Uematsu, Y., Bonthuis, D. J., & Netz, R. R. (2019). Impurity effects at hydrophobic surfaces. *Curr. Opin. Electrochem.*, 13, 166-173.

[16]. Bergström, P. Å., & Lindgren, J. (1990). An infrared spectroscopic study of the hydration of the triflate ion ($CF3SO^{-}_{3}$) in aqueous solution. *J. Mol. Struct.*, 239, 103-111.

[17]. Yamamoto, T. (2012). Soap-free emulsion polymerization of aromatic vinyl monomer using AIBN. *Colloid. Polym. Sci*., 290, 1833-1835.

[18]. Yamamoto, T. (2013). Synthesis of nearly micron-sized particles by soap-free emulsion polymerization of methacrylic monomer using an oil-soluble initiator. *Colloid. Polym. Sci*., 291, 2741-2744.

[19]. Yamamoto, T., & Kawaguchi, K. (2016). Relationship between surface potential and particle size in soap-free emulsion copolymerization of styrene and methyl methacrylate using a water-or oil-soluble initiator. *Colloid. Polym. Sci*., 294, 281-284.

Chapter 4 Functionalization of Cationic PMMA Particles

4.1 Introduction

This chapter focuses on functionalization of cationic PMMA particles prepared using ADIP-Cl. Considering the many industrial uses of PEs, cationic particles are expected to be more suitable for PE formation because the oil-water interface carries negative charge and tends to attract positively charged particles for adsorption through electrostatic force. However, phase separation occurs soon after agitating a mixture of oil and aqueous dispersion of cationic PMMA particles, resulting in emulsion failure. One way to suppress this is to modify the surface of particles to enhance their adsorption onto the droplet interface, as described in Section 1.4.3. Here, I focused on particle modification using PVA, which is a water-soluble polymer with excellent biocompatibility and chemical properties and has been used in a wide variety of industries. In previous studies, poly(lactic-co-glycolic acid) (PLGA) nanoparticles prepared from PVA *via* emulsion-evaporation methods were used in O/W PE [1, 2], and the PVA layer on the particle surface was able to change the wettability with amphiphilicity. As a result, water-dispersed PLGA-PVA particles adsorbed at the oil-water interface to form an O/W PE. However, it remains unclear why water-soluble PVA forms an adsorbed layer on polymeric particles in the continuous water phase, or how such a layer changes the wettability of the particle surface. Thus, I prepared PVA-modified cationic PMMA particles (denoted as PMMA-PVA) using PVA at three levels of hydrolysis for successful PE preparation. Furthermore, the behavior of PVA adsorbed onto the PMMA surface in water was investigated using coarse-grained simulations at the molecular level.

4.2 Materials & Methods

4.2.1 Reagents

Water treated by reverse osmosis and electrodeionization was used in all the experiments. Chloroform (purity 99.0%), methyl methacrylate (MMA, purity 98.0%), poly(vinyl alcohol) (PVA, catalog no. 165-16315; degree of polymerization 500; degree of saponification > 96 mol%; values as specified by the manufacturer), sodium chloride (NaCl, purity 99.5%), and 1,1,1,3,3,3-hexafluoroisopropanol (HFIP, purity 99.5%) were obtained from Fujifilm Wako Pure Chemical Corporation (Japan). Decamethylcyclopentasiloxane (DMCPS, purity 100%) was procured from Shin-Etsu Chemical Co., Ltd. (Japan). An inhibitor remover (catalog no. 311340) and 3-(2-benzothiazolyl)-*N*,*N*-diethylumbelliferylamine (coumarin-6, purity 98%) were obtained from Sigma-Aldrich Corporation (USA). *N*,*N*-Dimethylacetamide (purity > 99.0%) and sodium

trifluoroacetate (purity > 98.0%) were procured from Tokyo Chemical Industry Corporation (Japan). Two other PVA specimens (JL-05E and JP-05; degree of polymerization, 500 and 500; degree of saponification, 80 and 88 mol%; purity, ≥95% and ≥95%, respectively; values as specified by the manufacturer) were supplied by Japan Vam & Poval Co., Ltd. (Japan). ADIP-Cl was synthesized following the procedure described in Chapter 2.

The dynamic viscosities of aqueous PVA solutions were measured at 20 ℃ using a viscometer (ViscoQC 300-L; Anton Paar, Austria) equipped with a PTD 80 temperature sensor and an SC4-18 spindle. The degrees of saponification of PVA specimens were estimated by titration according to the Japanese Industrial Standard for testing PVA (JIS K6726). The obtained results are listed in Table 4-1.

Table 4-1. Characteristics of PVA specimens. The error represents the standard deviation of three independent measurements.

PVA Cat. No.	Degree of polymerization	Saponification (mol%)	Viscosity[a] (mPa·s)	IT[b] (mN/m)
JL-05E	500	80	4.58	14.4±0.7
JP-05	500	88	5.70	11.0±0.2
165-16315	500	>96	7.98	23.3±0.2

[a] 4% aqueous solution, [b]1% aqueous solution suspended in DMCPS.

4.2.2 Particle Synthesis and Evaluation

PMMA particles

PMMA latex particles were prepared following the procedure described in Section 2.2.3. Briefly, ADIP-Cl (23 mg) dissolved in water (1 g) and the MMA monomer (4.5 g) were added to water (24.5 g), followed by polymerization at 60 ℃ for 16 h. To prepare fluorescent-labeled PMMA particles, coumarin-6 (1.58 mg) was dissolved in the MMA monomer prior to polymerization. All emulsions obtained by polymerization were cooled to 25 ℃ and characterized.

PMMA-PVA particles

The synthesis of PMMA-PVA particles was entirely conducted in a 300-mL reactor (inner diameter: 75 mm) equipped with a baffle board and a three-necked lid. The PMMA particle dispersion and an aqueous PVA solution (total solid contents of PMMA and PVA are 4.8 and 2.7

g, respectively) were added into the reactor, followed by adding water to achieve a total weight of 199 g. Subsequently, the temperature was increased, and the radical initiator ADIP-Cl (38 mg) dissolved in water (1 g) was added to the warm emulsion for monomer elimination. The reaction was conducted at 60 ℃ under mechanical stirring for 3 h using a sealing mixer (UZ-SM1, Nakamura Scientific Instruments Industry Co., Ltd., Japan) and a propeller-shaped stirring rod (ø8 × 300 mm). The particle dispersion was cooled to 25 ℃ and characterized.

Prior to characterizing PMMA-PVA, free PVA was removed by washing as follows. The PMMA-PVA dispersion (200 g) was centrifuged at 12,000 *g* for 60 min, and the supernatant was removed. The precipitate was added with water (200 g) and then homogeneously dispersed. The washing process was repeated thrice. Subsequently, a 10 wt% PMMA-PVA stock dispersion and a freeze-dried powder (<10 Pa, 2 days) were prepared for the experiments described in sections 2.5.5, 2.5.6, and 2.5.7. The density of 0.01–1 wt% PMMA-PVA dispersions was determined to be 1.00 g/mL using a 20-mL Hubbard-type pycnometer.

Dynamic light scattering

DLS measurements were performed following the procedure described in Section 2.2.2. The sample at a concentration of 10 mg/L was prepared using the stock dispersion. The aggregation resistance against electrolytes containing NaCl is important for the stability of particle dispersion, and it can be used to evaluate the steric repulsion of the particles. Briefly, the polymer dispersion was diluted with an aqueous NaCl stock solution at a varying concentration from 0.0001 to 1 mol/L. The thickness of the layer of adsorbed PVA around the PMMA particles {denoted as adsorbed layer thickness (ALT)} was calculated using Eq. (4.1) [3, 4].

$$\mathrm{ALT} = \frac{1}{2}\left(D(H)_{PMMA-PVA} - D(H)_{PMMA}\right) \tag{4.1}$$

Zeta potential

The zeta potential was measured following the procedure described in Section 3.2.2.

Scanning electron microscopy

SEM was conducted following the procedure described in Section 2.2.2. The average diameters of synthesized polymer particles were calculated based on 10 particles in the SEM images.

4.2.3 Emulsion Preparation

An NS-310E3 homogenizer with an NS-7A mixing head (Micro-Tec Co., Ltd., Japan) was used for stirring during emulsification at 10 g. The oil phase (DMCPS), water, and the PMMA-PVA dispersed phase (with or without coumarin-6 label) were placed in 10-mL glass vials (height, 45

mm; inner diameter, 24 mm). DMCPS is a representative silicone oil used in the cosmetics industry. The mixture was homogenously stirred at 5,000 rpm (dial position 2) for 2 min. The volume fraction of dispersed DMCPS (ϕ_D) was estimated as the ratio of the oil volume relative to the total liquid volume. Emulsions with ϕ_D varying from 0.11 to 0.83 were prepared.

4.2.4 Observation of Emulsions

Macroscopic analysis

The appearance of the emulsions was monitored after storage for 0, 14, 15, and 86 days at 25 ℃.

Microscopic examination

The emulsion droplets were observed under an optical microscope (Leica DM2000 LED, Leica Microsystems, Germany) equipped with a camera (Leica DMC 2900), employing the image processing software Leica Application Suite (version 4.12.0, Germany). Approximately one drop of the prepared emulsion was spread on a glass slide for these experiments.

Confocal laser scanning microscopy

Fluorescence was monitored using a confocal laser scanning microscope (CLSM, LSM980, ZEISS, Germany) equipped with a Plan Apochromat 63× oil immersion objective and a 1.4 numerical aperture at an excitation wavelength of 473 nm and fluorescence wavelengths of 485–585 nm. The prepared emulsion (~100 μL) was placed in a film bottom dish (ibid GmbH, Germany). Confocal imaging was performed at a distance of 10 μm from the bottom of the dish to eliminate significant wall effects.

4.2.5 Extraction of Insoluble Fraction

The chloroform-insoluble fraction of PMMA-PVA was obtained using a Soxhlet extractor. The extraction kit consisted of a 150-mL flat-floor flask (SIBATA Scientific Technology Holdings Limited, Japan), a bead bath (BBH K-100, AS ONE CORPORATION, Japan), and a cylindrical cellulose cylinder (28 mm × 1000 mm). Chloroform (120 mL) and the freeze-dried sample (>1.5 g) were placed in the flat-floor flask and cylinder, respectively. The temperature of the bead bath was set to 100 ℃, and extraction was performed for more than 16 h. Afterwards, the cylinder with the chloroform-insoluble fraction was dried for more than 12 h at a pressure of <10 Pa, using a VOM-1000 vacuum dryer equipped with a UT-2000 tabletop cooling trap (TOKYO RIKAKIKAI CO., LTD. Japan). The chloroform-insoluble fraction did not dissolve in hot water or dimethyl sulfoxide but was dissolved in *N,N*-dimethylacetamide and HFIP.

The ratio of the chloroform-insoluble fraction to the input material (insoluble fraction) was calculated using Eq. (4.2).

$$\text{Insoluble fraction } \% = \frac{\text{Mass of chloroform} - \text{insolube fraction}}{\text{Mass of freeze dried sample}} \times 100 \qquad (4.2)$$

4.2.6 Fourier-Transform Infrared Spectroscopy

Chemical structures of the specimens were investigated using a Fourier-transform infrared (FTIR) device (Nicolet iS50, Thermo Fisher Scientific, USA) equipped with an attenuated total reflectance instrument having a diamond crystal plate as a reflector and a deuterated triglycine sulfate detector with a resolution of 4 cm^{-1}. A total of 32 scans were performed using the potassium bromide method. Data were collected and analyzed using OMNIC version 9.13 (Thermo Fisher Scientific, USA).

4.2.7 Gel Permeation Chromatography

The number-average molecular weight (M_n) and weight-average molecular weight (M_w) of the chloroform-insoluble fractions of PMMA, PVA, and PMMA-PVA were determined *via* gel permeation chromatography (GPC). This analysis was conducted at 40 ℃ using a Shodex GPC-104-series high-speed liquid chromatography instrument (Shoko Co., Ltd., Japan) equipped with a guard column (Shodex GPC K-G 4A, Showa Denko K.K., Japan) and two serial columns (Shodex GPC LF-404). Calibration curves were obtained using PMMA. HFIP containing 10 mM sodium trifluoroacetate was used as the eluent at a flow rate of 0.3 mL min^{-1}. Each freeze-dried sample (2 mg) was dissolved in the eluent (1 mL) and passed through a polytetrafluoroethylene (PTFE) membrane filter with a pore size of 0.2 μm. Then, 10 μL of the filtered sample solution was injected. Data were collected and analyzed using SIC μ7 version 1.00 (SYSTEM INSTRUMENTS Co., Ltd., Japan). PDI was calculated from the obtained data as M_w/M_n.

4.2.8 Interfacial Tension

Dynamic interfacial tension (IT) was measured *via* pendant drop tensiometry using a contact angle meter (DMo-502; Kyowa Interface Science Co., Ltd., Japan). A blunt-tipped needle with an outer diameter of 0.7 mm was used to add a droplet of the aqueous PVA solution, PMMA dispersion, or PMMA-PVA dispersion suspended in DMCPS. The measurements were conducted at 26 ± 1 ℃ and 45 ± 5% humidity. The experimentally acquired images of droplets were processed using the Young-Laplace equation in FAMAS software (version 7.2.0; Kyowa Interface Science Co., Ltd., Japan). For the calculations, the densities of DMCPS, PVA solution, and PMMA and PMMA-PVA dispersions were set to 0.96, 1.00, and 1.00 g/mL, respectively (see Table 1 for the IT values of the 1 wt% aqueous PVA solutions). The IT values obtained 1500 s after starting the measurement were used.

4.2.9 Simulation Methods

Dissipative particle dynamics

The dissipative particle dynamics (DPD) method [5, 6] was employed to investigate how the PVA saponification degree affects its adsorption onto PMMA at the molecular level. In DPD, a group of atoms or molecules are lumped together as a DPD bead, allowing the simulations to be performed on *millisecond* time scales and *micrometer* length scales. As a remarkably promising mesoscopic simulation tool, DPD has been applied to diverse biphasic systems with surfactants [7-9] and polymeric systems [10-12]. The DPD method is fundamentally governed by Newton's equation of motion, with each DPD bead subjected to three types of intermolecular forces: conservative, dissipative, and random. The Newton's equation of motion for particle *i* can be expressed as follows:

$$m_i \frac{d\mathbf{v}_i}{dt} = \mathbf{f}_i = \sum_{j \neq i} \mathbf{F}_{ij}^{\mathrm{C}} + \sum_{j \neq i} \mathbf{F}_{ij}^{\mathrm{D}} + \sum_{j \neq i} \mathbf{F}_{ij}^{\mathrm{R}}, \tag{4.3}$$

where m is the mass, $\mathbf{v}$ is the velocity, $\mathbf{F}^{\mathrm{C}}$ is the conservative force, $\mathbf{F}^{\mathrm{D}}$ is the dissipative force, and $\mathbf{F}^{\mathrm{R}}$ is the pairwise random force. The sum of forces acting on all beads between particles *i* and *j* is calculated. The conservative force, which is softly repulsive, is expressed as

$$\mathbf{F}_{ij}^{\mathrm{C}} = \begin{cases} -a_{ij}\left(1 - \dfrac{|\mathbf{r}_{ij}|}{r_{\mathrm{c}}}\right)\mathbf{n}_{ij}, & |\mathbf{r}_{ij}| \leq r_{\mathrm{c}} \\ 0, & |\mathbf{r}_{ij}| > r_{\mathrm{c}} \end{cases}, \tag{4.4}$$

where $\mathbf{r}_{ij} = \mathbf{r}_j - \mathbf{r}_i$, $\mathbf{n}_{ij} = \mathbf{r}_{ij} / |\mathbf{r}_{ij}|$, a_{ij} represents the magnitude of the repulsive force between beads *i* and *j*, and r_{c} is the cutoff distance. The dissipative force $\mathbf{F}_{ij}^{\mathrm{D}}$ and random force $\mathbf{F}_{ij}^{\mathrm{R}}$ can be expressed as follows:

$$\mathbf{F}_{ij}^{\mathrm{D}} = \begin{cases} -\gamma\omega^{\mathrm{D}}(|\mathbf{r}_{ij}|)(\mathbf{n}_{ij} \cdot \mathbf{v}_{ij})\mathbf{n}_{ij}, & |\mathbf{r}_{ij}| \leq r_{\mathrm{c}} \\ 0, & |\mathbf{r}_{ij}| > r_{\mathrm{c}} \end{cases} \tag{4.5}$$

and

$$\mathbf{F}_{ij}^{\mathrm{R}} = \begin{cases} \sigma\omega^{\mathrm{R}}(|\mathbf{r}_{ij}|)\zeta_{ij}\Delta t^{-1/2}\mathbf{n}_{ij}, & |\mathbf{r}_{ij}| \leq r_{\mathrm{c}} \\ 0, & |\mathbf{r}_{ij}| > r_{\mathrm{c}} \end{cases}, \tag{4.6}$$

where $\mathbf{v}_{ij} = \mathbf{v}_j - \mathbf{v}_i$, σ is the noise parameter, γ is the friction parameter, and ζ_{ij} is a random number based on a Gaussian distribution. Moreover, ω^{R} and ω^{D} are r-dependent weight functions expressed as follows:

$$\omega^{\mathrm{D}}(r_{ij}) = \left[\omega^{\mathrm{R}}(r_{ij})\right]^2 = \begin{cases} \left(1 - \dfrac{|\mathbf{r}_{ij}|}{r_{\mathrm{c}}}\right)^2, & |\mathbf{r}_{ij}| \le r_{\mathrm{c}} \\ 0, & |\mathbf{r}_{ij}| > r_{\mathrm{c}} \ . \end{cases} \tag{4.7}$$

The temperature T is controlled by the balance between $\mathbf{F}_{ij}^{\mathrm{D}}$ and $\mathbf{F}_{ij}^{\mathrm{R}}$. Additionally, the values of σ and γ are related to each other by the fluctuation-dissipation theorem, which is expressed as follows:

$$\sigma^2 = 2\gamma k_{\mathrm{B}} T, \tag{4.8}$$

where k_{B} is the Boltzmann constant. Reduced units are often used in DPD simulations: the unit of length is the cutoff distance r_{c}, the unit of mass is the bead mass m, and the unit of energy is $k_{\mathrm{B}}T$. Temperature is expressed in the energy dimension (k_{B}), with a normal temperature considered to be compatible with $1.0\,k_{\mathrm{B}}T$ [13].

Simulation models

The coarse-grained models adopted in this study (Fig. 4-1) were constructed based on previous findings [9]. The model of PVA is comprised three types of beads: a main chain (vinyl group), a hydrophilic side chain (hydroxy group), and a hydrophobic side chain (acetyl group); which are denoted in Fig. 4-1a as M [yellow region], I [blue region], and O [red region], respectively. The chain length (N) of PVA is set to 10. The degree of saponification is defined as $f = a/(a+b)$, where a and b represent the number of hydrophilic and hydrophobic groups, respectively. I considered two cases with f = 0.8 and 1.0. The model of PMMA (Fig. 4-1b) is comprised of n = 20 beads (denoted by P). Furthermore, a water molecule is represented by a single DPD bead (denoted by W) (Fig. 4-1c). Bonding interactions between the nearest-neighbor particles in the PVA and PMMA molecules are captured using the parameter $\mathbf{F}_{ij}^{\mathrm{S}}$.

$$\mathbf{F}_{ij}^{\mathrm{S}} = -k\left(|\mathbf{r}_{ij}| - r_{\mathrm{s}}\right)\mathbf{n}_{ij}, \tag{4.9}$$

where $k = 100\,k_{\mathrm{B}}T/r_{\mathrm{c}}^2$ is the spring constant and $r_{\mathrm{s}} = 0.5\,r_{\mathrm{c}}$ is the equilibrium bond length [7].

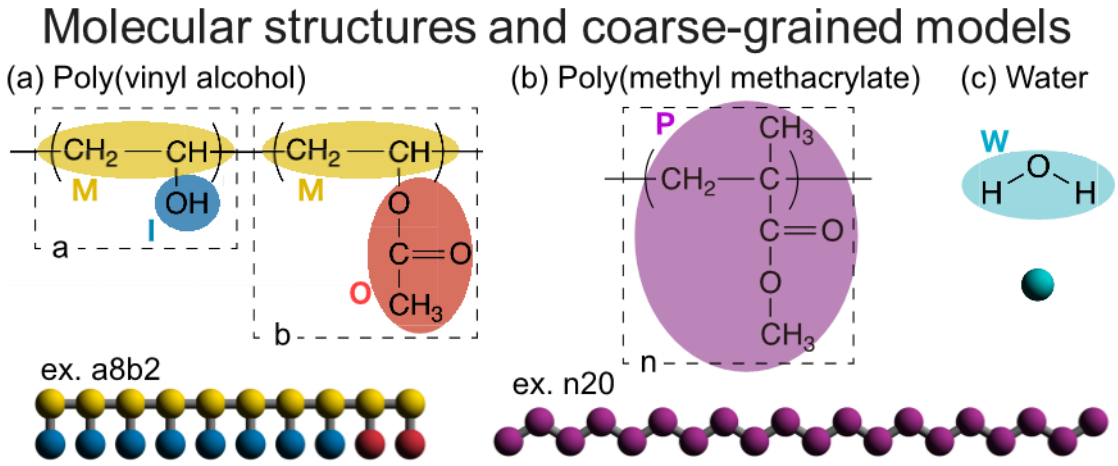

Fig. 4-1. Molecular structures and coarse-grained models of (a) PVA, (b) PMMA, and (c) water. The following beads are considered: the vinyl (yellow, "M"), hydroxy (blue, "I"), and acetyl (red, "O") groups of PVA; the PMMA unit (purple, "P"); and the water unit (cyan, "W").

The interaction parameters for $\mathbf{F}_{ij}^{C}$ between any two beads are related to the Flory-Huggins χ-parameters estimated from the mixing energy calculations. Consequently, a_{ij} is defined as follows:

$$a_{ij} = a_{ii} + 3.268\frac{V_{\text{seg}}}{RT}\left(\delta_i - \delta_j\right)^2, \tag{4.10}$$

where V_{seg} is the average molar volume of beads *i* and *j*, *R* is the gas constant, and δ is the bead solubility parameter. The parameters for the PVA molecules were inspired by a previous study [9], whereas those for PMMA were determined using the same approach as that in previous studies [10, 14, 15] using J-OCTA simulation software [16]. All-atom molecular dynamics simulations were performed to estimate the solubility parameters δ and molar volume V_{m} by calculating the cohesive energy of each bead. The Lennard-Jones potential of a general assisted model building with energy refinement (AMBER) force field (GAFF) [17] and molecular orbital calculations were used for the force field and charge values, respectively (see Table 4-2 for a summary of the interaction parameters).

Table 4-2. Interaction parameters a_{ij} in the expression for $\mathbf{F}_{ij}^{C}$ (Eq. 4.4) for all pairs. All values[a] are given in $k_{\mathrm{B}}T/r_{\mathrm{c}}$ units.

	M	I	O	P	W
M	18.75	61.01	20.23	18.95	39.75
I		18.75	48.77	67.48	23.94
O			18.75	19.51	30.48
P				18.75	35.06
W					18.75

[a] M: main chain, I: hydrophilic side chain, O: hydrophobic side chain, P: PMMA, W: water

A biphasic system with PVA molecules placed at the interface between water and PMMA beads was constructed as the initial configuration. Notably, the PMMA beads were treated as frozen particles based on previously reported findings [18-21], because the relaxation time of this amorphous polymer is longer than that of liquids. The initial PMMA configuration for the biphasic system was determined as follows. First, a biphasic water-PMMA system was simulated to obtain an equilibrium structure. Subsequently, the PMMA beads were frozen, and PVA molecules were added to the water phase of the biphasic system. Two different volume fractions of PVA molecules (ϕ) were considered (0.05 and 0.10), with ϕ defined as the ratio between the number of PVA beads and the total number of oil and water beads. The volume of the simulation box was $30\,r_{\mathrm{c}} \times 30\,r_{\mathrm{c}} \times 40\,r_{\mathrm{c}}$ for $\phi = 0.0$, and the edge length of the simulation box in the *z*-th direction was adjusted to achieve $\rho = 4\,r_{\mathrm{c}}^{-3}$ for $\phi > 0.0$. Periodic boundary conditions were applied to all three dimensions. The effects of temperature on PVA adsorption on the surface of PMMA were investigated at three temperatures: $1.0\,k_{\mathrm{B}}T$, $1.5\,k_{\mathrm{B}}T$, and $2.0\,k_{\mathrm{B}}T$. The noise parameter σ and friction parameter γ were set to 3.0 and 4.5, respectively. The time step *dt* was 0.01. All simulations were performed using the HOOMD-Blue software package (version 2.9.7) [22, 23].

4.3 Results

4.3.1 Emulsion Observations

Emulsification using various types of PMMA-PVAs

Figure 4-2 shows PEs prepared using the PMMA-PVA (synthesized with three types of PVA) and PMMA particles. The ϕ_D value and particle concentration were fixed at 0.46 and 1.5 wt%, respectively. Emulsion prepared using PMMA particles showed phase separation immediately after stirring, and a uniform PE was not formed. However, when using PMMA-PVA (PVA saponification: 80 or 88 mol%), PE was formed with a uniform appearance and no oil phase separation. On the other hand, PMMA-PVA (PVA saponification > 96 mol%) caused phase separation. These results suggest that PVA containing 10–20 mol% acetyl groups is suitable for PE formation.

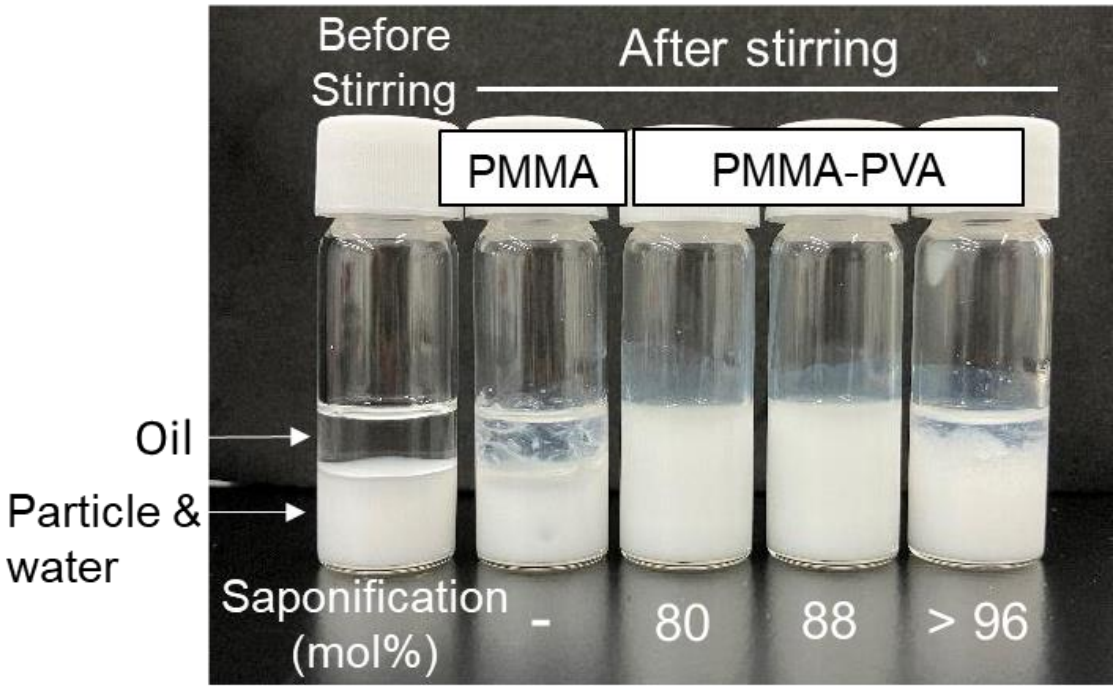

Fig. 4-2. Result of emulsification using PMMA and PMMA-PVA particles with ϕ_D= 0.46.

Storage stability of emulsions

The continuous phase of 1.5 wt% PMMA-PVA emulsions with varying ϕ_D values (0.11–0.83) was visually monitored (Fig. 4-3a). The continuous phase appeared clouded owing to the dispersion of PMMA-PVA ("before stirring"). All samples formed emulsions soon after stirring (0 day). Notably, after 14 days of storage, the emulsions with ϕ_D < 0.63 separated into two or three phases: a cream phase (upper layer) and an aqueous phase with or without particles (lower layer and a clear middle layer, respectively). After 86 days, the three phases were more clearly separated than the case after 14 days. In particular, the emulsion with $\phi_D = 0.83$ did not flow when the vial was turned upside down, suggesting gel-like behavior (Fig. 4-2b).

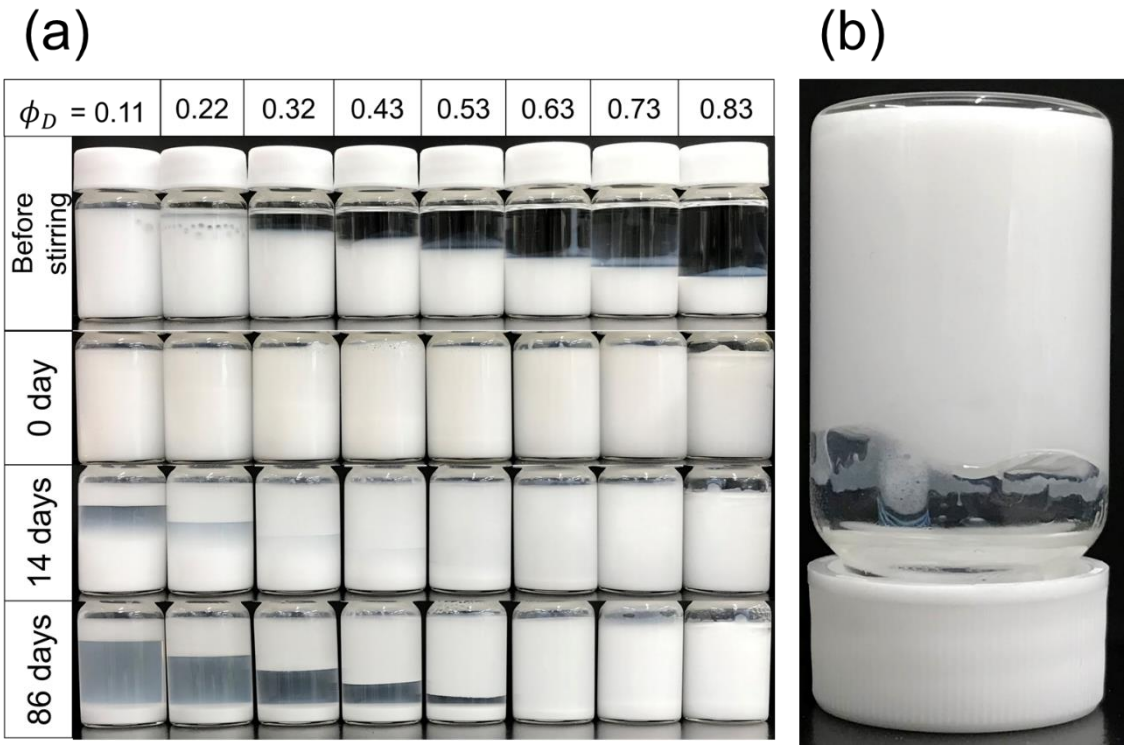

Fig. 4-3. (a) Photographs of emulsions stabilized by 1.5 wt% PMMA-PVA (88 mol%) with ϕ_D = 0.11–0.83 during storage at 25 °C. (b) Photograph of the inverted sample with $\phi_D = 0.83$ after 15 days of storage.

Microscopic analysis

Optical microscopic images (Fig. 4-4) confirmed that oil droplets did not exist in the bottom aqueous phase (Fig. 4-4a) but were present in the cream phase (Fig. 4-4b). This tendency was consistently observed for ϕ_D values ranging from 0.11 to 0.53. However, in the sample with $\phi_D = 0.63$, a few droplets were observed in the bottom aqueous phase (Fig. 4-4f). In the specimens with $\phi_D > 0.63$, the droplets became more concentrated and smaller as ϕ_D increased (Figs. 4-4b to 4-4d). In the sample with $\phi_D = 0.83$, the concentrated droplets began to rupture immediately after starting the observation. Specifically, two minutes later all the droplets became connected to each other, forming polyhedral droplets (Fig. 4-4e).

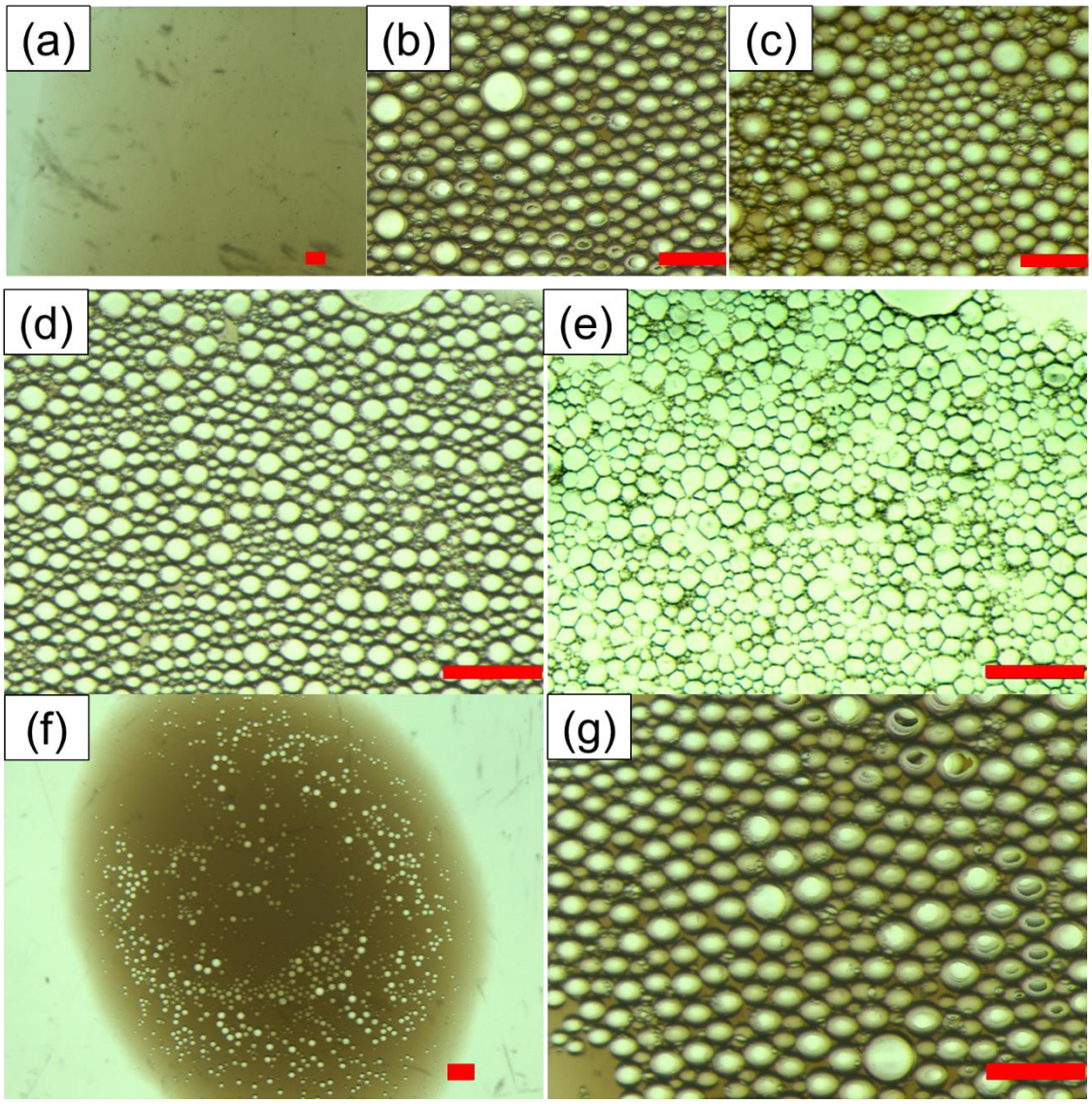

Fig. 4-4. Microscopic images of emulsions stabilized by 1.5 wt% PMMA-PVA (88 mol%): (a) aqueous phase ($\phi_D = 0.53$), (b–d) emulsion phase with (b) $\phi_D = 0.53$, (c) $\phi_D = 0.73$, (d) $\phi_D = 0.83$, and (e) $\phi_D = 0.83$ and recorded 2 min after (d). (f) Aqueous layer and (g) cream layer with $\phi_D = 0.63$. Red scale bar in each image represents 200 μm.

CLSM observation

To clarify the type of emulsion (O/W or W/O), stained DMCPS was used during emulsification. I observed fluorescent-labeled PMMA-PVA particles (yellow) surrounding DMCPS droplets (red) in water (Fig. 4-5a), confirming that PMMA-PVA formed an O/W emulsion. In Fig. 4-5b, fluorescent-labeled PMMA-PVA (green) enveloped the oil droplets. Most droplets were densely packed but effectively separated by PMMA-PVA, which functioned as an immobile wall. Furthermore, certain droplets exhibited hexagonal shapes, corroborating the observation in Fig. 4-4e.

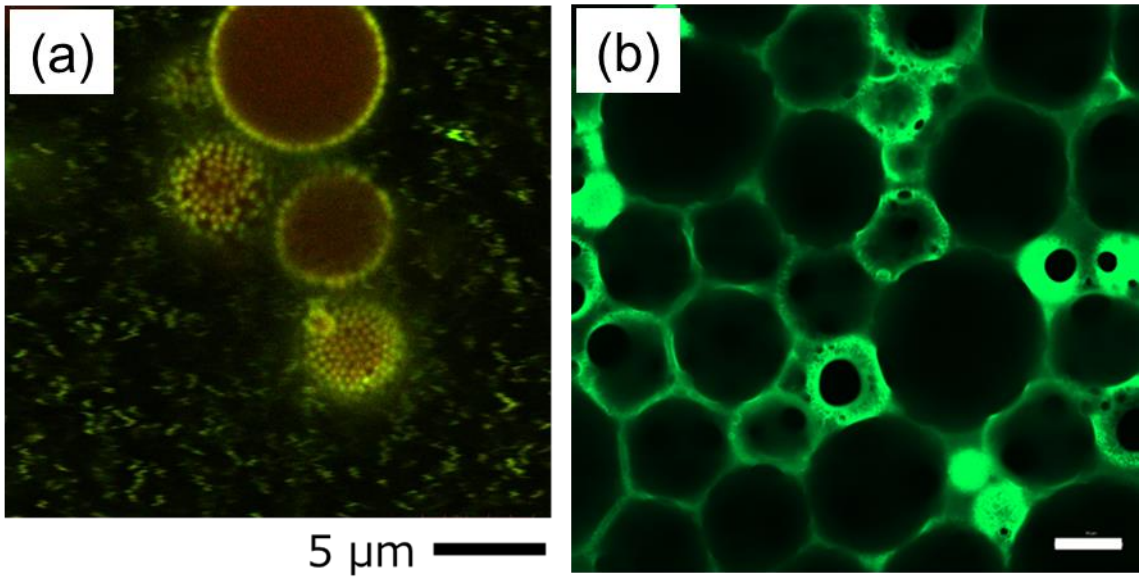

Fig. 4-5. (a) Confocal microscopic image of the emulsion using DMCPS stained by Nile Red (red) and coumarin-6 (yellow)-labeled PMMA-PVA (88 mol%). Scale bar: 5 μm. (b) Confocal microscopic image of the emulsion with $\phi_D = 0.77$ and stabilized by coumarin-6 (green)-labeled PMMA-PVA (88 mol%). Scale bar: 50 μm.

4.3.2 Evaluation of Synthetic Samples

SEM observation

SEM imaging of the PMMA particles (Fig. 4-6a) revealed monodisperse particles with a diameter of 356 ± 11 nm. SEM imaging of the coumarin-6-labeled PMMA particles indicated that they exhibited a diameter of 352 ± 10 nm and a highly narrow size distribution (Fig. 4-6b); the estimated particle diameter is like that of the coumarin-6-free PMMA particles.

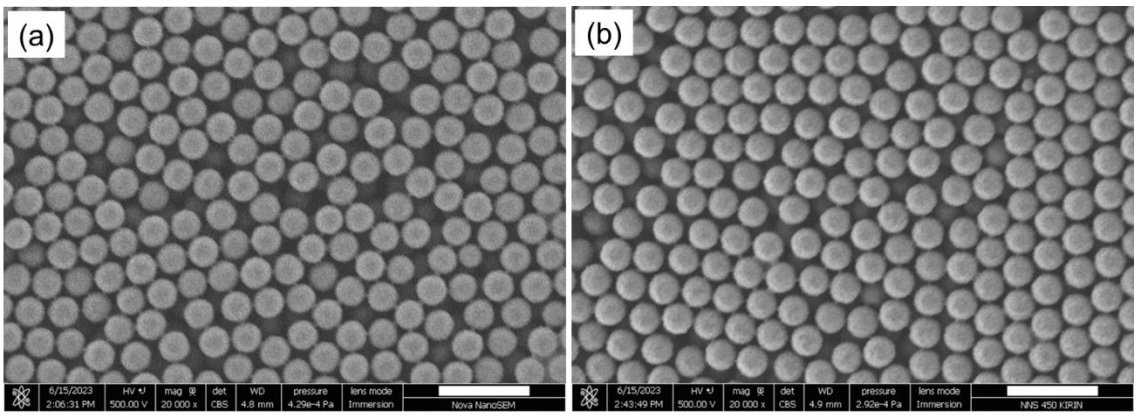

Fig. 4-6. Representative SEM image of the PMMA particles. (a): PMMA particles without coumarin-6. (b): PMMA particles with coumarin-6 (scale bar: 1 μm).

Characteristics of PMMA-PVA

All the PMMA and PMMA–PVA specimens exhibited narrow size distributions, with PDI values less than 0.1 (Table 4-3). Moreover, the $D(H)$ values of PMMA–PVA prepared using the PVA specimens with saponification degrees of 80 and 88 mol% were higher than that of the PMMA particles. In contrast, the $D(H)$ value of PMMA–PVA with fully hydrolyzed PVA was almost identical to that of the PMMA particles. Moreover, analysis of the ALT suggested that the ALT for PMMA–PVA with the partially hydrolyzed PVA specimens (80 and 88 mol%) was ~15 nm, but that of PMMA–PVA with fully hydrolyzed PVA was barely detected. These results suggested that the PVA with a lower saponification degree efficiently adsorbed onto the PMMA particles as a layer. Moreover, the decrease in Zeta potential for the specimens with partially hydrolyzed PVA substantiated the formation of the adsorbed layer.

Table 4-3. DLS analysis of the PMMA and PMMA–PVA specimens (n = 3).

Sample	Saponification of PVA (mol%)	$D(H)$ (nm)	PDI (-)	Zeta potential (mV)	ALT (nm)
PMMA	-	410 ± 3	0.08 ± 0.05	32 ± 1	-
PMMA-PVA	80	441 ± 3	0.02 ± 0.01	23 ± 3	15 ± 3
PMMA-PVA	88	440 ± 7	0.04 ± 0.01	22 ± 1	15 ± 5
PMMA-PVA	> 96	407 ± 1	0.02 ± 0.02	29 ± 8	−2 ± 2

Dispersion stability in the presence of NaCl

The effect of NaCl concentration on the stability of PMMA and PMMA-PVA particle dispersions was investigated. No changes were observed in the $D(H)$ values of PMMA-PVA (88 mol%) and PMMA-PVA (80 mol%) in 0.001–1 mol/L NaCl (Fig. 4-7). However, in 0.1 mol/L NaCl PMMA showed a significant increase in $D(H)$, whereas PMMA-PVA (>96 mol%) showed a slight increase. In 1 mol/L NaCl, the $D(H)$ values of PMMA and PMMA-PVA (>96 mol%) increased drastically to >1500 nm, indicating particle aggregation. Notably, salt resistance was observed in PMMA particles incorporating partially hydrolyzed PVA with saponification degrees of 80 or 88 mol%.

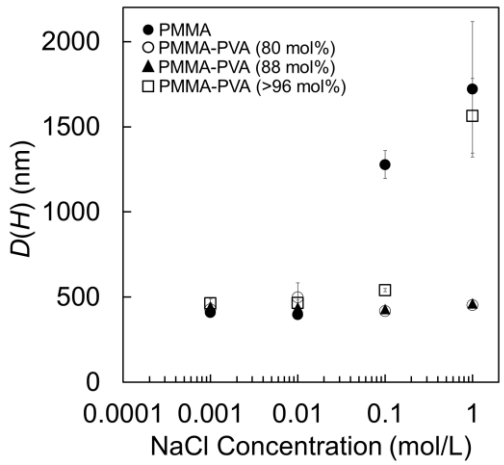

Fig. 4-7. Measured $D(H)$ values of PMMA and PMMA-PVA dispersions in aqueous NaCl solutions. Solid particle content: 10 mg/L (n = 3).

Extraction of insoluble fractions

Soxhlet extraction was conducted to confirm the adsorption of PVA onto the PMMA particles. Chloroform was used as the extractant because of its efficiency in dissolving PMMA but not PVA. According to the results (Fig. 4-8), no residue was obtained from the freeze-dried PMMA particles, but a chloroform-insoluble fraction of 5.3% was obtained for the freeze-dried PMMA-PVA (88 mol%) particles.

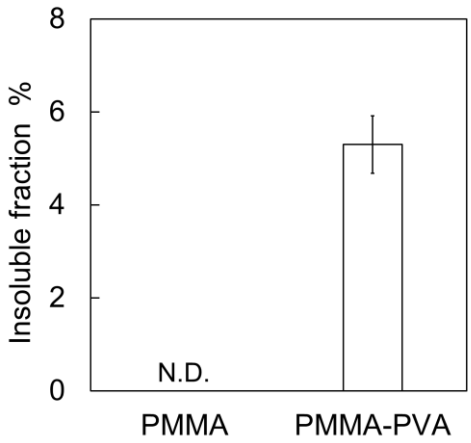

Fig. 4-8. Chloroform-insoluble fractions of PMMA and PMMA-PVA (88 mol%) particles, as obtained by Soxhlet extraction. n = 3. N.D.: not detected.

FTIR analysis

FTIR spectroscopy was used to explore the characteristics of the chloroform-insoluble fraction. In the obtained spectra (Fig. 4-9), all samples exhibited an absorbance peak at ~1,720 cm^{-1}, corresponding to carbonyl stretching. Moreover, the spectra of the chloroform-insoluble fraction (Fig. 4-9a) and PVA (88 mol%) (Fig. 4-9b) both showed a broad peak at ~3,400 cm^{-1}, which was ascribed to the hydroxyl group. In contrast, the freeze-dried PMMA particles did not display this peak (Fig. 4-9c). A spectral library search using the data in Fig. 4-9a suggested the presence of 88 mol% hydrolyzed PVA (concordance rate: 75.55%). The difference spectrum between the chloroform-insoluble fraction and PVA (88 mol%) (Fig. 4-9d) does not include the hydroxyl peak. Moreover, a spectral library search using the data in Fig. 4-9d suggested the presence of PMMA (concordance rate: 87.01%). Therefore, the chloroform-insoluble fraction was confirmed to be mostly PVA, with a smaller portion of PMMA residue.

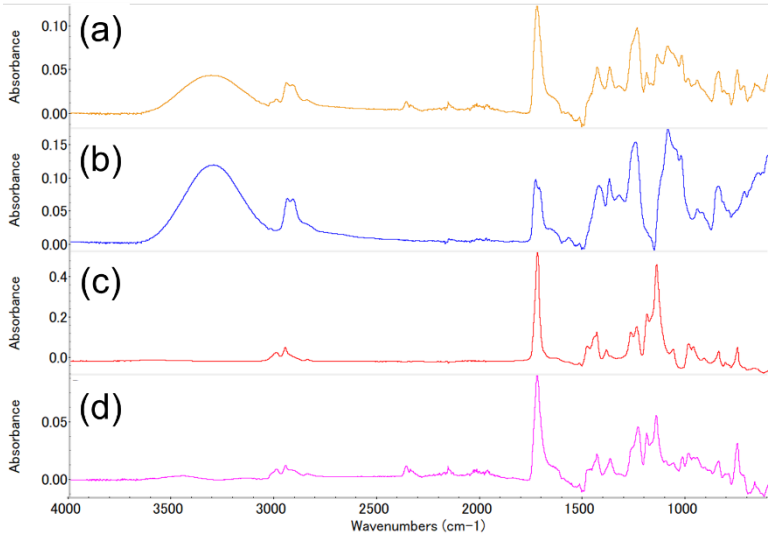

Fig. 4-9. FTIR spectra of (a) chloroform-insoluble fraction of PMMA-PVA (88 mol%) particles, (b) PVA (88 mol%), and (c) PMMA. (d) Difference spectra between (a) and (b).

GPC

GPC analysis (Table 4-4) showed that the M_w value of the PMMA particles was around 600,000, and that PMMA and PMMA-PVA (88 mol%) have similar M_n and M_w values. Therefore, adsorption of PVA had only an insignificant effect on the M_n and M_w of PMMA. Notably, the M_n and M_w values of the chloroform-insoluble fraction were approximately two folds higher than those of PVA (88 mol%). Furthermore, it is possible that the PMMA residue in the chloroform-insoluble fraction influenced the structure of PVA dissolved in the HFIP eluent.

Table 4-4. GPC measurement results of the PMMA, PVA (88 mol%), and PMMA-PVA (88 mol%) particles, as well as their chloroform-insoluble fraction.

	M_n ($\times 10^5$) (g/mol)	M_w ($\times 10^5$) (g/mol)	M_w/M_n (-)
PMMA	1.5	5.8	3.9
PMMA-PVA（88 mol%）	1.3	5.6	4.3
PVA (88 mol%)	0.39	0.82	2.1
Insoluble fraction	0.75	1.5	2.0

Interfacial tension

The kinetics of particle adsorption at the oil surface was studied using pendant drop tensiometry. The IT value between water and DMCPS showed no significant decrease over time (33.4 ± 0.2 mN/m at 1,200 s, Fig. 4-10a). The dynamic IT of 0.1 wt% aqueous PVA solution decreased slightly over the course of 1200 s (Fig. 4-10a), whereas that of 1 wt% PMMA dispersion was almost constant, decreasing by only ~1 mN/m from 300 to 1,200 s (Fig. 4-10b). For PMMA-PVA (80, 88, and >96 mol%), their IT values decreased from 0 to 1,200 s by 15.0, 10.6, and 5.9 mN/m, respectively. This change is smaller for PVA with a lower degree of saponification, which is consistent with the behavior of aqueous PVA solutions. The IT values remained almost constant after 1,200 s for the samples with 1% PMMA-PVA (Fig. 4-10c). Moreover, IT decreased with increasing PMMA-PVA particle concentration.

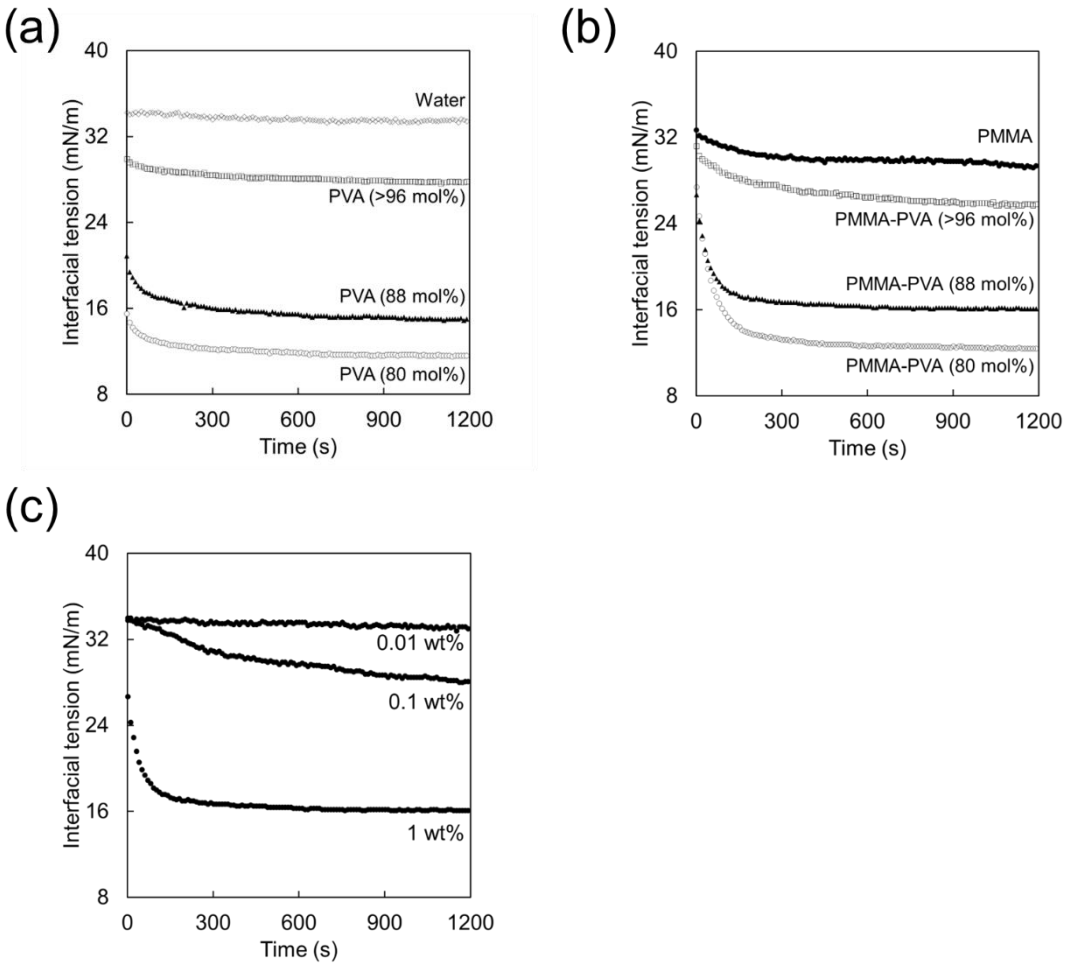

Fig. 4-10. Dynamic interfacial tension (IT) of the water-DMCPS interface. (a) Water and 0.1 wt% aqueous PVA solutions, (b) 1 wt% PMMA and PMMA-PVA dispersions, and (c) concentration-dependent IT of the PMMA-PVA (88 mol%) particle dispersion. All measurements were performed using the aqueous solution or dispersion droplets suspended in DMCPS. Measurements were conducted in triplicate, and the average value was plotted.

4.3.3 Simulation of PVA adsorption

To acquire molecular-level insights into the experimental results, I performed coarse-grained molecular simulations to reveal the effects of PVA saponification degree on PVA adsorption onto the PMMA surface. Snapshots of the biphasic system were acquired using the ratio between the number of PVA beads and the total number of oil and water beads, ϕ value of 0.05, and the degree of saponification, *f* values of 0.8 and 1.0 at various temperatures (Fig. 4-11). At $1.0\,k_{\mathrm{B}}T$, all PVA molecules with *f* = 0.8 adsorbed onto the PMMA surface, whereas some fully hydrolyzed PVA molecules (*f* = 1.0) remained in the water phase owing to their high hydrophilicity (Figs. 4-11a and 4-11d, respectively). Notably, the difference in adsorption behavior between *f* = 0.8 and *f* = 1.0 became more pronounced at higher temperatures. For example, at $2.0\,k_{\mathrm{B}}T$ the partially hydrolyzed PVA (*f* = 0.8) remained at the water-PMMA interface (Fig. 4-11c), whereas the fully hydrolyzed PVA penetrated the water phase (Fig. 4-11f).

Focusing on the adsorption behavior of PVA with *f* = 0.8 onto PMMA, I analyzed the molecular distributions at the water-PMMA interface and plotted the number density distributions corresponding to the acquired snapshots (Fig. 4-12). For $\phi = 0.05$, there were sharp peaks of PVA corresponding to the vinyl, hydroxy, and acetyl groups at the water-PMMA interface, indicating the formation of an adsorbed PVA layer on the PMMA surface (Fig. 4-12b). Notably, the number of PVA molecules adsorbed onto the PMMA surface increased with an increase in the number of PVA molecules to $\phi = 0.10$ (Fig. 4-12c). Furthermore, distinct peaks of the main chain (vinyl, "M") and hydrophobic side chain (acetyl, "O") in the water phase emerged at $r \approx 11.2\,r_{\mathrm{c}}$ and $r \approx 11.7\,r_{\mathrm{c}}$, respectively (Fig. 4-12d). This indicated that partially hydrolyzed PVA formed a sufficiently adsorbed monolayer, resulting in the appearance of acetyl groups near the aqueous phase.

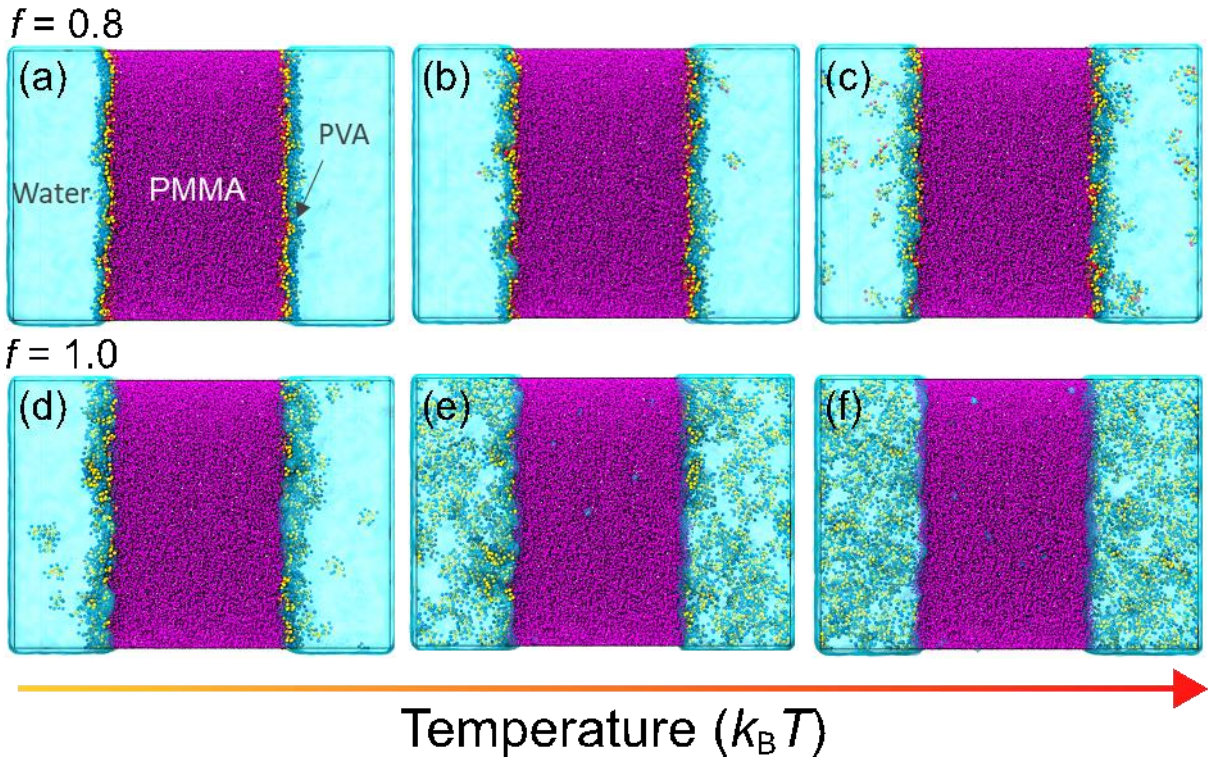

Fig. 4-11. Representative simulation snapshots of biphasic systems of (a–c) f = 0.8 and (d–f) f = 1.0 at various temperatures: (a, d) 1.0 k_BT, (b, e) 1.5 k_BT, and (c, f) 2.0 k_BT.

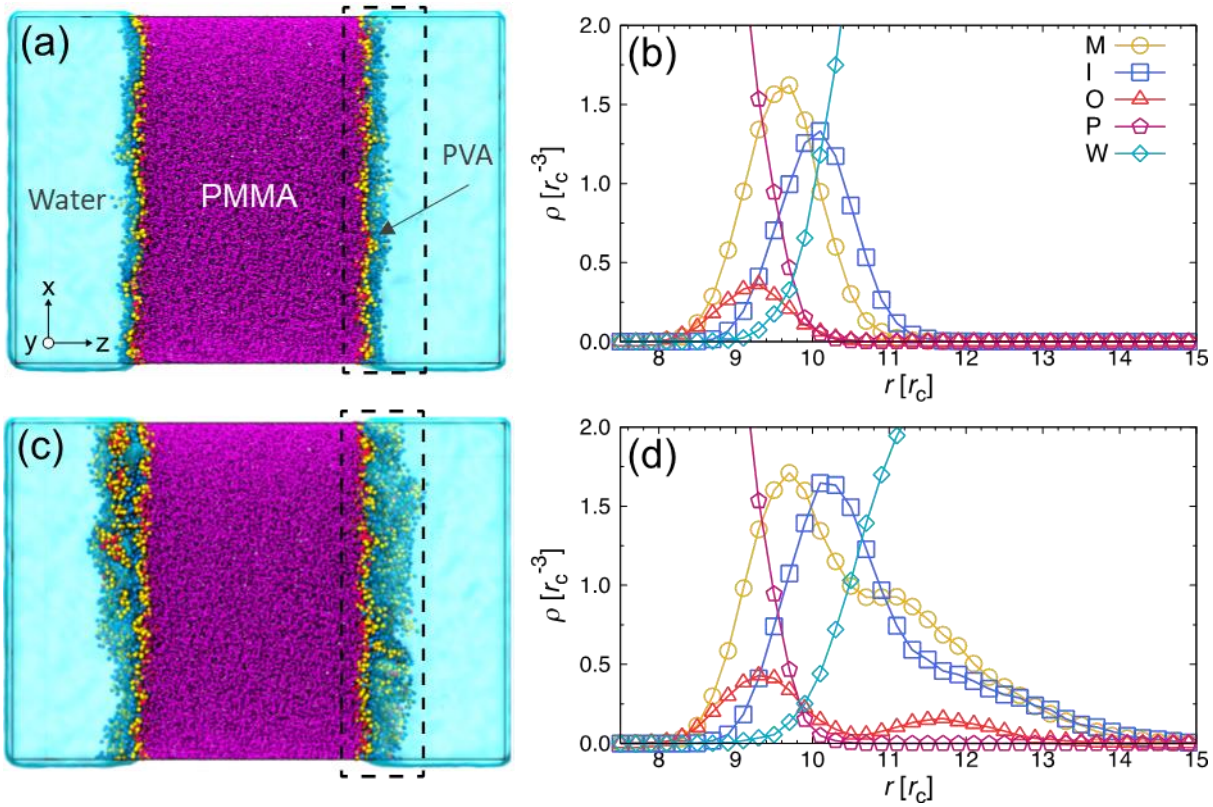

Fig. 4-12. Representative simulation snapshots of biphasic systems and number density profiles in the *z*-direction for (a, b) $\phi = 0.05$ and (c, d) $\phi = 0.10$. M: main chain (vinyl group) of PVA, I: hydrophilic side chain (hydroxy group) of PVA, O: hydrophobic side chain (acetyl group) of PVA, P: PMMA, W: water.

4.4 Discussion

4.4.1 Characteristics of Pickering Emulsions Stabilized by PMMA-PVA

Immediately after stirring, the emulsions were homogenous under all the tested conditions. However, particle sedimentation and creaming occurred after 14 and 86 days of storage, respectively. Notably, the emulsions stabilized by PMMA-PVA with $\phi_D = 0.63$ differed from those with $\phi_D = 0.53$, because creaming did not occur in the former as evidenced by macroscopic (Fig. 4-3a) and microscopic droplet observations (Figs. 4-3a, f, and g). According to Li *et al.* [24] and Yang *et al.* [25], emulsions stabilized by microgel particles and starch nanocrystals with ϕ_D < 0.6 quickly separate into a cream layer and an aqueous solution layer. Here, creaming occurred because of the difference in density between DMCPS (0.96 g/mL) and water (1.00 g/mL). Therefore, a smaller density difference and a higher viscosity of the continuous phase should help prevent phase separation according to the Stokes equation (Eq. 2.3).

4.4.2 High Internal Oil Phase Pickering Emulsion

The emulsion with $\phi_D = 0.83$ exhibited a gel-like behavior (Fig. 4-3b), and its droplet shape changed drastically from spherical (Fig. 4-4d) to faceted (Fig. 4-4e) in a few minutes. Although these phenomena are representative of high internal phase Pickering emulsions (HIPPEs) [24-29], the corresponding microscopic images (Fig. 4-4e) included certain artifacts because the emulsions were thinly spread on glass plates for examination. For a more thorough analysis, an emulsion stabilized by fluorescent-labeled PMMA-PVA with $\phi_D = 0.77$ was imaged by CLSM without spreading. This emulsion contained faceted droplets (Fig. 4-5b), strongly suggesting that the bulk emulsion was an O/W HIPPE. The state of HIPPEs is affected by the number and size of particles and inter-particle interactions [26, 27]. The number of particles in the continuous phase can be readily controlled, because the dispersion of PMMA particles can be concentrated by centrifugation during the post-polymerization stage. Moreover, size control of PMMA particles from 100 to 400 nm has been previously achieved using SFEP [30].

The inter-particle interactions in PMMA-PVA can induce intermolecular hydrogen bonding between PVA units on PMMA particle surface. After modification with PVA, a decrease in the repulsive electrostatic forces was observed, affording a reduction in the zeta potential of the particles (Table 4-3). The densely packed oil droplet immobilized by PMMA-PVA (Fig. 4-5b) indicated that there were friction forces. As a result, I assumed that attractive forces surpassed the repulsive forces, resulting in stronger inter-particle interactions that affected the stability of HIPPE.

Overall, these factors including the number of particles, particle size, and inter-particle interactions should be considered in more detail when studying HIPPEs stabilized by PMMA-PVA in the future.

4.4.3 Properties of PMMA-PVA

DLS measurements and ALT calculations revealed that the PVA specimens hydrolyzed at 80 and 88 mol% formed a robust layer on the PMMA particle surface (Table 4-3). The presence of PVA on the surface led to a change in the zeta potential (approximately +30 and +20 mV for PMMA and PMMA-PVA particles, respectively), with the positive charges of the PMMA particles originating from the imidazolium group of ADIP-Cl [30]. This reduction in zeta potential was due to an outward shift of the slipping plane by the adsorbed layer of PVA. Notably, PLGA-PVA with a negative charge deriving from the carboxylic end group also showed an increase in its hydrodynamic diameter because of PVA adsorption and a reduction in the zeta potential [1, 2]. Moreover, analysis of the amount of chloroform-insoluble fraction of PMMA-PVA (Fig. 4-8) and the associated FTIR study (Fig. 4-9) confirmed the presence of ~5 wt% PVA on the PMMA surface. Furthermore, the PMMA particles aggregated in 0.1 mol/L aqueous NaCl solution, but PMMA-PVA (80 and 88 mol%) particles did not coalesce even in 1 mol/L NaCl (Fig. 4-7). In conclusion, the resistance of the PMMA-PVA system against aggregation in NaCl was attributed to PVA acting as a protective colloid.

The chloroform-insoluble fraction of PMMA-PVA was comprised of PVA together with some PMMA residues (Fig. 4-9d). The hydroxy group of PVA forms intermolecular hydrogen bonds with C=O in the acetyl group of PMMA [31]. It was therefore assumed that the freeze-dried powder of PMMA-PVA partially maintained its hydrogen bonding during extraction. As a result, some PMMA was not extracted but remained in the residue.

PVA hydrolyzed to >96 mol% did not form a sturdy layer on the PMMA particles (Table 4-3). In the electrolyte resistance test, PMMA-PVA (>96 mol%) exhibited suppressed and notable aggregation in 0.1 and 1 mol/L aqueous NaCl solutions, respectively (Fig. 4-7). Furthermore, the IT values of PMMA-PVA (>96 mol%) were slightly lower than those of the PMMA particles (Fig. 4-11b). Additionally, DPD simulations of the biphasic system showed that as the temperature increased, fully hydrolyzed PVA dissociated from the PMMA surface in water (f = 1.0; Figs. 4-11d to 4-11f) compared to partially hydrolyzed PVA (f = 0.8; Figs. 4-11a to 4-11c). These results strongly suggest that surface coverage of the PMMA particles was insufficient when utilizing PVA without non-hydrolyzed acetyl group, because this group worked as an anchor for adsorption onto the PMMA surface.

4.4.4 Interfacial Adsorption Behavior of PMMA-PVA

When the aqueous phase was a dispersion of PMMA particles in water, the IT value was slightly lower than that of the control (water) (Figs. 4-10a and 4-10b). This finding is consistent with several studies on the thermodynamically favorable adsorption and surface activity of PLGA nanoparticles [1, 2]. Notably, the IT values decreased non-uniformly with respect to time: decreasing from 0 to 300 s, remaining constant from 300 to 900 s, and then decreasing slightly again from 900 to 1,200 s (Fig. 4-10b). The PMMA particles adsorbed at the interface in a reversible manner owing to their Brownian motion in water and inter-particle interactions *via* electrostatic repulsion.

The IT values of aqueous PVA solutions decreased with decreasing degree of PVA saponification, and this trend was reflected in the PMMA-PVA dispersions. Furthermore, the 0.1 wt% aqueous PVA solution at 1,200 s and 1 wt% PMMA-PVA dispersion had almost identical IT values. Considering that the chloroform-insoluble fraction of PMMA-PVA, which mainly comprised PVA, was ~5 wt% (Fig. 4-8), 1 wt% PMMA-PVA dispersion should contain ~0.05 wt% PVA. Therefore, the decrease in IT was driven by PVA. The IT curves of PMMA-PVA dispersions indicated that the adsorption kinetics was dominated by Brownian motion and irreversible particle adsorption at the interface. The concentration-dependent measurements (Fig. 4-10c) showed that 0.01 wt% PMMA-PVA was insufficient for decreasing IT, indicating a lack of particles for interfacial coverage. The IT decrease driven by particle diffusion was more dominant in the 0.1 wt% dispersion than in the 1 wt% one. In particular, the sample at the maximum particle content (1 wt%) showed a sharp reduction in IT, because it had enough particles to achieve interfacial coverage in the initial state of dynamic IT analysis.

The molecular-level DPD simulation results suggested that the number of partially hydrolyzed PVA molecules adsorbed at the PMMA surface increased with increasing number of PVA molecules, as demonstrated by the appearance of acetyl groups near the aqueous phase (Fig. 4-12). Overall, the experimental findings indicated that PMMA-PVA efficiently reduced IT as the degree of saponification of PVA decreased. Moreover, the simulation and experimental results suggested that the acetyl group of PVA helped reinforce the O/W emulsion stabilized by PMMA-PVA.

4.5 Summary

In Chapter 4, it was demonstrated that the formation of particle-stabilized O/W emulsion is determined by the hydrolysis level of PVA molecule utilized to modify the surface of submicron cationic PMMA particles. Moreover, I found that hydrophobic interaction between the acetyl group of PVA molecule and PMMA surface is important for forming a PVA layer on the PMMA particle surface.

In more detail, O/W emulsions including O/W HIPPEs were prepared using PMMA-PVA. The adsorption of PVA on the PMMA particle surface was confirmed *via* zeta potential analysis, aggregation tests against NaCl, and extraction experiments. I demonstrated that partially hydrolyzed PVA facilitated the formation of this PVA layer. Furthermore, coarse-grained molecular simulations strongly suggested that the PVA layer was formed *via* adsorption onto the PMMA surface, with the acetyl group acting as an anchor. In contrast, fully hydrolyzed PVA, which contained few acetyl group, could only adsorb through its main chain and hence failed to form a surface layer. These results suggest that successful adsorption of PVA in water can be attributed to the hydrophobic interactions between the acetyl group of PVA and PMMA. Furthermore, PMMA particles with a robust PVA layer were efficient in reducing IT when the PVA had a lower degree of saponification. At the molecular level, when a robust and sufficient layer was created by partially hydrolyzed PVA, the acetyl groups adsorbed on PMMA and were located near the aqueous phase. Therefore, I predict that the total particle wettability would be change by the acetyl group near the aqueous phase. These O/W emulsions including O/W HIPPEs stabilized by PMMA-PVA are promising for applications in cosmetics, healthcare, emulsion-templated scaffolds, and biomedicine such as tissue engineering.

4.6 References

[1]. Albert, C., Huang, N., Tsapis, N., Geiger, S., Rosilio, V., Mekhloufi, G., Chapron, D., Robin, B., Beladjine, M., Nicolas, V., Fattal, E., & Agnely, F. (2018). Bare and sterically stabilized PLGA nanoparticles for the stabilization of Pickering emulsions. *Langmuir*, 34(46), 13935-13945.

[2]. Robin, B., Albert, C., Beladjine, M., Legrand, F. X., Geiger, S., Moine, L., Nicolas, V., Canette, A., Trichet, M., Tsapis, N., Agnely, F., & Huang, N. (2021). Tuning morphology of Pickering emulsions stabilised by biodegradable PLGA nanoparticles: How PLGA characteristics influence emulsion properties. *J. Colloid Interface Sci.*, 595, 202-211.

[3]. Tiemeyer, C., Lange, A., & Plank, J. (2014). Determination of the adsorbed layer thickness of functional anionic polymers utilizing chemically modified polystyrene nanoparticles. *Colloids Surf. A*, 456, 139-145.

[4]. Stecher, J., & Plank, J. (2020). Adsorbed layer thickness of polycarboxylate and polyphosphate superplasticizers on polystyrene nanoparticles measured via dynamic light scattering. *J. Colloid Interface Sci*., 562, 204-212.

[5]. Hoogerbrugge, P. J., & Koelman, J. M. V. A. (1992). Simulating microscopic hydrodynamic phenomena with dissipative particle dynamics. *Europhys. Lett.*, 19(3), 155.

[6]. Groot, R. D., & Warren, P. B. (1997). Dissipative particle dynamics: Bridging the gap between atomistic and mesoscopic simulation. *J. Chem. Phys.*, 107(11), 4423-4435.

[7]. Han, D., Mao, J., Zhao, J., Zhang, H., Wang, D., Wang, C., Xue, J., Cao, H., Yang, X., Lin, C., Zhang, Y., & Fu, M. (2022). Dissipative particle dynamics simulation and experimental analysis of the effect of anionic/cationic mixed surfactants on the stability of emulsions. *J. Mol. Liq.*, 367, 120482.

[8]. Chang, H. Y., Tsao, H. K., & Sheng, Y. J. (2023). Solid-like elastic behavior of nanosized concentrated emulsions: Size-dependent Young's and bulk moduli. *J. Mol. Liq.*, 380, 121745.

[9]. Suzuki, K., Kobayashi, Y., Yamazaki, T., Tsuji, T., & Arai, N. (2024). Mechanisms underlying the stability and instability of concentrated oil-in-water emulsions: Effect of the chemical structure of amphiphilic polymers. *J. Mol. Liq.*, 394, 123749.

[10]. Araki, Y., Kobayashi, Y., Kawaguchi, T., Kaneko, T., & Arai, N. (2018). Water permeation in polymeric membranes: Mechanism and synthetic strategy for water-inhibiting functional polymers. *J. Membr. Sci.*, 564, 184-192.

[11]. Liu, D., Yang, M., Wang, D., Jing, X., Lin, Y., Feng, L., & Duan, X. (2021). DPD Study on the interfacial properties of PEO/PEO-PPO-PEO/PPO ternary blends: effects of pluronic structure and concentration. *Polymers*, 13(17), 2866.

[12]. Liu, D., Lin, Y., Bo, H., Li, D., Gong, K., Zhang, Z., & Li, S. (2022). Effect of sequence distribution of block copolymers on the interfacial properties of ternary mixtures: a dissipative particle dynamics simulation. *RSC Adv.*, 12(5), 3090-3096.

[13]. Groot, R. D., & Rabone, K. L. (2001). Mesoscopic simulation of cell membrane damage, morphology change and rupture by nonionic surfactants. *Biophys. J.*, 81(2), 725-736.

[14]. Arai, N., Kobayashi, Y., & Yasuoka, K. (2020). A biointerface effect on the self-assembly of ribonucleic acids: a possible mechanism of RNA polymerisation in the self-replication cycle. *Nanoscale*, 12(12), 6691-6698.

[15]. Yokoyama, T., Miwake, H., Hamaguchi, M., Nakatake, R., & Arai, N. (2023). Reproduction of super-multicomponent self-assembled structures and their functionality using coarse-grained molecular simulation–the example of cleansing agents. *Mol. Syst. Des. Eng.*, 8(4), 538-550.

[16]. JSOL Corporation, J-OCTA, https://www.j-octa.com (accessed 13 December 2024).

[17]. Wang, J., Wolf, R. M., Caldwell, J. W., Kollman, P. A., & Case, D. A. (2004). Development and testing of a general amber force field. *J. Comput. Chem.*, 25(9), 1157-1174.

[18]. Chen, C., Gao, C., Zhuang, L., Li, X., Wu, P., Dong, J., & Lu, J. (2010). A many-body dissipative particle dynamics study of spontaneous capillary imbibition and drainage. *Langmuir*, 26(12), 9533-9538.

[19]. Chen, C., Zhuang, L., Li, X., Dong, J., & Lu, J. (2012). A many-body dissipative particle dynamics study of forced water–oil displacement in capillary. *Langmuir*, 28(2), 1330-1336.

[20]. Arai, N., Yasuoka, K., & Zeng, X. C. (2012). Nanochannel with uniform and Janus surfaces: Shear thinning and thickening in surfactant solution. *Langmuir*, 28(5), 2866-2872.

[21]. Kobayashi, Y., & Arai, N. (2017). Self-assembly and viscosity behavior of Janus nanoparticles in nanotube flow. *Langmuir*, 33(3), 736-743.

[22]. Anderson, J. A., Glaser, J., & Glotzer, S. C. (2020). HOOMD-blue: A Python package for high-performance molecular dynamics and hard particle Monte Carlo simulations. *Comput. Mater. Sci.*, 173, 109363.

[23]. Phillips, C. L., Anderson, J. A., & Glotzer, S. C. (2011). Pseudo-random number generation for Brownian Dynamics and Dissipative Particle Dynamics simulations on GPU devices. *J. Comput. Phys*., 230(19), 7191-7201.

[24]. Li, Z., Ming, T., Wang, J., & Ngai, T. (2009). High internal phase emulsions stabilized solely by microgel particles. *Angew. Chem. Int. Ed.*, 48(45), 8490-8493.

[25]. Yang, T., Zheng, J., Zheng, B. S., Liu, F., Wang, S., & Tang, C. H. (2018). High internal phase emulsions stabilized by starch nanocrystals. *Food Hydrocolloids*, 82, 230-238.

[26]. Kaganyuk, M., & Mohraz, A. (2019). Role of particles in the rheology of solid-stabilized high internal phase emulsions. *J. Colloid Interface Sci.*, 540, 197-206.

[27]. Kaganyuk, M., & Mohraz, A. (2019). Impact of particle size on droplet coalescence in solid-stabilized high internal phase emulsions. *Langmuir*, 35(39), 12807-12816.

[28]. Rodriguez, A. M. B., & Binks, B. P. (2022). High internal phase Pickering emulsions. *Curr. Opin. Colloid Interface Sci.*, 57, 101556.

[29]. He, X., & Lu, Q. (2024). A review of high internal phase Pickering emulsions: Stabilization, rheology, and 3D printing application. *Adv. Colloid Interface Sci.*, 324, 103086.

[30]. Yamazaki, T., Ogawa, A., Koizumi, H., & Tsuji, T. (2021). Controlled soap-free emulsion polymerization stability using a novel cationic azo radical initiator with chloride or triflate counter anion. *Colloids Surf. A*, 609, 125614.

[31]. Mitani, E., Ozaki, Y., & Sato, H. (2022). Two types of C=O···HO hydrogen bonds and OH···OH (dimer, trimer, oligomer) hydrogen bonds in PVA with 88% saponification/PMMA and PVA with 99% saponification/PMMA blends and their thermal behavior studied by infrared spectroscopy. *Polymer*, 246, 124725.

Chapter 5 Encapsulation of Ultraviolet Absorber into Cationic Polystyrene Particles by Miniemulsion Polymerization using Poly(vinyl alcohol)

5.1 Introduction

Sunlight plays a vital role in the health of humans and many animals by promoting vitamin D synthesis [1], regulating circadian rhythms [2], and enhancing mood [3]. However, extended exposure to sunlight can lead to detrimental overexposure to UV rays, which elevates the risks of sunburn and skin cancer [4]. Organic UV filters capable of absorbing UVB (280–320 nm) and UVA (320–400 nm) light have been formulated and incorporated into various consumer products including cosmetics [5]. Due to the intrinsic ability of aromatic moieties to absorb UV rays, organic UV filters tend to be polar oils or insoluble solids, which complicates their dissolution or uniform dispersion in water-based cosmetic formulations.

Miniemulsion polymerization can effectively produce aqueous dispersions of polymer particles containing encapsulated materials [6, 7]. The standard formulation for miniemulsion polymerization consists of monomer droplets (with or without encapsulated material), water, surfactant, and a water-soluble radical initiator [8–10]. Several researchers have used this method to synthesize particles encapsulating UV filters [11–13], but those studies all had some shortcomings. First, the initial emulsification process requires a substantial quantity of emulsifier, such as sodium dodecyl sulfate, that has been shown to cause skin irritation when incorporated into the final cosmetic product [14–16]. Even if the emulsifier is subsequently removed, this step requires extra energy and may generate environmentally harmful effluents. Thus, it is imperative to establish a cost-effective miniemulsion polymerization procedure employing only materials that are both skin-safe and environmentally benign.

Second, the synthesized particles possess a negative electrical charge due to remnants of anionic radical initiators such as potassium peroxodisulfate (KPS) [8–10]. Cosmetic formulations with UV blocking capabilities have to adhere well to the skin and/or hair to create a protective film. Because the surface of hair fiber carries negative charge, positively charged sunscreen components are more easily retained there through electrostatic force [17]. Nevertheless, research on cationic UV absorbers remains scant [18].

To address existing limitations of UV absorbers for cosmetic applications, in this chapter I employed miniemulsion polymerization and a cationic radical initiator to prepare UV-filter-encapsulating particles, utilizing PVA as an alternative to conventional emulsifiers. Two types of

PVA were considered as potential polymer-based emulsifiers. PVA is known to be biocompatible [19] and biodegradable [20] and has a long history in effectively stabilizing emulsions [21–25]. However, it has hardly been delpoyed as an emulsifying agent in miniemulsion polymerization, because the conventional PVA molecule has poor stabilizing capacity for emulsion or miniemulsion polymerization, as mentioned in Section 1.3.6. In contrast, I revealed that low-molecular-weight PVA was quite effective for preparing miniemulsion droplets and polymer particles with high contents of UV absorber in this study.

Specifically, I synthesized cationic PS particles containing a UVA filter {diethylamino hydroxybenzoyl hexyl benzoate (DHHB)} using PVA and a cationic radical initiator {2,2'-azobis[2-(2-imidazolin-2-yl)propane]dihydrochloride (VA-044)}, as depicted in Fig. 5-1. Comprehensive analyses were conducted on the particle size, size distribution, and surface charge of DHHB-encapsulated PS particles (PS-DHHB). Furthermore, the content of DHHB within PS-DHHB was quantified, and the particles' UV absorbance was assessed to determine their efficacy as a UV filter. Leaching tests of PS-DHHB were conducted in aqueous alcohol solutions, given that such solutions are often employed as antibacterial agents in cosmetic products. The adsorption capabilities of cationic and anionic PS-DHHB to hair fibers were compared. Lastly, hair protein degradation induced by UVA irradiation was monitored in the presence of both PS-DHHB and unmodified PS particles.

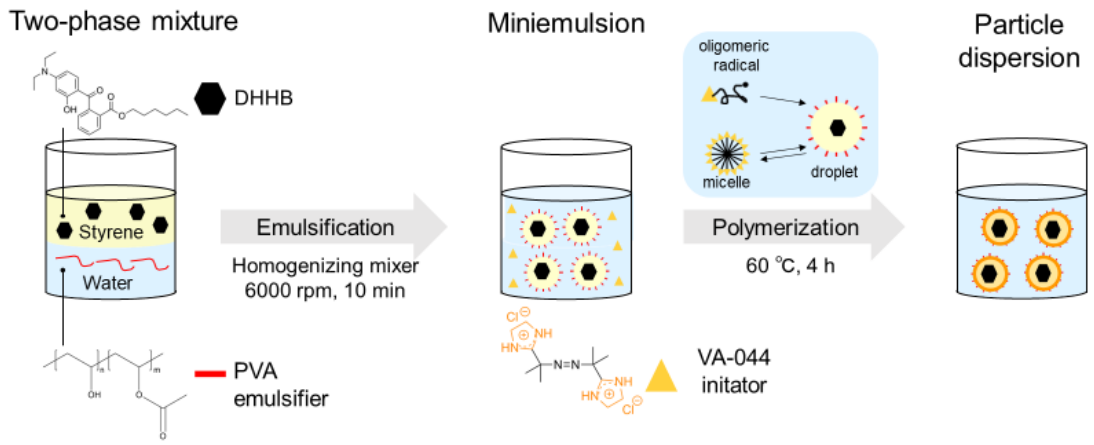

Fig. 5-1. Schematic of the preparation of DHHB-encapsulated PS particles.

5.2 Materials & Methods

5.2.1 Reagents

Water treated with reverse osmosis and electrodeionization (RO plus EDI) was employed for all experimental procedures. Acetonitrile, chloroform, ethanol (99.5%), KPS, tetrahydrofuran (THF), VA-044, and other chemicals were acquired from Fujifilm Wako Pure Chemical Corporation, Japan. DHHB, styrene, 1,2-pentanediol, 1,2-hexanediol, and 1,3-butanediol were sourced from Tokyo Chemical Industry Corporation, Japan. Additional reagents including Dulbecco's phosphate-buffered saline (DPBS, catalog number: 14190-144), Pierce™ BCA Protein Assay Kit (catalog numbers: 23225 and 23227), and Pierce™ bovine serum albumin (BSA) standard ampules (2 mg/mL, catalog number: 23209) were obtained from Thermo Fisher Scientific, USA. The inhibitor remover (catalog number: 311340) was obtained from Sigma-Aldrich Corporation (USA).

PS with a weight-average molecular weight (M_w) of 300,000 was sourced from Toyo Styrene Co., Ltd., Japan, while that with an M_w of 50,000 was acquired from Polysciences, Inc., USA. Two types of PVA with different degrees of polymerization and saponification were supplied by Japan Vam & Poval Co., Ltd., Japan, namely JP-05 {degree of polymerization (D.P.), 500; degree of saponification (D.S.), 88 mol%} and JMR-3H {D.P., 110; D.S., 78 mol%}. The dynamic viscosities of JP-05 and JMR-3H in 4 wt% aqueous solutions were found to be 4.99 ± 0.02 and 1.79 ± 0.01 mPa·s, and their interfacial tensions (IT) in 0.1 wt% aqueous solutions suspended in

styrene were 6.7 ± 0.0 and 1.7 ± 0.1 mN m^{-1}, respectively. These properties are summarized in Table 5-1.

Table 5-1. Properties of PVA.

PVA	D.P.[a]	D.S.[a]	D.V.[b]	IT[c]
		mol%	mPa/s^{-1}	mN m^{-1}
JP-05	500	88	4.99 ± 0.02	6.7 ± 0.0
JMR-3H	110	78	1.79 ± 0.01	1.7 ± 0.1

[a] Manufacturer's specifications; [b] 4 wt% aqueous solution; [c] 0.1 wt% aqueous solution suspended in styrene. The values are presented as mean ± standard deviation (n = 3).

The dynamic viscosity of PVA aqueous solutions was ascertained using a ViscoQC 300-L viscometer (Anton Paar, Austria). For temperature regulation at 25 °C and measurement, temperature devices and sensors (PTD 80) as well as a spindle (SC4-18) were utilized. Interfacial tension was determined through pendant drop tensiometry aided by a DMo-502 contact angle meter (Kyowa Interface Science Co., Ltd., Japan). A blunt-tipped needle with an outer diameter of 0.7 mm was used to introduce a droplet of aqueous PVA solution into styrene. All measurements were conducted at 25 ± 1 °C and 45 ± 5% relative humidity. Experimental images of droplets were analyzed using the Young-Laplace equation in FAMAS software (version 7.2.0, Kyowa Interface Science Co., Ltd., Japan). The densities of styrene and PVA solution were recorded as 0.91 and 1.00 g/mL, respectively. The reported experimental values include the standard deviations from three separate trials. A representative image utilized for calculating IT is displayed in Fig. 5-2.

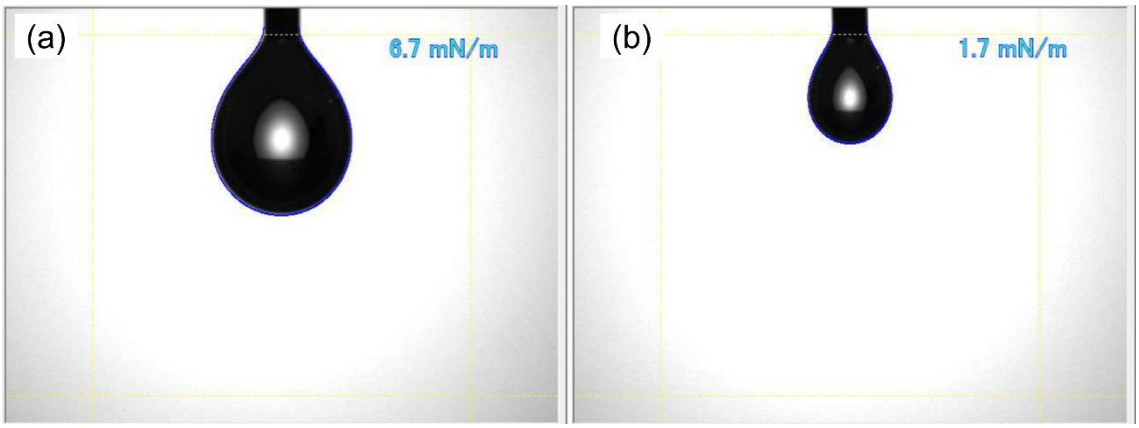

Fig. 5-2. Representative photographs of aqueous droplets of (a) 0.1 wt% JP-05 at 300 s after starting the measurement and (b) 0.1 wt% JMR-3H 89 s after starting the measurement. Both droplets were suspended in styrene for IT analysis.

5.2.2 Emulsification

Emulsification was conducted utilizing a LABOLUTION system equipped with a Homogenizing Mixer Mark II Model 2.5 as the mixing head (PRIMIX Corporation, Japan). Prior to use, styrene was treated with inhibitor remover to eliminate 4-*tert*-butylcatechol. In the standard procedure, a PVA solution (4 g) was added to water (185 g) in a 500-mL disposable polypropylene container. Subsequently, styrene (45 g) containing DHHB (15 g) was gradually introduced into the aqueous PVA solution. The mixture was initially stirred at 2,000 rpm and subsequently homogenized at 6,000 rpm. When employing PS as a stabilizer for the polymerization process, it was pre-dissolved in the styrene monomer and stirred overnight at 4 °C. The average hydrodynamic diameter [$D(H)$] of the emulsion droplets was determined using a DLS instrument (Zetasizer Nano ZSP, Malvern Instruments Limited, UK) equipped with a 10-mW He-Ne laser operating at a wavelength of 633 nm. Data collection and analysis were executed using Dispersion Technology software (version 7.13; Malvern Instruments Limited). The instrument was set to operate in the backscatter mode at an angle of 173° (noninvasive backscatter, NIBS®), with 12 runs conducted on each sample to determine the size distribution by number. Following homogenization, argon gas was introduced into the emulsion for 10 min to remove oxygen.

Emulsification tests using PVA were conducted as follows. Styrene (2.25 g), aqueous PVA solution, and water were combined in a glass vial (height, 45 mm; inner diameter, 24 mm) to achieve a total solution mass of 10 g. Emulsification was conducted using an NS-310E3 apparatus

fitted with an NS-7A mixing head (Micro-Tec Co., Ltd., Japan). The styrene and water phases were homogenized at 2,500 rpm for 1 min, followed by emulsification at 12,500 rpm for another 1 min. The size distribution by number of emulsion droplets was measured.

5.2.3 Synthesis of DHHB-Encapsulated Polystyrene Particles (PS-DHHB)

The amounts of each component used in the synthesis of PS-DHHB are detailed in Table 5-2. All emulsions were prepared as described in Section 5.2.2 and then transferred to a 300-mL reactor featuring an inner diameter of 75 mm, a baffle board, and a three-necked lid. Thereafter, the emulsion was heated, and a solution of the radical initiator VA-044 (0.47 g) in water (1 g) was added. Polymerization ensued with mechanical stirring for 4 h at 60 °C, facilitated by a sealing mixer (UZ-SM1, Nakamura Scientific Instruments Industry Co., Ltd., Japan) and a propeller-shaped stirring rod (∅8 mm × 300 mm). After polymerization, all particle dispersions were evaluated for any significant odors (which indicates incomplete polymerization) before cooling to 25 °C for characterization.

Anionic PS-DHHB was prepared as follows. The amounts each component used in synthesis are detailed in Table 5-2, and emulsions were prepared as described in Section 5.2.2. Each emulsion was transferred to a 300-mL reactor featuring an inner diameter of 75 mm and a baffle board. After heating the emulsion, water (1 g) containing the radical initiator KPS (0.39 g, Entry S2 in Table 5-2) was introduced. Polymerization was conducted for 4 h at 60 °C.

Table 5-2. Components and characteristics of emulsions prepared at 60 °C. In all cases, the amount of PVA was 4 g.

Entry	Styrene (g)	PS (g)	DHHB (g)	Water (g)	Initiator	Initiator (g)	Rotation speed (rpm)
1	45	0	15	186	VA-044	0.47	450
2	45	0	15	186	VA-044	0.47	120
3	40.5	4.5 [a]	15	186	VA-044	0.47	120
4	40.5	4.5 [b]	15	186	VA-044	0.47	120
S1	45	0	0	151	VA-044	0.47	120
S2	45	0	15	186	KPS	0.39	120

[a] M_w = 300,000; [b] M_w = 50,000

5.2.4 Characterization of PS-DHHB

The Z-average $D(H)$ and PDI of PS-DHHB were determined using DLS, as described in Section 5.2.2. The zeta potential was assessed using a Zetasizer Nano ZSP instrument with the M3-PALS® method. A minimum of 10 runs were performed for each sample to determine the zeta potential. All measurements were conducted at 25 °C. The viscosity and relative permittivity of water were assumed to be 0.89 mPa·s and 78.5, respectively. Henry's function (1.5) was utilized for zeta potential calculations. The concentration of PS-DHHB ($C_{PS-DHHB}$, Table 5-3) in the dispersion was determined from the oven-dried weight of 0.3 g PS-DHHB dispersion.

Observations of PS-DHHB were conducted at an acceleration voltage of 500 V and a magnification of 20,000× (Fig. 5-7). PS-DHHB in its dried state (Entry 2) was directly observed on aluminum foil.

UV-visible (UV-vis) absorbance spectra were acquired with a BioMate TM 160 spectrophotometer (Thermo Fisher Scientific, Inc., USA). Water and THF served as the blanks for particle dispersion and particles dissolved in THF, respectively.

The DHHB content in the PS particles (C_{DHHB}) was quantified using a Shimadzu Prominence high-performance liquid chromatography (HPLC) system (Shimadzu Corporation, Japan) fitted with an octadecyl-silica column (250 mm × 4.6 mm, 5 μL; OSAKA SODA CO., LTD., Japan). Acetonitrile served as the mobile phase and was flowed at a rate of 0.5 mL/min for 11 min. The column temperature was set at 40 °C, the injection volume was 1 μL, and the absorbance at 350

nm was measured using a UV-vis detector (SPD-20MA). Data collection and analysis were performed using LabSolutions Version 5.101 (Shimadzu Corporation, Japan). To prepare the sample, 150 μL of PS-DHHB dispersion was centrifuged at 20,400 g for 15 min, and the supernatant was discarded. The precipitate was dissolved in 150 μL of THF containing 850 μL of chloroform, followed by sonication for 15 min. This dispersion was then diluted with acetonitrile and passed through a PTFE membrane filter with a pore size of 0.2 μm. A standard solution was also prepared by dissolving DHHB in acetonitrile.

The polymer content ($C_{Polymer}$) was calculated using Eq. (5.1).

$$C_{Polymer} = C_{PS-DHHB} - C_{DHHB} \tag{5.1}$$

The yield was calculated using Eq. (5.2).

$$\text{Yield } \% = \frac{C_{PS-DHHB}}{Theoretical\ solid\ contents} \times 100 \tag{5.2}$$

The encapsulation efficiency was calculated using Eq. (5.3).

$$\text{Encapsulation efficiency } \% = \frac{C_{DHHB}}{Theoretical\ contents\ of\ DHHB} \times 100 \tag{5.3}$$

PS-DHHB (Entry 2) after washing was characterized as follows. The PS-DHHB dispersion (A 150 μL) was centrifuged at 20,400 g for 15 min to eliminate excess monomer and PVA. The precipitate was added with water (1 mL) and dispersed. The dispersion underwent centrifugation, and a 50 vol% ethanol solution was added to the precipitate for dispersion and removal of DHHB. After a third centrifugation step, the concentration of DHHB in the ethanol supernatant was quantified using a spectrophotometer. DLS was employed to measure $D(H)$, PDI, and the zeta potential.

The ratio of DHHB in the ethanol washing fluid was calculated using Eq. (5.4).

$$\text{DHHB in washing fluid}\% = \frac{DHHB\ \ in\ 50\ vol\%\ Ethanol}{DHHB\ in\ the\ polystyrene\ particle\ (C_{DHHB})} \times 100 \tag{5.4}$$

Table 5-3. Contents of PS-DHHB ($C_{PS-DHHB}$) and PS computed from the dispersions.

Entry	$C_{PS-DHHB}$ (wt%)
1	19.1
2	24.4
3	24.6
4	25.5
S1	21.5
S2	21.0

5.2.5 Evaluation of DHHB Leaching from Particles into Aqueous Alcohol Solution

A dispersion of PS-DHHB (20 mg; Table 3, Entry 2) was introduced into a 1.5-mL tube, to which various alcohols (ethanol, 1,2-hexanediol, 1,2-pentanediol, and 1,3-butanediol) were added to achieve the minimum inhibitory concentration (MIC) described in the literature [26]. Water was incorporated into the mixture to standardize the final concentrations of PS-DHHB (0.05 wt%) and alcohol. The samples were then incubated at 50 °C for 24 h and centrifuged at 20400 *g* for 45 min. Afterwards, 150 µL of the supernatant was diluted with 850 µL of acetonitrile.

For the positive control (PC), PS-DHHB dispersion (20 mg, Entry 2) and THF (100 µL) were thoroughly mixed in a 1.5-mL tube. Chloroform (600 µL) was subsequently added, followed by 15 min of sonication. The sonicated sample (10 µL) was diluted with acetonitrile (990 µL). All prepared samples were passed through a PTFE membrane filter with a pore size of 0.2 µm.

The contents of DHHB in the supernatant containing each alcohol or PC were determined *via* HPLC, as described in Section 5.2.4. According to the HPLC analysis, the relative amounts of DHHB in the aqueous alcohol solutions were calculated using Eq. (5.5).

$$\text{Relative amount of DHHB in aqueous alcohol solution} = \frac{C_{Sample}}{C_{PC}} \quad (5.5)$$

where C_{PC} represents the DHHB content in PC, and C_{sample} represents the DHHB content in the aqueous alcohol solution.

5.2.6 Evaluation of PS-DHHB Adsorption on Hair

Human hair that had been bleached white served as the experimental substrate. The hair was immersed in water (control), cationic PS-DHHB (Entry 2), or anionic PS-DHHB (Entry S2) dispersions for 10 min. After immersion, the hair was rinsed thrice by submersion in water for 5 min to eliminate residual particles before air drying at ambient temperature. The dried strands were cut to 1-cm pieces and examined under SEM at an accelerating voltage of 500 V and magnifications of 2,000× (Figs. 5-10a–c) or 8,000× (Fig. 5-10d). Each dried hair specimen was attached to carbon tape prior to SEM assessment.

5.2.7 Evaluation of Hair Protein Loss by UVA Irradiation

Bleached hair was soaked in either 1 wt% PS (Entry S1) or cationic PS-DHHB (Entry 2) dispersions for 10 min. The treated hair was allowed to dry at 25 °C for two days. The dried strands were subsequently exposed to radiation from a UVA lamp (FPL27BLB, Sankyo Denki Co., Ltd., Japan).

The cumulative amount of UVA irradiation was calculated using Eq. (5.6).

$$\text{Accumulated UVA Intensity } (\text{J/cm}^2) = I_{UVA}(\text{mW/cm}^2) \times T \text{ (s)} \quad (5.6)$$

where I_{UVA} represents the UVA intensity measured using a UV ray intensity meter (catalog number: UV-340C, CUSTOM Corporation, Japan), and T represents the irradiation time.

After UVA exposure, the hair samples were partially severed from the terminal end with a razor, weighed, and then submerged in water at 40 °C for 3 h to facilitate protein extraction. The water-to-hair weight ratio was 70. The protein concentration in the aqueous extract was quantified using the bicinchoninic acid (BCA) assay as follows [27]. The working reagent (WR) was formulated by combining Reagent A and Reagent B in a volumetric ratio of 50:1. On a 96-well plate, 25 µL of sample or standard solution was placed in each well. Then, 200 µL of WR was added to each well, followed by incubation at 37 °C for 30 min. The absorbance was subsequently recorded at 562 nm utilizing a microplate reader. The BSA standard was calibrated to concentrations from 0 to 50 µg/mL using DPBS. Statistical analysis was performed using Dunnett's test, with $p < 0.05$ considered significant. For the control, PS-treated (Entry S1), and PS-DHHB-treated (Entry 2) samples without UVA irradiation, their protein loss was found to be statistically insignificant (Fig. 5-3).

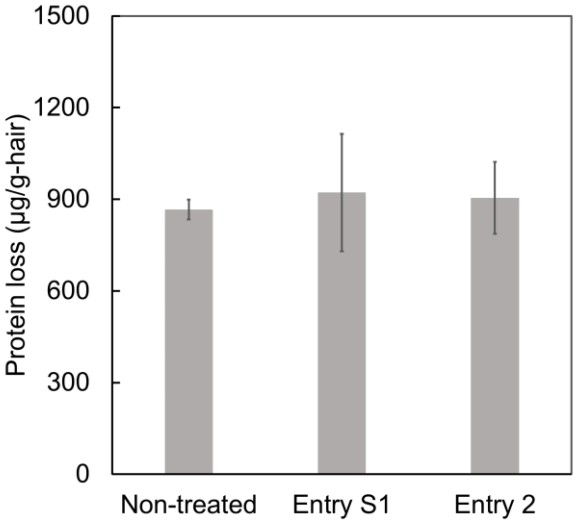

Fig. 5-3. Protein loss from non-treated hair sample and those treated with PS (Entry S1) and PS-DHHB (Entry 2). n = 3, mean ± standard deviation.

5.3 Results

5.3.1 Optimal Type of PVA for Miniemulsion Polymerization of Styrene

Different types of PVA were tested to generate small emulsion droplets while maintaining emulsion stability during deoxygenation prior to polymerization. Figure 5-4 shows the time-dependent size distribution of emulsion droplets formulated with two types of PVA, namely JP-05 and JMR-3H. The PVA content in the emulsion was fixed at 2 wt%, because preliminary tests indicated that droplet size is inversely correlated with the concentration of JMR-3H (Fig. 5-5). A unimodal droplet size distribution was observed in both cases. JP-05 reduced the droplet size from 5000 to 1000 nm, and the size further declined upon extending the duration of homogenization. However, during the deoxygenation stage preceding polymerization, emulsions employing JP-05 exhibited considerable bubble formation, which impeded polymerization (data not presented). In contrast, the droplet size in emulsions formulated with JMR-3H remained small and stable during homogenization, chiefly from 20 to 100 nm. Moreover, the JMR-3H-based emulsions showed no bubble formation during the deoxygenation phase. Thus, JMR-3H is more favorable for miniemulsion polymerization compared to JP-05, owing to its capacity for producing smaller droplets and maintaining emulsion stability throughout deoxygenation.

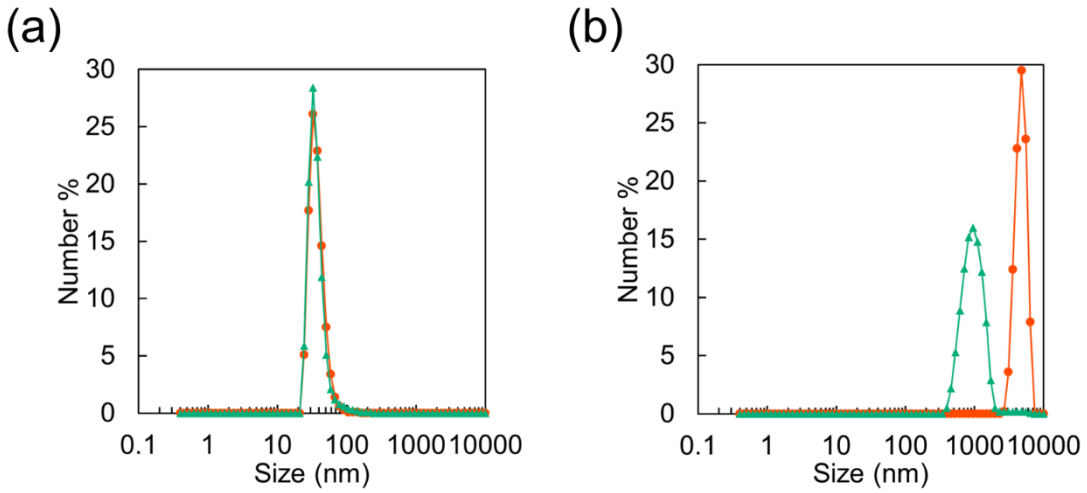

Fig. 5-4. Droplet size distribution (number %) for two types of PVA: (a) JMR-3H and (b) JP-05. Both emulsions contained 2 wt% PVA. Red curve: 2 min post-homogenization, green curve: 30 min post-homogenization.

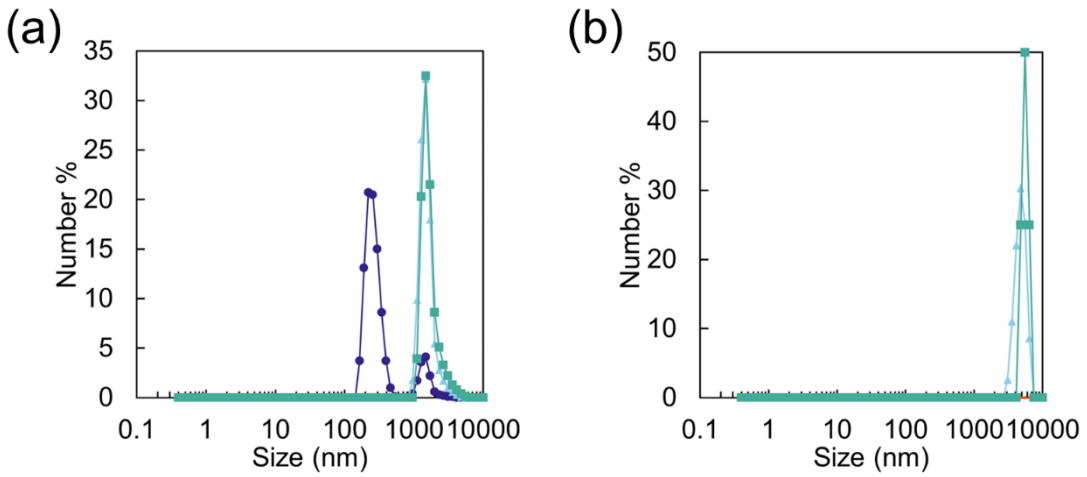

Fig. 5-5. Droplet size distribution (number %) for (a) JMR-3H and (b) JP-05. Indigo (circle), cyan (triangle), and teal (square) correspond to 2, 1, and 0.5 wt% PVA, respectively. The indigo line is not shown in (b) because the drop size exceeded the upper limit (6000 nm).

5.3.2 Polymerization Conditions for forming Stable and DHHB-rich PS-DHHB

Tables 5-2 and 5-4 present the synthesis components and characteristics of PS-DHHB formed at 60 °C, respectively. Figure 5-6 depicts the representative size distribution by number both before (as droplets) and after (as PS-DHHB) polymerization. Three criteria were used for assessment. First, the PDI should be less than 0.2, which signifies the absence of particle aggregation. Second, $C_{polymer}$ should be approximately 20 wt%, indicating complete conversion of the styrene monomer. Third, higher C_{DHHB} values are preferred because a lower value indicates suboptimal encapsulation of DHHB. All entries in Table 5-4 show PDI < 0.2, confirming a narrow size distribution and no particle aggregation. Entries 2–4 have $C_{polymer}$ ~20 wt% and gave a faint odor, whereas Entry 1 has $C_{polymer}$ = 13 wt% and gave a more pronounced odor that suggests incomplete polymerization. A slower stirring speed during polymerization led to higher conversion efficiency of the styrene monomer. Moreover, the inclusion of PS in the styrene monomer prior to polymerization elevated the C_{DHHB} value. This was particularly evident when PS with a lower molecular weight was used, such as in Entry 4. In this case, $C_{polymer}$ and C_{DHHB} were 19.9 and 6 wt%, respectively, indicating both near-complete conversion and successful encapsulation.

Figure 5-7 shows an SEM image of PS-DHHB (Entry 2), revealing particles with high monodispersity and the absence of smaller particles. Table 5-5 details the characteristics of Entry 2 after washing with either water or 50 vol% ethanol. Water was used to remove residual monomer or PVA, and 50 vol% ethanol was employed for DHHB removal. The $D(H)$, PDI, and zeta values remained consistent with those listed in Table 5-4. The DHHB extracted with 50 vol% ethanol accounted for 1.5% of the polymer emulsion, indicating that most of the DHHB was encapsulated, although some may reside in micelles or be adsorbed on the particle surface.

Table 5-4. Components and characteristics of emulsion polymerization product at 60 °C. In all cases, the amounts of DHHB, water, and PVA were 15, 186, and 4 g, respectively.

Entry	$D(H)$ (nm)	PDI (-)	Zeta potential (mV)	$C_{Polymer}$ (wt%)	C_{DHHB} (wt%)	Yield (%)	Encapsulation efficiency (%)
1	246	0.18	48	12.8	6.3	74	105
2	247	0.12	43	20.2	4.2	95	70
3	227	0.078	45	19.5	5.1	96	85
4	215	0.11	45	19.9	5.6	99	93
S1	255	0.11	43	21.5	0	94	0
S2	220	0.094	–53	16.3	4.7	86	77

Table 5-5. Characteristics of PS-DHHB (Entry 2) after washing.

Washing fluid	$D(H)$ (nm)	PDI (-)	Zeta potential (mV)	DHHB in washing fluid (%)
Water	230.3	0.099	48.3	N.D.
50 vol% EtOH	277.4	0.181	50.1	1.5

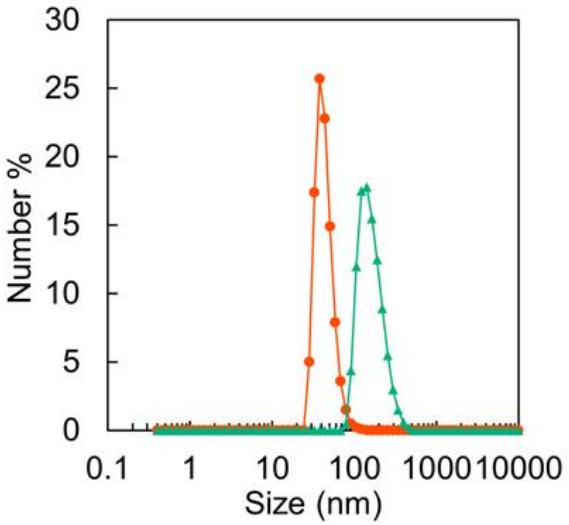

Fig. 5-6. Size distribution (number %) before (emulsion droplet, red line) and after (particle, green line) polymerization (Entry 2).

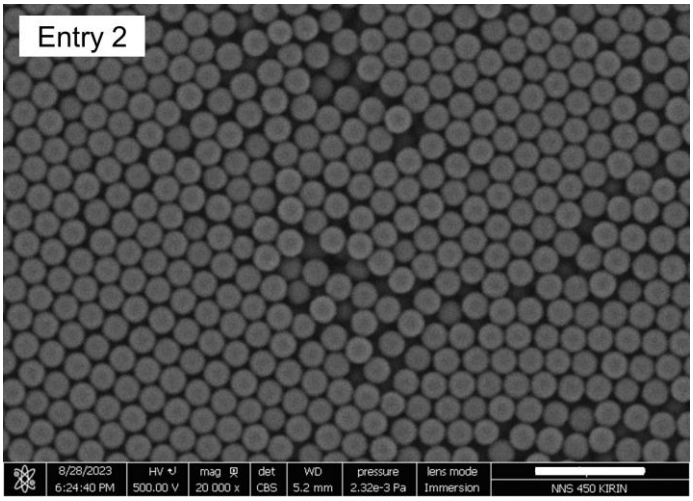

Fig. 5-7. A representative SEM image of PS-DHHB (Entry 2). White bar: 1 μm.

5.3.3 UV Absorption of PS-DHHB

The UV absorption spectrum of PS-DHHB (Entry 2) dispersed in THF is depicted in Fig. 5-8a, with the circles representing data points. The peak absorption wavelength (λ_{max}) occurs at 352 nm, which is close to the λ_{max} for DHHB dissolved in THF (black line). The similarity between these spectra implies an unaltered chemical structure of DHHB post-polymerization. The absorbance spectra of the PS-DHHB dispersion (Entry 2, black line), PS dispersion (Entry S1, dotted line), and clear liquid of Entry 2 (broken line, obtained by filtering the dispersion) are shown in Fig. 5-8b. The synthesis protocol for Entry S1 is presented in Table 5-2, and its characterization results are listed in Table 5-4. The λ_{max} value of Entry 2 is 362 nm. In contrast, no UVA absorption was detected in either the pristine PS particles (Entry S1) or the clear liquid of Entry 2, confirming that UVA absorption is exclusive to PS-DHHB.

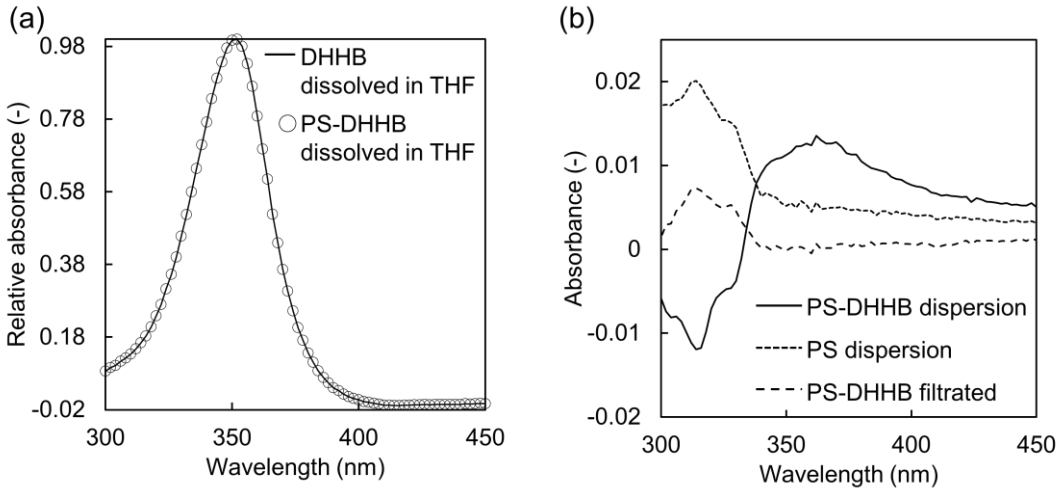

Fig. 5-8. (a) Absorbance spectra of the PS-DHHB dispersion (Entry 2, circles) and DHHB dissolved in THF (continuous line). Absorbance was normalized at the maximum absorption wavelength (352 nm). Entry 2 was diluted with THF by a factor of 10000. (b) Absorbance spectra of PS-DHHB dispersion (0.5 ppm, Entry 2, solid line), 0.5 ppm PS dispersion (Entry S1, dotted line), and clear liquid of Entry 2 after passing through a polysulfone membrane filter (pore size: 0.2 μm, broken line).

5.3.4 DHHB Leaching from PS-DHHB in Aqueous Alcohol

Figure 5-9 illustrates the relative DHHB content in aqueous alcohol extracted from PS-DHHB, based on three independent measurements. The relative DHHB concentration was calculated as described in Section 5.2.5. Alcohols are frequently utilized in cosmetic formulations to inhibit microbial growth [26]. The alcohols and their contents were: 10 wt% ethanol (E_10), 20 wt% 1,3-butanediol (B_20), 10 wt% 1,2-pentanediol (P_10), and 2.5 wt% 1,2-hexanediol (H_2.5). No traces of DHHB were found in any of the solutions, confirming that DHHB remained encapsulated within PS-DHHB.

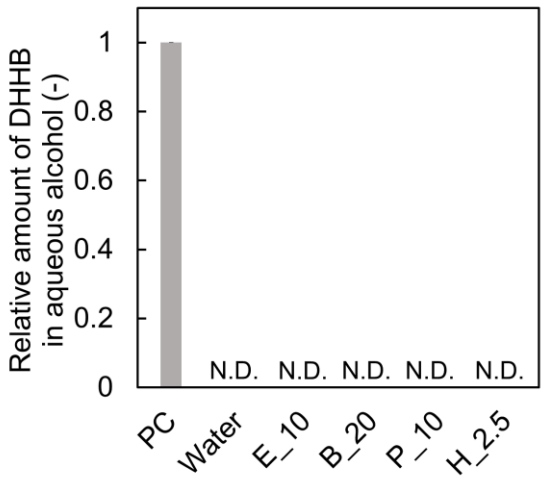

Fig. 5-9. Relative amount of DHHB in aqueous alcohols based on three independent measurements: PC, 10 wt% ethanol (E_10), 20 wt% 1,3-butanediol (B_20), 10 wt% 1,2-pentanediol (P_10), and 2.5 wt% 1,2-hexanediol (H_2.5). N.D.: not detected.

5.3.5 Hair Adsorption Properties of PS-DHHB

Figure 5-10 shows SEM images of hair samples subjected to various treatments: water (panel a), PS-DHHB dispersion (panel b, Entry 2), and anionic PS-DHHB dispersion (panel c, Entry S2). Figure 5-10d shows a magnified image of the area delineated in Fig. 5-10b. The preparation protocol for Entry S2 and its associated characterization results are documented in Tables 5-2 and 5-4, respectively. The images reveal the unique scale-like architecture of hair strands, and particles are visible *over* an expansive area of the hair surface in Figs. 5-10b and 5-10d. The average diameter for 10 particles observed in Fig. 5-10d was 263 ± 19 nm, corroborating the findings of DLS measurements (Entry 2 in Table 5-4). In contrast, no particles were deposited on the hair surface in Figs. 5-10a and 5-10c, affirming that cationic PS-DHHB adhered robustly to hair whereas anionic PS-DHHB did not.

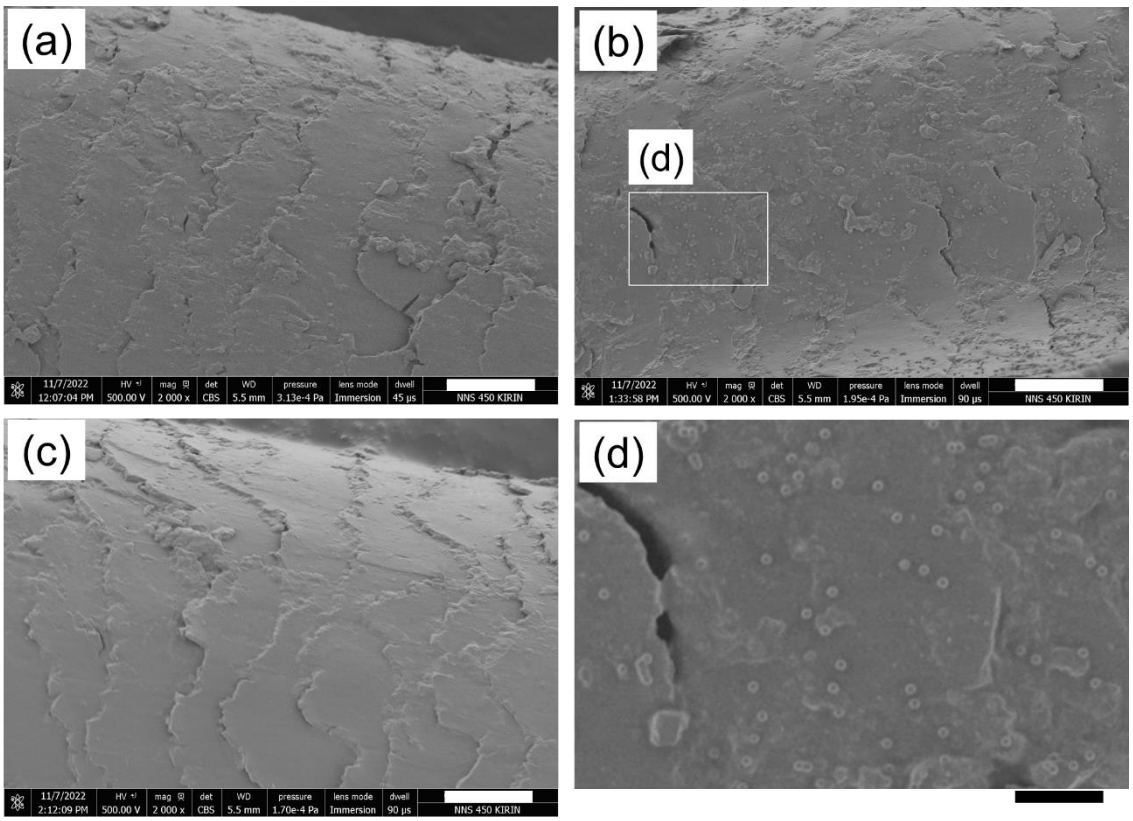

Fig. 5-10. SEM images of hair fibers treated with (a) water (control), (b) PS-DHHB (Entry 2), and (c) anionic PS-DHHB (Entry S1). (d) Enlarged image corresponding to the square in (b). White scale bar in (a)–(c): 10 μm, black scale bar in (d): 3 μm.

5.3.6 Inhibition of Protein Loss from Hair Due to UVA Irradiation

Figure 5-11 shows the extent of protein loss from hair fibers subjected to UVA irradiation at an intensity of 192 J/cm^2, an exposure equivalent to 10 h of midday sunlight during summertime. Non-treated hair samples exhibited around 1.4 times greater protein loss compared to those treated with particles but not subjected to UVA irradiation (Fig. 5-3). The protein loss in non-treated samples was not statistically different from that in Entry S1. However, a statistically significant difference was observed between the non-treated samples and Entry 2 ($p < 0.05$), indicating that cationic PS-DHHB effectively mitigated UVA-induced protein loss in hair. In contrast, cationic PS devoid of DHHB did not manifest such a protective effect.

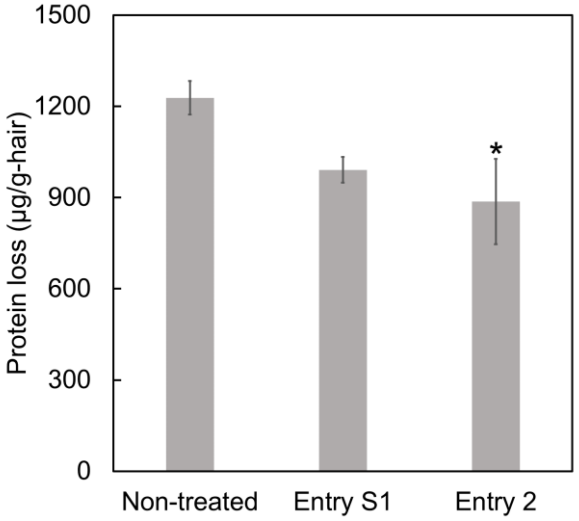

Fig. 5-11. Amount of protein loss due to UVA light exposure (192 J/cm^2) from hair samples treated with PS (Entry S1) and PS-DHHB (Entry 2). *$p < 0.05$ in Dunnett's test, n = 3, mean ± standard deviation.

5.4 Discussion

5.4.1 Difference in Emulsification due to the Molecular Weight of PVA

From the experimental results, PVA with a lower molecular weight (JMR-3H) facilitated the emulsification of styrene prior to polymerization. The size of styrene emulsion droplets stabilized by JMR-3H reached equilibrium within 2 min and remained consistently small, as depicted in Fig. 5-4. Meanwhile, droplets stabilized by JP-05 exhibited a gradual size reduction during 30 min of emulsification (Fig. 5-4). Budhlall *et al*. posited that PVA with D.P. = 480 and D.S. = 88 mol% functions as a clustered assembly of intertwined molecules in aqueous media. Such clustering is attributed to inter-molecular interactions or serial association-dissociation mechanisms [28]. Consequently, the more protracted emulsification kinetics in the presence of JP-05 relative to JMR-3H suggests that JP-05 also displays a clustered morphology.

Moreover, the decline in IT was less pronounced for JP-05 compared to JMR-3H (Fig. 5-2). This could be induced by the less efficient adsorption of JP-05 at the styrene monomer interface due to its clustered state in the aqueous phase. The clustering behavior of JP-05 appears to hinder styrene emulsification in two ways: by decreasing the rate of PVA adsorption at the droplet interface and by stabilizing the interface post-adsorption. Conversely, JMR-3H demonstrated rapid and effective adsorption at the styrene interface, thereby serving as a proficient polymeric emulsifier that stabilized the droplets.

5.4.2 Efficient Preparation of PS-DHHB *via* Miniemulsion Polymerization

Two factors are paramount for the successful synthesis of encapsulated particles by miniemulsion polymerization. First, the formation of small, stable droplets of 30–500 nm is highly desirable [10]. Second, it is imperative to inhibit the genesis of new monomer droplets *via* diffusion from pre-existing droplets. The second factor is essential because substances encapsulated within the monomer droplets, such as DHHB, are prone to precipitation, and the diffusion of monomer (which serves as their solvent) can further reduce their solubility.

To evaluate these factors, I analyzed the number and size of emulsion droplets both before and after polymerization [29]. Additional details on the emulsification procedure are provided in Section 5.4.1. The size distributions by number were unimodal before and after polymerization. Although the size became larger after polymerization, both droplet and particle sizes remained within the desirable range for miniemulsion polymerization, as evidenced in Fig. 5-6.

When employing a water-soluble radical initiator, the formation of oligomeric radicals and micelles occurs in the aqueous phase. These entities help stabilize the droplet interface due to their extensive interfacial area [30]. Presumably, droplet growth could be facilitated either by micellar adsorption or through the fusion of individual droplets. Importantly, no particles smaller than the monomer size of the primary population (approximately 200 nm) were detected,

indicating the absence of new nucleation events (Fig. 5-7). The lack of secondary nucleation sites, attributed to oligomers or micelles, suggests that polymerization took place at the pre-existing monomer droplets.

Incorporating a hydrophobic agent into the monomer phase is an efficacious strategy for preparing encapsulated particles. Specifically, hydrophobic agents help stabilize the monomer phase throughout the miniemulsion polymerization process [31–34]. According to research conducted by Kamogawa *et al*., the solubility of PS significantly augments oil droplet stability [35] and has been employed for the efficient encapsulation of various compounds into particles [36, 37]. In the current study, the incorporation of pre-dissolved PS in the monomer phase (Entries 3 and 4) led to superior encapsulation of DHHB in the resulting particles compared to the particles devoid of PS (Entry 2). These findings support the hypothesis that enhanced stability of styrene monomer droplets and restricted diffusion between such droplets optimize the encapsulation efficacy.

Notably, PS of lower molecular weight increased both the yield and encapsulation efficiency when the weight of PS was fixed. It has been proposed that a hydrophobic polymer dissolved in an oil droplet gains stability through steric repulsion [35]. In the context of this study, I surmise that the surface of the monomer droplet was sufficiently modified by PS molecules to attain stability. This is probably because the rapid molecular diffusion allowed enough molecules to occupy the droplet surface. Consequently, lower-molecular-weight PS effectively inhibited Ostwald ripening and thereby facilitated polymerization. Additionally, possible synergistic stabilization effects due to PVA from the aqueous phase through intermolecular interactions warrants comprehensive investigation in the future.

Entries 2 through 4 demonstrated remarkably high yields (greater than 95%), and these samples were significantly less odorous in comparison to Entry 1, which had a yield of 74% and a more pronounced odor. For the ultimate application of these products in cosmetics, the concentration of residual styrene monomer must be less than 100 ppm as determined by gas chromatography [38]. Should the styrene concentration exceed this threshold, additional optimization of the polymerization process or alternative procedures for monomer removal is necessary. Possible options include copolymerization or centrifugal separation techniques.

5.4.3 UV Absorption and Hair Adsorption of PS-DHHB

A comparison of UV absorption spectra revealed that the λ_{max} of PS-DHHB dispersion was shifted to a longer wavelength compared to that of DHHB dissolved in THF. A previous study of PS particles encapsulating anthraquinones showed that λ_{max} shifted to a longer wavelength because of the π–π stacking of anthraquinones [37]. Similar intermolecular interactions between PS and DHHB may have occurred in the particles studied here.

The outmost layer of hair (cuticle) exhibits a scale-like structure as depicted in Fig. 5-10. This layer is characterized by a strong negative surface charge due to carboxyl groups originating from glutamate, aspartate, and sulfonate moieties [17]. The surface of PS-DHHB carries a positive charge attributable to the imidazolium group of the radical initiator. Consequently, PS-DHHB exhibits enhanced adsorption onto the hair surface *via* electrostatic interactions in comparison to negatively charged particles. For optimized adsorption efficacy, it may be advantageous to adjust the mechanical flexibility of these particles [39]. This can be orchestrated by modulating the glass transition temperature *via* copolymerization, but the encapsulation efficiency must not be compromised.

5.4.4 Applications of PS-DHHB

PS-DHHB significantly inhibited protein loss from hair fibers upon exposure to UVA irradiation, whereas cationic PS demonstrated negligible effects. This inhibitory action of PS-DHHB is hypothesized to occur in two steps. Initially, cationic PS particles adhere to the hair fiber through electrostatic interactions. Subsequently, the encapsulated DHHB blocks UVA irradiation. It is well-documented that exposure to UV radiation generates free radicals in hair, causing the oxidative degradation of proteins, color fading, and reduced aesthetic qualities of hair [18, 40, 41]. Although the literature on cationic UVA filters for hair protection is limited [18], PS-DHHB emerges as a promising candidate for incorporation into hair-care formulations as a novel UVA filter.

Furthermore, our findings indicate that DHHB remains securely encapsulated within the particles even in the presence of alcohols, which are commonly utilized as antibacterial agents in cosmetic formulations. Thus, PS-DHHB should also be stable in aqueous cosmetic compositions. Given that all components of PS-DHHB (PS, DHHB, and PVA) are registered in the International Nomenclature of Cosmetic Ingredients (INCI) and have been used in cosmetics, PS-DHHB holds considerable potential for cosmetic applications. Nonetheless, its safety profile should be verified experimentally.

5.5 Summary

In Chapter 5, PS-DHHB particles were synthesized by miniemulsion polymerization. Utilization of low-molecular-weight PVA as an emulsifying agent was proven to be beneficial for particle formation in this synthesis technique. The incorporation of dissolved PS within the monomer droplet significantly enhanced the encapsulation efficiency of DHHB. The synthesized PS-DHHB particles exhibited four distinct attributes. First, their dispersion was capable of absorbing UVA irradiation. Second, DHHB remained securely encapsulated within the particles, showing no leaching in aqueous alcohol solutions at concentrations typically used in cosmetics for antimicrobial purposes. Thirdly, the cationic nature of PS-DHHB allowed these particles to be adsorb strongly onto human hair *via* electrostatic interactions compared to its anionic counterpart. Lastly, cationic PS-DHHB effectively mitigated protein loss from hair exposed to UVA radiation, outperforming cationic PS particles in this respect. These findings suggest that cationic PS-DHHB particles hold significant potential as UV protective agents in cosmetic formulations.

5.6 References

[1]. Holick, M. F. (1995). Environmental factors that influence the cutaneous production of vitamin D. *Am. J. Clin. Nutr*., 61, 638S-645S.

[2]. Wright, K. P., McHill, A. W., Birks, B. R., Griffin, B. R., Rusterholz, T., & Chinoy, E. D. (2013). Entrainment of the human circadian clock to the natural light-dark cycle. *Curr. Biol.*, 23, 1554-1558.

[3]. Benedetti, F., Colombo. C., Barbini. B., Campori, E., & Smeraldi, E. (2001). Morning sunlight reduces length of hospitalization in bipolar depression, *J. Affect. Disord*., 62, 221-223.

[4]. Ziegler, A., Jonason, A. S., Leffellt, D. J., Simon, J. A., Sharma, H. W., Kimmelman, J., Remington, L., Jacks, T., & Brash, D. E. (1994). Sunburn and P53 in the onset of skin cancer. *Nature*, 372, 773-776.

[5]. Serpone, N., Dondi, D., & Albini, A. (2007). Inorganic and organic UV filters: Their role and efficacy in sunscreens and suncare products. *Inorg. Chim. Acta*, 360, 794-802.

[6]. Landfester, K. (2009). Miniemulsion polymerization and the structure of polymer and hybrid nanoparticles. *Angew. Chem. Int. Ed*., 48, 4488-4507.

[7]. Landfester, K., & Weiss, C. K. (2010). Encapsulation by miniemulsion polymerization. In: Caruso, F. (ed.), Modern Techniques for Nano- and Microreactors/-reactions (Advances in Polymer Science, 229), Springer Berlin Heidelberg, Berlin.

[8]. Tiarks, F., Landfester, K., & Antonietti, M. (2001). Preparation of polymeric nanocapsules by miniemulsion polymerization. *Langmuir*, 17, 908-918.

[9]. Cao, Z. H., Shan, G. R., Sheibat-Othman, N., Putaux, J. L., & Bourgeat-Lami, E. (2010). Synthesis of oily core-hybrid shell nanocapsules through interfacial free radical copolymerization in miniemulsion: droplet formation and nucleation. *J. Polym. Sci. Part A: Polym. Chem*., 48, 593-603.

[10]. Antonietti, M., & Landfester, K. (2002). Polyreactions in miniemulsions. *Prog. Polym. Sci.*, 27, 689-757.

[11]. Wu, P. S., Huang, L. N., Guo, Y. C., & Lin, C. C. (2014). Effects of the novel poly(methyl methacrylate) (PMMA)-encapsulated organic ultraviolet (UV) filters on the UV absorbance and in vitro sun protection factor (SPF). *J. Photochem. Photobiol. B*, 131, 24-30.

[12]. Lorca, B. S. S., Bessa, E. S., Nele, M., Santos, E. P., & Pinto, J. C. (2012). Preparation of PMMA nanoparticles loaded with benzophenone-3 through miniemulsion polymerization. *Macromol. Symp*., 319, 246-250.

[13]. Frizzo, M. S., Feuser, P. E., Berres, P. H., Ricci-Júnior, E., Campos, C. E. M., Costa, C., de Araújo, P. H. H., & Sayer, C. (2019). Simultaneous encapsulation of zinc oxide and octocrylene in poly(methyl methacrylate-co-styrene) nanoparticles obtained by miniemulsion polymerization for use in sunscreen formulations. *Colloids Surf. A*, 561, 39-46.

[14]. Agner, T., Serup. J., Handlos, V., & Batsberg, W. (1989). Different skin irritation abilities of different qualities of sodium lauryl sulphate. *Contact Derm.*, 21, 184-188.

[15]. Agner, T., & Serup, J. (1990). Sodium lauryl sulphate for irritant patch testing -a dose-response study using bioengineering methods for determination of skin irritation, *J. Invest. Dermatol*., 95, 543-547.

[16]. Moore, P. N., Puvvada, S., & Blankschtein, D. (2003). Challenging the surfactant monomer skin penetration model: Penetration of sodium dodecyl sulfate micelles into the epidermis. *J. Cosmet. Sci.*, 54, 29-46. PMID: 12644857.

[17]. Robbins, C. R. (1988). Chemical and Physical Behavior of Human Hair. Springer, New York.

[18]. Dario, M. F., Baby, A. R., & Velasco, M. V. R. (2015). Effects of solar radiation on hair and photoprotection. *J. Photochem. Photobiol. B,* 153, 240-246.

[19]. DeMerlis, C. C., & Schoneker, D. R. (2003). Review of the oral toxicity of polyvinyl alcohol (PVA). *Food Chem. Toxicol*., 41, 319-326.

[20]. Chiellini, E., Corti, A., D'Antone, S., & Solaro, R. (2003). Biodegradation of poly(vinyl alcohol) based materials. *Prog. Polym. Sci*., 28, 963-1014.

[21]. Blehn, G. F., & Ernsberger, M. L. (1948). Polyvinyl alcohol as an emulsifying agent. *Ind. Eng. Chem.*, 40, 1449-1453.

[22]. Lankveld, J. M. G., & Lyklema, J. (1972). Adsorption of polyvinyl alcohol on the paraffin-water interface. III. Emulsification of paraffin in aqueous solutions of polyvinyl alcohol and the properties of paraffin-in-water emulsions stabilized by polyvinyl alcohol. *J. Colloid Interface Sci.,* 41, 475-483.

[23]. Zambaux, M. F., Bonneaux, F., Gref, R., Maincent, P., Dellacherie, E., Alonso, M. J., Labrude, P., & Vigneron, C. (1998). Influence of experimental parameters on the characteristics of poly(lactic acid) nanoparticles prepared by a double emulsion method. *J. Controlled Release*, 50, 31-40.

[24]. Sahoo, S. K., Panyam, J., Prabha, S., & Labhasetwar, V. (2022). Residual polyvinyl alcohol associated with poly(D,L-lactide-*co*-glycolide) nanoparticles affects their physical properties and cellular uptake. *J. Controlled Release,* 82, 105-114.

[25]. Kemala, T., Budianto, E., & Soegiyono, B. (2012). Preparation and characterization of microspheres based on blend of poly(lactic acid) and poly(ε-caprolactone) with poly(vinyl alcohol) as emulsifier. *Arab. J. Chem*., 5, 103-108.

[26]. Taniguchi, Y., & Nomura, S. (2012). Prediction of preservative effectiveness of cosmetics from a predictive formula on the basis of the minimum inhibitory concentration (MIC). *J. Soc. Cosmet. Chem. Jpn.*, 46, 295-300.

[27]. Smith, P. K., Krohn, R. I., Hermanson, G. T., Mallia, A. K., Gartner, F. H., Provenzano, M. D., Fujimoto, E. K., Goeke, N. M., Olson, B. J., & Klenk, D. C. (1985). Measurement of protein using bicinchoninic acid. *Anal. Biochem*., 150, 76-85.

[28]. Budhlall, B. M., Landfester, K., Sudol, E. D., Dimonie, V. L., Klein, A., & El-Aasser, M. S. (2003). Characterization of partially hydrolyzed poly(vinyl alcohol). Effect of poly(vinyl alcohol) molecular architecture on aqueous phase conformation. *Macromolecules,* 36, 9477-9484.

[29]. Landfester, K., Bechthold, N., Förster, S., & Antonietti, M. (1999). Evidence for the preservation of the particle identity in miniemulsion polymerization. *Macromol. Rapid Commun*., 20, 81-84.

[30]. Lovell, P. A., & Schork, F. J. (2020). Fundamentals of emulsion polymerization. *Biomacromolecules*, 21(11), 4396-4441.

[31]. Blythe, P. J., Morrison, B. R., Mathauer, K. A., Sudol, E. D., & El-Aasser, M. S. (2000). Polymerization of miniemulsions containing predissolved polystyrene and using hexadecane as costabilizer. *Langmuir*, 16, 898-904.

[32]. Landfester, K., Bechthold, N., Tiarks, F., & Antonietti, M. (1999). Formulation and stability mechanisms of polymerizable miniemulsions. *Macromolecules*, 32, 5222-5228.

[33]. Bechthold, N., Tiarks, F., Willert, M., Landfester, K., & Antonietti, M. (2000). Miniemulsion polymerization: applications and new materials. *Macromol. Symp.,* 151, 549-555.

[34]. Landfester, K. (2001). Polyreactions in miniemulsions. *Macromol. Rapid Commun.,* 22, 896-936.

[35]. Kamogawa, K., Kuwayama, N., Katagiri, T., Akatsuka, H., Sakai, T., Sakai, H., & Abe, M. (2003). Dispersion and stabilization in water of droplets of hydrophobic organic liquids with the addition of hydrophobic polymers. *Langmuir*, 19, 4063-4069.

[36]. Lelu, S., Novat, C., Graillat, C., Guyot, A., & Bourgeat-Lami, E. (2003). Encapsulation of an organic phthalocyanine blue pigment into polystyrene latex particles using a miniemulsion polymerization process. *Polym. Int.,* 52, 542-547.

[37]. Hu, Z., Xue, M., Zhang, Q., Sheng, Q., & Liu, Y. (2008). Nanocolorants: A novel class of colorants, the preparation and performance characterization. *Dyes Pigm.,* 76, 173-178.

[38]. Johnson, W. Jr., Bergfeld, W. F., Belsito, D. V., Hill, R. A., Klaassen, C. D., Liebler, D. C., Marks, J. G., Shank, R. C., Slaga, T. J., Snyder, P. W., & Heldreth, B. (2014). Safety assessment of styrene and vinyl-type styrene copolymers as used in cosmetics. Final Report. Washington, D.C. Last updated 2014.

[39]. Deshmukh, O. S., van den Ende, D., Stuart, M. C., Mugele, F., & Duits, M. H. (2015). Hard and soft colloids at fluid interfaces: Adsorption, interactions, assembly & rheology. *Adv. Colloid Interface Sci*., 222, 215-227.

[40]. Nogueira, A. C. S., & Joekes, I. (2004). Hair color changes and protein damage caused by ultraviolet radiation. *J. Photochem. Photobiol, B Biol*., 74, 109-117.

[41]. Jeon, S. Y., Long, Q. P., & Lee, W. S. (2008). Comparison of hair shaft damage after UVA and UVB irradiation. *Int. J. Cosmet. Sci.,* 59, 151-156.

Chapter 6 Conclusion

6.1 Summary

This Dissertation describes the following interconnected research. First, the dispersion of cationic PMMA particles was controlled by choosing a suitable counterion for the cationic azo radical initiator with a quaternary ammonium structure. Second, triflate with the -CF_3 group caused aggregation of cationic PMMA latex particles at a lower concentration. To the best of my knowledge, these two findings are novel in improving the dispersion/aggregation of cationic polymer particles prepared with cationic azo radical initiators. Third, cationic PMMA particles with PVA-modified surface were prepared and used as a particle stabilizer for O/W emulsions. Here, the hydrolysis degree of PVA was shown to be crucial for creating robust O/W PEs including HIPPEs. Finally, using low-molecular-weight PVA as an emulsifier, an organic UV absorber was successfully encapsulated into cationic PS particles *via* miniemulsion polymerization. The results demonstrated that low-molecular-weight PVA is a suitable polymeric surfactant in miniemulsion polymerization.

In more detail, Chapter 2 describes the synthesis of PMMA particles using cationic radical initiator *via* SFEP. The dispersion stability of synthesized cationic particles was evaluated. Fast sedimentation within 7 days of storage only occurred when the particles were prepared using ADIP. Further investigation revealed that cationic PMMA particles aggregate significantly in the presence of triflate anion compared to other halides or polyatomic anions. To overcome these disadvantages, I synthesized ADIP-Cl, an ADIP derivative with the triflate counter anion replaced by chloride. ADIP was successfully used as an initiator to prepare cationic PMMA particles that displayed no sedimentation.

Chapter 3 discusses the aggregation mechanism of cationic PMMA latex particles in the presence of triflate. The zeta potential of these particles was significantly lowered in the presence of triflate at a lower concentration compared to other monovalent anions. This is because triflate adsorbs strongly onto the hydrophobic surface and changed the surface charge. Hence, aggregation in the presence of triflate mainly occurs through the vdW attractive force between particles, due to the weaker electrostatic repulsive force. Moreover, the dispersion and aggregation kinetics was investigated in the presence of various electrolytes. The critical coagulation concentration of cationic PMMA latex particles was far lower in the presence of triflate compared to other monovalent anions.

In Chapter 4, cationic PMMA particles prepared using ADIP-Cl were functionalized for PE applications. However, phase separation occurred soon after agitating a mixture of oil, water, and cationic PMMA particles. To prevent emulsion collapse, the PMMA particle surface was modified with PVA. Notably, partially hydrolyzed PVA was found effective for forming an adsorbed layer on the particle surface, resulting in homogeneous PEs without phase separation. The experimental and simulation results indicated that the acetyl group of PVA functioned as an anchor for adsorption onto not only the PMMA particle surface but also the oil-water interface.

In Chapter 5, a UVA absorber (DHHB) was encapsulated in cationic PS particles and dispersed in water using miniemulsion polymerization. Low-molecular-weight PVA was employed as an emulsifier to facilitate both the formation of monomer droplets and the subsequent polymerization process. Importantly, inclusion of PS in the monomer droplet increased the solid content and stabilized the system, thereby enhancing the encapsulation efficiency of DHHB. The synthesized PS-DHHB particles exhibited UV absorption properties very similar to those of DHHB. These water-dispersible PS-DHHB particles carrying positive charge have significant applications in polymer science and cosmetics, owing to their efficient UV absorption and strong adsorption on human hair.

6.2 Future Prospects

Compounds containing fluorine, such as triflate, display hydrophobicity and lipophobicity at the same time (the fluorous effect). Hence, they are usually immiscible with organic solvent and water [1], a feature that is useful in coatings. I predict that linear polymers synthesized using ADIP would also display the fluorous effect. Jitsuhiro *et al*. prepared composite sheets consisting of general purpose PS (GPPS) and linear PS prepared using ADIP (ADIP-PS), and the sheets showed good antimicrobial effects [2]. Those authors thought that during the heat press to prepare the sheets, the fraction of ADIP-PS with high antimicrobial activity (due to the imidazolium structure of ADIP) would localize to the sheet surface. Based on the results described in this dissertation, the localization of ADIP-PS fraction in Ref. [2] may be caused by triflate, the counterion of ADIP. The reason is that triflate gathers and becomes enriched at the air-solid interface through the fluorous effect, and the imidazolium terminus will be pulled up to the surface at the same time.

ADIP derivatives with a counterion containing fluorine are expected to be effective for preparing self-assembled polymer structures such as micelles and nanocapsules [3]. Moreover, the

combination of the imidazolium structure of ADIP and a suitable counterion can lead to new ionic liquid-based polymers for energy devices, environmentally responsive materials, and catalysts [4].

6.3 References

[1]. Dolbier Jr, W. R. (2005). Fluorine chemistry at the millennium. *J. Fluorine Chem.*, 126(2), 157-163.

[2]. Jitsuhiro, A., Maeda, T., Ogawa, A., Yamada, S., Konoeda, Y., Maruyama, H., Endo, F., Kitagawa, M., Tanimoto, K., Hotta, A., & Tsuji, T. (2024). Contact-killing antibacterial polystyrene polymerized using a quaternized cationic initiator. *ACS Omega*, 9(8), 9803-9812.

[3]. Koda, Y., Terashima, T., Sawamoto, M. (2015). Design and functions of fluorous nanospaces with microgel star polymers and amphiphilic random copolymers. *Kobunshi Ronbunshu*, 72(12), 691-706 in Japanese.

[4]. Patra, A., & Matsumi, N. (2025). Densely imidazolium functionalized water soluble poly (ionic liquid) binder for enhanced performance of carbon anode in lithium/sodium-ion batteries. *Adv. Energy Mater.*, 15(5), 2403071.

List of Publications

Below are published original articles by the author of this dissertation.

Chapter 2

Yamazaki, T., Ogawa, A., Koizumi, H., & Tsuji, T. (2021). Controlled soap-free emulsion polymerization stability using a novel cationic azo radical initiator with chloride or triflate counter anion. *Colloids Surf. A*, 609, 125614.

Chapter 3

Yamazaki, T., & Tsuji, T. (2024). Aggregation of positively charged poly(methyl methacrylate) latex particles in the presence of trifluoromethanesulfonate anion. *Chem. Lett.*, 53(7), upae136.

Chapter 4

Yamazaki, T., Suzuki, K., Kobayashi, Y., Arai, N., & Tsuji, T. (2024). Poly(vinyl alcohol)-modified poly(methyl methacrylate) particles for solid-stabilized oil-in-water emulsions. *Colloids Surf. A*, 697, 134433.

Chapter 5

Yamazaki, T., Shimizu, M., Yamada, S., Kanda, R., & Tsuji, T. (2024). Encapsulation of ultraviolet filter into cationic polystyrene particles via miniemulsion polymerization with poly(vinyl alcohol). *Colloid. Polym. Sci*., 302(1), 91-101.

Acknowledgments

I would like to express my deepest appreciation to Prof. Dr. Ken'ichiro Matsumoto and Prof. Dr. Toshifumi Satoh from Hokkaido University for encouragement, constructive suggestions, and guidance.

I would like to acknowledge Assoc. Prof. Dr. Takuya Isono, Prof. Dr. Kazuki Sada, Prof. Dr. Manabu Tokeshi, and Prof. Dr. Takeshi Ohkuma from Hokkaido University as referees for my dissertation and for their helpful suggestions.

I would also like to express my sincere gratitude to Assoc. Prof. Dr. Noriyoshi Arai and Kojiro Suzuki from Keio University, and Assistant Prof. Dr. Yusei Kobayashi from Kyoto Institute of Technology for collaborative research.

I want to thank GOO Chemical Co., Ltd for collaboration and particularly JAPAN VAM & POVAL CO., Ltd. for providing some types of poly(vinyl alcohol) as reagents.

This work was supported by Kirin Holdings Co., Ltd., and was conducted at KIRIN Central Research Institute. First, I thank Dr. Toshikazu Tsuji for providing me with a research environment and offering abundant thoughtful advice ever since I joined his group in 2019. Second, I would like to express my gratitude to Akiko Ogawa, Eriko Sasaki, Rina Kanda, Sayuri Yamada, Yuki Konoeda, Dr. Hideki Koizumi, and Dr. Minori Shimizu for assistance with my Ph.D. work.

I am deeply indebted to the late Prof. Dr. Hiroshi Yamazaki for leading me to science.

Finally, special thanks to my family, relatives, friends, and colleagues for their warmth, continuous support, and encouragement.

March 2025

Takashi Yamazaki